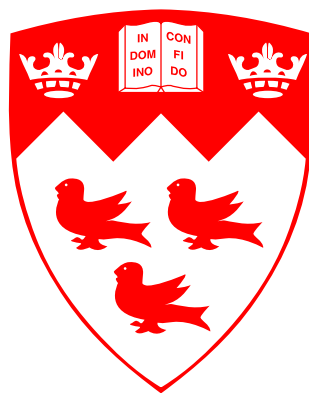


Theory and experimental demonstration of large area suspended graphene varactors

Mohamed Hussein Hamed AbdelGhany



Department of Electrical and Computer Engineering
McGill University
Montréal, Québec, Canada

August 2016

Under the supervision of Professor Thomas Szkopek

A thesis submitted to McGill University in partial fulfillment of the
requirements for the degree of Doctor of Philosophy.

© 2016 Mohamed AbdelGhany

To my family

Abstract

In this thesis we investigated the use of suspended graphene in nano-electromechanical variable capacitors (varactors) and other devices. The superior electrical and mechanical properties of graphene offers promising performance improvement compared to traditional micro-electromechanical systems (MEMS). We have explored the theoretical limit of the suspended graphene varactor, where the capacitance is tuned through the deflection of suspended graphene membrane under electrostatic actuation. Capacitor tuning of 76% is predicted, which exceeds the 50% limit of traditional parallel plate varactor. Actuation voltages as low as 1V can be achieved due to the low flexural rigidity of the suspended graphene. The non-linear response of the varactor was investigated and odd current harmonics are expected for frequencies up to its mechanical resonant frequency, with most of the power concentrated in the third harmonic. At voltages close to the pull-in voltage the third harmonic to fundamental current ratio is ~ 0.3 , which suggests that the device can be used as a mixer or frequency tripler.

We have also investigated the theoretical limit of the suspended graphene tunnelling relay for digital applications. A tunnelling relay is a device that combines the electrostatic actuation and extreme on-off ratio of a mechanical relay with the electrically modulated quantum tunnelling current and steep sub-threshold swings of tunnelling field effect transistors TFETs. We predict sub-threshold swings as low as 10 mV/decade, breaking the thermionic limit of 60 mV/decade at room temperature for metal oxide semiconductor field effect transistors MOSFETs due to the exponential dependency of the tunnelling

current on the electrostatically actuated gap. This device offers a potential reduction in digital circuit power consumption $\sim 1\%$ of the power consumption of state-of-the-art circuits.

We have fabricated large arrays comprising thousands of suspensions to create a tunable capacitance of over $10pF/mm^2$, higher than what is achieved by traditional MEM devices. The devices were fabricated by transferring pre-pattern large area graphene to a silicon oxide on silicon substrate. The graphene is grown using chemical vapour deposition (CVD), and the silicon oxide layer was pre-patterned with trenches for suspensions and metal pads for electrical contact. The bulk of the silicon wafer was used as the fixed electrode of the varactor. Capacitance tuning of 55% was achieved with 10V, which exceeded the 50% limit of traditional parallel plate varactor with a voltage significantly lower than what is needed for a traditional MEMS varactor of the same aspect ratio. Linear and non-linear responses were investigated experimentally and are in good agreement with the theoretical model. The properties of the suspended graphene extracted for capacitance measurements were independently verified using atomic force microscopy (AFM).

Abrégé

Dans cette thèse, nous avons étudié l'utilisation du graphène suspendu dans des condensateurs à nano-électromécanique variable (Varactors) et d'autres dispositifs. Les propriétés électriques et mécaniques supérieures du graphène offre l'amélioration des performances prometteuses par rapport aux systèmes micro-électromécaniques traditionnels (MEMS). Nous avons exploré la limite théorique du varactor de graphène suspendu. La capacité est réglée par l'intermédiaire de la déviation de la membrane de graphène suspendu sous l'actionnement électrostatique. La variation de capacité de 76 % est prévu, ce qui dépasse la limite de 50 % du plateau varactor parallèle traditionnel. Le tension d'actuation plus basses que 1 V peuvent être obtenus en raison de la faible rigidité en flexion de la graphène suspendu. La réponse non linéaire du varactor a été étudiée et les harmoniques de courant sont attendues, la majeure partie de la puissance concentrée dans le troisième harmonique. A des tensions à proximité de la traction en tension la troisième harmonique ratio courant fondamental est $\sim 0,3$, ce qui suggère que le dispositif peut être utilisé comme un mélangeur ou la fréquence tripleur.

Nous avons également étudié la limite théorique de relais tunnel du graphène suspendu pour les applications numériques. Un relais à effet tunnel est un dispositif qui combine l'actionnement électrostatique et un rapport d'un relais mécanique avec le courant d'effet tunnel quantique modulé électriquement et variations abruptes de sous-seuil des transistors à effet tunnel extrême. Nous prédisons un variation sous-seuil de courant aussi faibles que 10 mV / décade de la limite thermoionique de 60 mV / décade à la température ambiante pen-

dant MOSFETs à cause de la dépendance exponentielle du courant tunnel sur la fente actionnée électrostatiquement. Ce dispositif offre une réduction potentielle de $\sim 1\%$ de la consommation d'énergie de l'état de la technique des circuits CMOS.

Nous avons fabriqué des grands tableaux comprenant des milliers de suspensions pour créer une capacité accordable de plus de $10 \text{ pF}/\text{mm}^2$, plus élevé que ce qui est réalisé par des dispositifs MEM traditionnels. Les dispositifs sont fabriqués en transférant de pré-configuration graphène de grande de surface en un oxyde de silicium sur un substrat de silicium. Graphène est cultivé en utilisant le croissance chimique en phase vapeur (CVD) et la couche d'oxyde de silicium a été pré-structurée avec des tranchées pour les suspensions et les électrodes métalliques pour le contact électrique. La plus grande partie de la tranche de silicium a été utilisé comme l'électrode fixe du varactor. Capacité de réglage 55 % a été obtenue avec un tension d'actuation 10V, qui a dépassé la limite de 50 % du varactor classique à plaques parallèles à une tension nettement inférieure à ce qui est nécessaire pour un varactor MEMS classique du même rapport d'aspect. Les réponses linéaires et non-linéaires ont été étudiés expérimentalement et sont en bon accord avec le modèle théorique. Les propriétés du graphène en suspension extraite pour des mesures de capacité ont été vérifiées séparément en utilisant la microscopie à force atomique (AFM) et des techniques de spectroscopie Raman.

Acknowledgements

First and foremost, I would like to express my immense gratitude towards my supervisor Prof. Thomas Szkopek. I am grateful to his guidance, patience, encouragement, and support. I thank him for giving me the freedom to pursue my own ideas and for teaching me to keep the big picture in mind while considering every detail. I am proud he is my supervisor and mentor. I would like also to thank Prof. Dennis Giannacopoulos and Prof. Frédéric Nabki for serving on my PhD committee, their questions and suggestions helped me significantly.

I would like to thank my colleagues and lab mates: Shadi Sabri for getting me started in the fabrication lab and for his advice and support, Elizabeth Ledwosinska for her advice on theoretical analysis of suspended graphene, Helgi Skulason for sharing his experience in fabrication and testing, Peter Gaskell for his help with laboratory equipment and PCB fabrication, Nicholas Hemsworth and Ibrahim Fakih for their help and great discussions, Vahid Tayari for his advice and help with fabrication and testing, and especially Farzaneh Mahvash Mohammadi for her help and patience in growing all the graphene for my several trials.

I would like to thank Prof. Mohamed Siaj for growing the graphene and for his helpful discussions. I would like also to thank Alexandre Favron, Dr. Pierre Lévesque, and Prof. Richard Martel for their help with Raman spectroscopy. I wish to acknowledge the micro-fabrication laboratory staff for their help with my process: Dr. Matthieu Nannini, Dr. Lino Eugene, Don Berry, and Jun Li. I would also like to acknowledge Ms. Mohini Ramkaran for her help with the

atomic force microscopy AFM experiments.

I wish to thank my friends for their support. Also I would like to express my immense gratitude towards my family for their unconditional love and invaluable support.

Finally, I would like to thank our funding agencies without which this work was impossible: Natural Sciences and Engineering Research Council of Canada, Fonds Quebecois du Recherche Nature et Technologies, Canada Research Chairs, and Canadian Foundation for Innovation.

Contents

1	Introduction	1
1.1	Radio Frequency MEMS	2
1.1.1	Micro-electromechanical Systems	2
1.1.2	RF applications	3
1.1.3	Advantages and disadvantages of RF MEMS	4
1.2	MEMS varactors	6
1.2.1	Types of MEMS varactors	6
1.2.2	Electrostatic MEMS varactors	7
1.3	MEMS Switches	10
1.3.1	RF MEMS switches	10
1.3.2	MEMS switches as digital relays	12
1.4	Graphene as a NEMS material	14
1.4.1	Graphene mechanical properties	14
1.4.2	Suspended graphene devices	16
1.4.3	Challenges for graphene NEMS	19
1.5	Thesis contributions	21
1.6	Thesis organization	24

2	Theoretical analysis of suspended graphene varactors and re-	
	lays	26
2.1	Electrostatic actuation of suspended graphene	27
2.1.1	Geometry of the suspended membrane	27
2.1.2	Equation of motion	29
2.2	Design and Analysis of the Suspended Graphene Varactor . . .	35
2.2.1	Device structure and capacitance evaluation	35
2.2.2	Electrical quality factor and design metrics	38
2.2.3	Intrinsic non-linearity	40
2.3	Design and analysis of the tunnelling relay	44
2.3.1	Structure and operation of graphene relays	45
2.3.2	Equation of motion and tunnelling current	48
2.3.3	Sub-threshold slope, dynamic energy, and delay time . .	49
2.3.4	Inverter model	52
2.4	Summary	55
3	Suspended graphene varactor fabrication	56
3.1	Target device and initial trials	57
3.2	Challenges	60
3.2.1	Macroscopic challenges	60
3.2.2	Microscopic challenges	61
3.3	Fabrication process	63
3.3.1	Substrate preparation	63
3.3.2	Graphene growth and pre-patterning	66
3.3.3	Graphene transfer	67

3.3.4	Suspended graphene verification	70
4	Varactor experimental characterization	73
4.1	Linear Electrical Characterization	74
4.1.1	Test setup	74
4.1.2	Capacitance measurement	76
4.1.3	Direct current measurement	80
4.2	Non-linear measurements	80
4.2.1	Device lifetime	83
4.3	AFM characterization of suspended graphene mechanical prop- erties	85
4.4	Summary	93
5	Conclusion and future work	94
5.1	Summary	94
5.2	Future work	96

List of Tables

2.1	Comparison of variable capacitor properties.	41
3.1	Details of the Silicon oxide etch recipe.	65
3.2	Tunable capacitance and yield for the fabricated devices.	70
4.1	Effective values for Young's modulus and pretension per unit width for the working devices.	76

List of Figures

- 1.1 An SEM image of a standard parallel plate varactor fabricated by Zhang and Fang[1]. Reprinted with permission from Elsevier. 4
- 1.2 An SEM image of an ohmic RF switch[2] (©IEEE 2012). The inset is a side view of the switch that shows the gap between the contacts. 5
- 1.3 A simple schematic of a parallel plate capacitor. g_0 is the initial gap between the plates, while d is the deflection of the movable plate due to the applied voltage V_{bias} 8
- 1.4 A simple schematic illustrating the approach of a separate actuation electrode. 8
- 1.5 A) Schematic illustrating a simple example of comb finger varactors. B) SEM images of a fabricated comb finger varactor[3] ©IEEE 2015. 9
- 1.6 A schematic illustrating a simple example of RF capacitive switches. 11
- 1.7 An SEM of a mechanical relay with switching voltage of 5.35 V for logic applications[4] ©IEEE 2009. 14

1.8	An SEM of a mechanical graphene resonator from [5]. Reprinted with permission from AAAS. The scale bar is $1\mu\text{m}$	17
1.9	An AFM image of the impermeable membrane from [6]. Image reprinted with permission from [6] ©2008 ACS.	18
1.10	An SEM image of the suspended graphene switch from [7] ©IEEE 2012. A schematic of the switch is located at the bottom of the figure.	18
1.11	The transfer process used by [8] along with example of good and bad transfers. Image reprinted with permission from [8] ©2009 ACS.	20
2.1	A figure illustrating the forces acting on a suspended membrane. F_s is the strain force, F_{es} is the electrostatic force, T is the pre-tension, and F_{vdW} is the van der Waal-Casimir force.	28
2.2	Two suspended membranes over trenches of width L and height h. A) A suspended membrane with hinged edges $\frac{\partial d}{\partial x}(x=0) \neq 0$ and $\frac{\partial d}{\partial x}(x=L) \neq 0$. B) A suspended membrane with fixed edges $\frac{\partial d}{\partial x}(x=0) = 0$ and $\frac{\partial d}{\partial x}(x=L) = 0$	29
2.3	A) Schematic showing the geometry of the suspended graphene structure under study. B) Top view of the structure showing the relationship between the width and the length of the trenches. C) Cross section of the structure illustrating how voltage is applied between the membrane and the underlying electrode. . . .	30

2.4	Normalized deflection versus bias voltage plot. This is a normalized plot, hence it describes any structure regardless of its dimensions and properties of the materials used.	31
2.5	Comparison of the strain and pretension restoring forces in two cases. The first is a trench of length of $1\mu\text{m}$ and height of 100nm , the second is a trench of length of $2\mu\text{m}$ and height of 100nm . The pretension is assumed to be $S_0 = 0.06\text{N/m}$. This value was determined experimentally by [6].	32
2.6	The pull-in voltage V_{pi} of a suspended membrane versus trench height h with the trench aspect ratio L/h indicated as a parameter.	33
2.7	A) A schematic of the proposed suspended varactor. B) An array of graphene capacitors can be used to increase the total capacitance for a given capacitance per unit width.	36
2.8	The relative change in capacitance $[C(V_{bias}) - C(0)]/C(0)\%$ versus DC bias voltage V_{bias} for a capacitor of length $L = 2.5\ \mu\text{m}$ and a trench height $h = 0.1\ \mu\text{m}$. An approximate linear response is observed over a 40% tuning range, with a total tuning range of 76% at pull-in.	37
2.9	An electric circuit model accounting for graphene resistive losses, with R being the total graphene membrane resistance, C being the total graphene-fixed plate capacitance, and n the number of discrete elements used to approximate the distributed system, with a continuum model reached as $n \rightarrow \infty$	38

-
- 2.10 Electric quality factor Q versus operating frequency for a graphene varactor of length $10\mu\text{m}$ and height $1\mu\text{m}$. The quality factor drops to unity at high frequency and high sheet resistance, where the varactor acts as a lossy transmission line. 39
- 2.11 The trench aspect ratio L/h is determined by the design metric $1/\omega Q V_{\pi}^2$ and the available graphene sheet resistance R_S 40
- 2.12 The relative change of capacitance with voltage from $-V_{pi}$ to V_{pi} for a capacitor of length $L = 2.5 \mu\text{m}$ and a trench height $h = 0.1 \mu\text{m}$. The effect of pretension is ignored. 42
- 2.13 A) AC applied voltage to a SGV, $V_{ac} = 0.5V_{pi} \times \cos(2\pi \times 10\text{kHz})$.
 B) Total current per unit width for the capacitor described in Fig. 2.12. C) The change in current due to capacitance change VdC/dt 43
- 2.14 The magnitude of quadrature Fourier components B_k of the total current per unit width from Fig. 2.13. The even harmonics do not appear on the graph because their magnitudes are much smaller than $10^{-2}\mu\text{A/m}$ 44
- 2.15 The harmonic components B_k of varactor current versus AC amplitude V_{ac} for the suspended graphene varactor described in 2.12, where $V_{pi} = 4.7 \text{ V}$, $L/W = 25$, and $V_{dc} = 0$ 45

-
- 2.16 (a) Schematic of a tunnelling relay (TR), including a suspended graphene membrane, gate electrode for electromechanical actuation of membrane motion, and contact electrode atop a gate insulator layer. Critical TR dimensions including the tunnelling gap g are indicated in the diagram. (b) Circuit symbol for a TR. (c) Force diagram for the suspended graphene membrane, including the electrostatic force F_{es} , van der Waals force F_{vdW} and mechanical strain force F_{mech} 46
- 2.17 Tunnelling current J_D versus applied contact voltage V_D , with V_G as a parameter and $V_S = 0$. The device dimensions are $L = 800$ nm, $h_0 = 16$ nm, and $h_1 + h_2 = 8$ nm. These dimensions are used in all TR simulations in this section. 50
- 2.18 Scaling of actuation voltage V_G versus contact electrode diameter D_C under the constraint $E_{vdW} = 0.5 E_{es}$ 50
- 2.19 Tunnelling current J_D versus gate voltage V_G at fixed contact voltage $V_D = 0.5$ V. A mean sub-threshold swing of $S \sim 10$ mV/decade is predicted. 51

2.20	A) The dynamic energy consumed with a representative load capacitance $C_L = 2.5$ fF versus operating voltage V_D . The proposed graphene TR, the experimentally demonstrated drift TFET[9], and the 22 nm CMOS low stand-by power node from 2011 report of International Technology Roadmap of Semiconductors [10]. B) Electromechanical delay time τ versus contact diameter D_C under the constraint $E_{vdW} = 0.5 E_{es}$. A sub-ns delay is predicted.	53
2.21	A) Schematic and circuit diagram for a TR inverter, with input and output voltages V_{in} and V_{out} respectively. B) The transfer characteristic of an inverter built from two tunnelling relays with the geometry of Fig. 2.17. C) Circuit diagram for a universal NAND logic gate composed of TR switches, with inputs A and B	54
3.1	Schematic of the ideal structure for a suspended graphene varactor.	57
3.2	Schematic of "proof of concept" structure for a suspended graphene varactor.	58
3.3	A diagram of the proposed process flow illustrating the three stages of fabrication.	59
3.4	An SEM image demonstrating the different problems associated with manual transfer.	61
3.5	An SEM image demonstrating the different problems associated with graphene suspensions.	62

-
- 3.6 Part of the two overlapping masks used for contact deposition and trench etching showing four adjacent devices. The mask represents the top view of the varactor. 64
- 3.7 Partial SEM of a fabricated substrate showing the trenches and metal contact. 65
- 3.8 A contact mode AFM line scan across two trenches. 66
- 3.9 Part of the mask used for patterning graphene. Continuous pieces of graphene are used as alignment marks. 67
- 3.10 A diagram showing how the PMMA supported graphene is scooped out of a liquid. 68
- 3.11 False colour SEM images of the fabricated devices. A) Image of few suspensions. B) Magnified image of a single suspension. C) Low magnification image of one third of a varactor showing hundreds of suspensions. 69
- 3.12 A) A contact mode AFM image of the probed area showing the cross sections sampled across the trench and suspended graphene. B) Cross sections of trenches and suspended graphene. 70
- 3.13 A) Raman spectrum of the graphene after all processing and transfer. The pump wave length was 514.5 nm. B) Partial map of the 2D peak intensity of a suspended graphene varactor made using hyperspectral Raman imaging technique with a pump wave length of 532 nm. C) Partial map of the wave number shift of the 2D peak of the same area, where the black areas denote no peak. 72

-
- 4.1 A) The circuit schematic of the used for capacitance measurement. B) A simple diagram illustrating how the device is connected in the probe station. A metal probe is fixed to metal contact in the device, while the ground is connected to the silicon wafer. A false colour SEM image shows how the metal contact is connected to the suspended graphene. 74
- 4.2 A) The circuit schematic of extracted probe station model. The best fit model parameters are $L_{ps} = 0.75\mu\text{H}$, $R_{ps} = 1.55\text{k}\Omega$, $L = 61\text{cm}$, and $Z_0 = 50\Omega$. B) and C) The measured short circuit impedance Z_{in} between the probe station terminals. The short circuit was achieved by landing the probe directly on the chuck. 75
- 4.3 The relative change in capacitance $[C(V_{bias}) - C(0)]/C(0)$ versus DC bias voltage. Both measurement and the theoretical model are depicted here. The capacitance change is calculated relative to the tunable suspended capacitance. The graph shows forward and backward measurement sweeps with no hysteresis. The model includes a pre-tension $S = 0.04 \pm 0.01\text{N/m}$ and a Young's modulus $E = 180 \pm 15\text{GPa}$ 78
- 4.4 Schematic of the three terminal device used for DC measurements. The gate voltage was applied through the probe station chuck. 81

-
- 4.5 A) Current across the graphene I_{ds} versus voltage across the graphene V_{ds} at bias voltage $V_g = 0$. The curve shows ohmic behavior. B) Current across the graphene strips I_{ds} versus gate voltage V_g at $V_{ds} = 0.1\text{V}$ 81
- 4.6 Measured change in capacitance $[C(V_{bias}) - C(0)]$ versus bias voltage V_{bias} from -10 V to 10V. The figure shows capacitance ambivalence to the voltage polarity. The numbered arrows show the order in which the sweeps were done. The capacitance was measured using an excitation AC voltage of amplitude 30 mV and frequency 100 kHz. 82
- 4.7 A) Setup used for non-linear measurements. B) Measured and theoretically modelled third harmonic component of the varactor current due to a 20 kHz AC excitation. The amplitude of the AC signal was swept from 1 V to 10 V. The model includes $S = 0.04\text{N/m}$ and $E = 180\text{GPa}$ 83
- 4.8 A) SEM images before and after applying and AC voltage V_{ac} with amplitude 10 V and frequency 1 kHz for several seconds. It shows graphene suspension collapse. B) The capacitance change versus voltage for this device before and after applying the voltage. 84
- 4.9 A) SEM image of the collapses in a suspended wide strip. B) The suspended capacitance versus voltage for this device as it decayed. 85
- 4.10 Contact mode AFM images of two of the probed areas, where the white marks denote the positions of indentation. 86

- 4.11 Raw data from the force versus displacement experiment. A) The tip deflection ΔZ_{tip} versus the piezo position ΔZ_{piezo} . The graph shows an initial dip in deflection that corresponds to the sudden attraction between the tip and the surface as the tip reaches the surface. As the piezo presses on, the tip starts deflecting upward. B) The extracted graphene deflection $\Delta Z_{graphene} = \Delta Z_{piezo} - \Delta Z_{tip}$ versus ΔZ_{piezo} . C) The force applied by the piezo $F = k_{tip}\Delta Z_{tip} = k_{graphene}\Delta Z_{graphene}$ versus graphene deflection $\Delta Z_{graphene}$. The spring constant of the cantilever $k_{tip} = 0.92\text{N/m}$ 88
- 4.12 A) $F - D$ curves for two indentations on the same suspension. The agreement of the data suggests that suspension was not damaged by the first indentation. B) $F - D$ curves for two indentations on a different suspension. The disagreement between the data suggests that suspension was damaged by the first indentation. 89
- 4.13 A) Applied force versus displacement for a narrow membrane with a linear fit. The inferred S_0 value is 54 mN/m. B) The extracted S_0 values of 12 suspensions versus their W/L 90
- 4.14 A) The geometry of membranes under consideration. B) Applied force versus displacement for a large membrane with a linear fit. The inferred E value is 170 GPa. C) The extracted E values of 14 suspensions versus their W/L 92

-
- 5.1 A) A comparison between this work and different types of state of the art MEMS varactors. The figure shows the air/vacuum gap versus the area per pF. The devices shown are state of the art silicon based MEMS varactors: parallel plate with fractal structure[11], curved plate varactor[12], vertical parallel plate[13], parallel plate with levers[14], original parallel plate design[1], and comb finger varactor[3]. Further indicated in the graph are the ideal limits achievable in accordance with $C/A = \epsilon/h$. The varactor height is limited by spontaneous pull-in from Casimir-van der Waals forces. 95
- 5.2 A) Schematic of the fabricated device, while B) shows the a schematic of the improved varactor design. 98

Chapter 1

Introduction

This chapter presents the introduction and motivation to this work. It starts by a short introduction to Mico-electromechanical systems (MEMS) and there Radio Frequency (RF) applications, demonstrating their advantages and disadvantages. We concentrate on the most common RF MEMS, which are variable capacitors and switches. Examples of the most commonly used architectures are emphasized. Finally we discuss the application of graphene to electromechanical structures, including potential advantages arising from the unique properties of graphene. We conclude the chapter with a summary of the original contributions of this thesis, a discussion of author contributions, and an overview of the structure of the remainder of this thesis.

1.1 Radio Frequency MEMS

1.1.1 Micro-electromechanical Systems

Since the fabrication of the first semiconductor transistor the field of semiconductors has been growing rapidly[15]. The invention of the integrated circuit and its fast pace growth inspired by Moore's Law required rapid advancement in the area of micro-fabrication[16]. In the 1960s the fabrication of 3D features in semiconductor chips was achieved using isotropic and anisotropic etching of silicon and silicon oxide. These etching processes were developed mainly for optoelectronic applications[17]. These advancements coupled with the discovery of electromechanical behaviour in semiconductors[18, 19] inspired the beginning of MEMS. Since the beginning of the 1980s the field of MEMS has itself grown rapidly. MEMS now have several applications such as: oscillators, scanning optical mirrors, micro-fluidic inkjet nozzles, sensors, and RF switches. MEMS have been in commercial use since Hewlett Packard invented the MEMS ink-jet nozzles for its printers in 1978[16]. In 2012 the MEMS market was 10.7 billion USD and has continued to grow without any sign of abating.[20]. The RF applications sector constitutes more than 10% of this market and grows steadily at an annual rate of 17 % [21]. The ultimate goal of MEMS development is achieving full monolithic integration with integrated circuits; but to achieve this goal two main challenges need to be faced: reducing the size of MEM devices and developing fabrication/integration processes compatible with CMOS fabrication processes[22]. In this thesis we studied the viability of graphene MEMS/NEMS for RF applications; especially that the

atomic thinness of graphene and its low elastic stiffness suggest that graphene NEMS will offer a significant reduction in size compared to traditional MEMS. In parallel integration of graphene with CMOS integrated circuits has been achieved by other researchers using a minimum number of post processing back-end of line steps[23, 24].

1.1.2 RF applications

RF MEMS have several applications. They are used in transmitter and receiver circuits and radar circuits. These circuits use MEMS components for two main functionalities the first being tuning the operating frequencies in oscillators, filters, and mixers. This tuning enables the same AM or FM radio circuit to operate over a wide frequency range. This technique is also used in mobile phones, wireless computer networks, and satellite receivers. The centre frequency of an LC oscillator $f_0 = \frac{1}{2\pi\sqrt{LC}}$ is most easily tuned by modulating the value of the capacitance (C) in the circuit. This can be achieved through a variable capacitor (varactor). There are several kinds of varactors. The most common are junction varactor, MOS varactor, and MEM varactor[25]. Fig. 1.1 depicts a parallel plate varactor extracted from reference [1], which is an example of MEMS varactors.

The second main use of MEMS in RF circuits is multiplexing the transmitter and receiver terminals to the antenna port. Most wireless devices have a single antenna or an array of connected antennas that is used for both transmitter and receiver. Each of the transmitter and the receiver is only connected to the antenna when it is in use. This multiplexing can be achieved through

microwave duplexers, semiconductor switches, or MEM switches. An example MEM switch is depicted in Fig. 1.2[2].

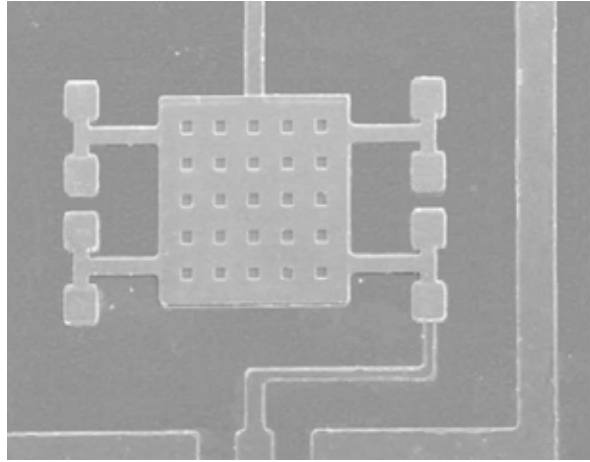


Fig. 1.1: An SEM image of a standard parallel plate varactor fabricated by Zhang and Fang[1]. Reprinted with permission from Elsevier.

1.1.3 Advantages and disadvantages of RF MEMS

Recently, RF MEMS are increasingly replacing their solid state counterparts because of their better performance[13]. RF MEMS out perform solid state devices in several aspects. RF MEMS do not respond to noise signals with frequencies higher than their mechanical resonant frequency[14]. Another advantage of RF MEMS is their higher electrical quality factor, as the presence of a vacuum gap dramatically decreases leakage current[25]. The lower leakage current adds another advantage to the RF MEMS; it results in lower power consumption[26]. Other advantages include higher linearity[11], higher power handling capabilities[27], and good performance up to the THz range[28].

Despite all advantages mentioned above, RF MEMS have two main disadvantages. These two disadvantages are size and actuation voltage[25]. Large

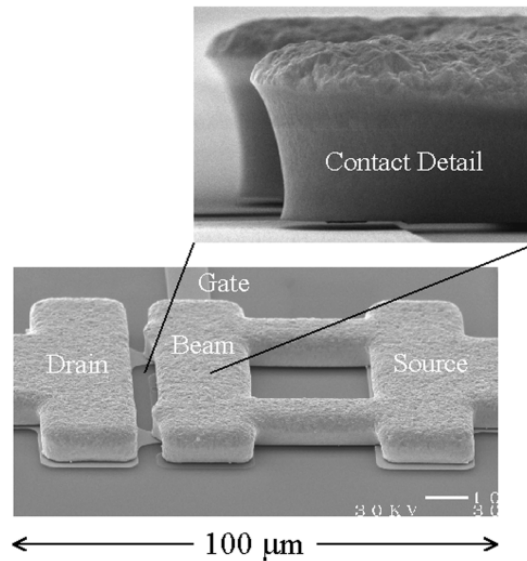


Fig. 1.2: An SEM image of an ohmic RF switch[2] (©IEEE 2012). The inset is a side view of the switch that shows the gap between the contacts.

size is a problem because area on silicon wafers is expensive, and high actuation voltage is a problem because it requires the addition on special circuits such as charge pumps and DC-DC converters to increase the voltage from the low circuit operating voltage to high MEMS operating voltage, these circuits occupy large area and have low power efficiency[29]. An additional disadvantage of large size is the difficulty of integration on CMOS chips[12]. Silicon is the material most widely used in MEMS[16]. Due to the stiffness of silicon, beams and plates made from it must be long in order to deflect with little force. Another solution to the stiffness of MEMS is to reduce the thickness of the beams and plates used. Graphene, the thinnest known conductor[30], offers the limit to thickness reduction[5].

1.2 MEMS varactors

1.2.1 Types of MEMS varactors

There are different categories of MEMS varactors. They are classified according to the physical phenomena causing the capacitance changes. The main categories are electrostatic, piezoelectric, magnetostatic, and electrothermal. Electrostatic varactors are actuated by the Coulomb force resulting from applying a bias voltage. Piezoelectric varactors use a piezoelectric cantilever or membrane, where applying a bias voltage causes it to bend. Magnetostatic varactors are actuated using magnetic attraction, and electrothermal varactors are actuated by the thermal expansion of single or bimorph beam[28].

The most common MEMS varactors are electrostatic. They are preferred because microstructures have large surface to volume ratio and the electrostatic force is a surface force[16]. Other advantages of electrostatic actuation is low power consumption and fast response[31]. Electrostatic actuation depends on the Coulomb attraction between oppositely charged surfaces. Thus capacitance can be modulated by applying a voltage across a pair of electrodes, with at least one flexible electrode.

MEMS varactors have other applications besides RF circuits. These applications are divided into two categories: sensing and actuation. A capacitive sensor is a varactor in which the position of the movable electrode changes due to the surrounding environment, which causes a change in the capacitance that can be detected electrically. Examples of capacitive sensors include pressure sensors, microphones, inertial sensors, and capacitive touch screens[32, 33].

On the other hand, electrostatic actuation is the control of electrode motion through an applied electrostatic force. Examples of electrostatic actuators include micro-motors and digital mirror displays[34, 35, 36].

1.2.2 Electrostatic MEMS varactors

The simplest electrostatic MEMS varactor is the parallel plate architecture[3]. Fig. 1.3 shows a simple schematic of a parallel plate varactor. The capacitance is actuated by applying a voltage across the two plates, which causes the movable plate to move downward. When the deflection d reaches $1/3$ of the initial gap g_0 , the electrostatic force exceeds the restoring strain force and the plate will collapse. This phenomena is called pull-in[37]. Due to pull-in, the maximum capacitance change in a parallel plate varactor is only 50%. This small tuning range is the main limitation of a parallel plate varactor. Other drawbacks are high actuation voltage, non-linearity of the capacitance-voltage (C-V) curve, and large chip area. Several approaches have been proposed to solve the limited tuning range problem[38]. These approaches usually offer a trade-off between tuning range and other parameters such as actuation voltage, linearity, electrical quality factor, and chip area.

The first approach to solve the tuning range problem is to use separate electrodes for actuation as illustrated in Fig. 1.4. The actuation voltage is applied between the movable electrode and one or more electrodes other than the fixed electrode of the capacitor. In this way the movable electrode can be less than $g_0/3$ from the fixed electrode without experiencing pull-in. Rather, pull-in occurs when happens if the deflection reaches $g_1/3$. This approach increases

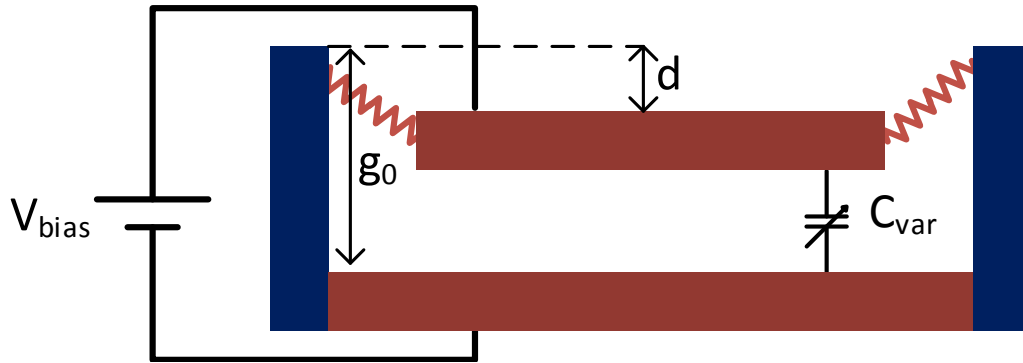


Fig. 1.3: A simple schematic of a parallel plate capacitor. g_0 is the initial gap between the plates, while d is the deflection of the movable plate due to the applied voltage V_{bias} .

the tuning range dramatically, and was extensively demonstrated by Nieminen et al., achieving a tuning range of 271% [39]. Tsang et al. demonstrated an even higher tuning range of 433% [38]. However this increase comes at the expense of actuation voltage, as $g_1 > g_0$. Also, the total chip area increases to accommodate the additional electrodes.

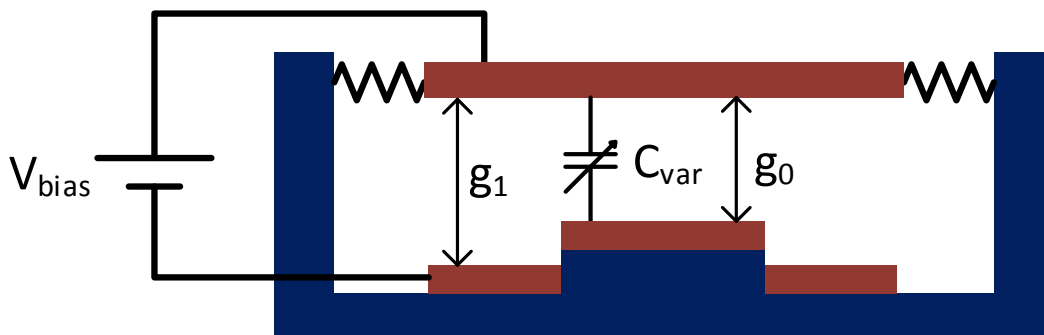


Fig. 1.4: A simple schematic illustrating the approach of a separate actuation electrode.

Another approach is to use a comb varactor. A comb varactor consists of

two interdigitated combs. The total capacitance of this varactor is the sum of the capacitances between the finger of the two combs. The capacitance is varied by changing the common area of the electrodes instead of the distance between them. This can be achieved by two mechanisms. The first method is to electrostatically pull the combs away from each other. Baek et al. used this mechanism to achieve a tuning range over 900% [3]. Fig. 1.5 shows a simplified example of this capacitor as well as the varactor fabricated by Baek et al.[3]. The other mechanism is to rotate the combs away from each other. Nguyen et al. used this mechanism to achieve a tuning range of 3000%[31]. Unfortunately, comb varactors have non-linear C-V curves. They are also intricate structures, which are more difficult to fabricate than parallel plate capacitors. Moreover, they need more chip area to accommodate the actuation mechanisms. These fabrication constraints hinder the integration of comb varactors with CMOS.

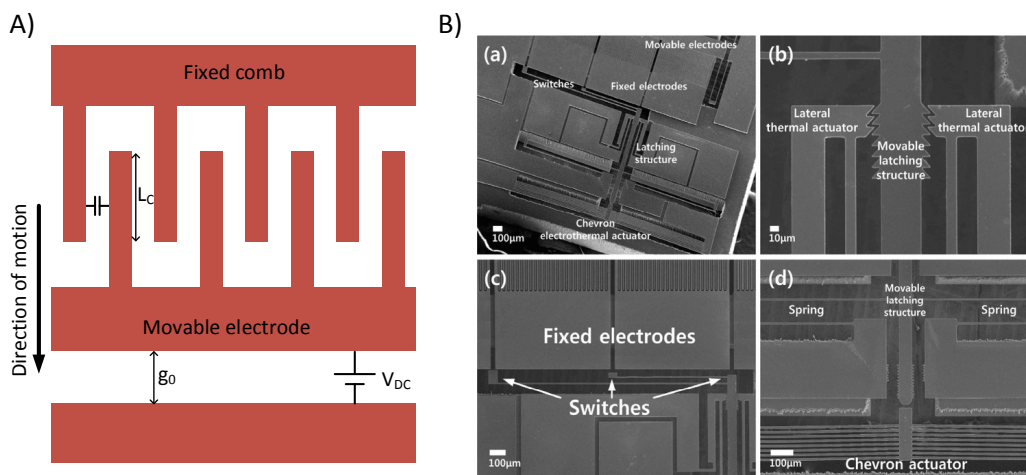


Fig. 1.5: A) Schematic illustrating a simple example of comb finger varactors. B) SEM images of a fabricated comb finger varactor[3] ©IEEE 2015.

There are several other approaches to implementing varactors as well, including: parallel plate with levers[14] and fractal parallel plate[11]. These approaches make the same trade-off as the multiple-electrode structures and combs explained above. Other, more exotic, MEM varactor approaches include parallel plate with movable dielectric -which have small tuning range[40]- and curved plates -which can achieve over 100% tuning in exchange for high actuation voltages[12].

1.3 MEMS Switches

1.3.1 RF MEMS switches

Electrostatic switches are preferred over other types of MEM switches, for the same reasons that electrostatic varactors are preferred. There are two categories of electrostatic switches: contact (Ohmic) switches and capacitive switches[41]. The contact switch is a metal-air-metal (MAM) switch; it turns on through physical contact between two metal electrodes. The contact area needed is small as depicted in Fig. 1.2, which reduces the OFF-state capacitance and improves isolation[42]. Nonetheless, these metal contacts are prone to corrosion. To solve these problems associated with mechanical contact, the capacitive switches were developed[28]. Fig. 1.6 offers a simplified schematic of a capacitive switch. They are metal-insulator-metal (MIM) switches; when in ON-state they have much lower capacitance than their OFF-state capacitance[43]. In the ON-state, RF signals are transmitted through the low capacitive impedance of the switch. Thus, capacitive switches suffer from a lower OFF-state isolation but offers improved device lifetime [27]. In RF cir-

contacts contact switches are connected in series with a transmission line, while capacitive switches are connected in shunt with the transmission line.

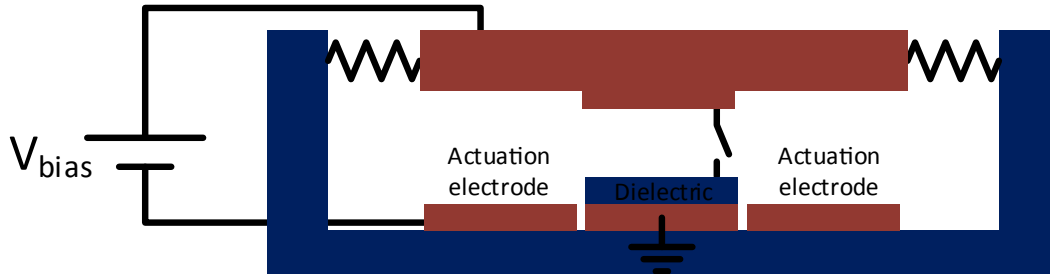


Fig. 1.6: A schematic illustrating a simple example of RF capacitive switches.

Prior to the development of MEM switches, RF switching was performed by semiconductor switches. MEM switches have certain advantages over semiconductor switches. First, MEM switches consume little static power due to the absence of leakage current in their OFF-state, and because their low duty cycles the power consumption of these switches is dominated by the static power consumption. Second, MEM switches have air gaps that result in OFF-capacitance in the fF range[41]. This low OFF-state capacitance ensures high isolation. Moreover, in the on state MEM switches have linear impedance between its electrodes, which prevent the creation of higher order harmonics. MEM switches have their disadvantages. First, they are relatively larger than their semiconductor counterparts; they are in the tens of micrometers range. They are also slower; mechanical response time of structures of this size is in the microsecond range[28]. Furthermore, MEM switches require high actuation voltage, usually tens of volts[44]. The integration with CMOS circuits is also a problem. RF MEM switches have reliability issues. Contact switches

have short lifetime as they are prone to corrosion[2], while capacitive switches suffer from dielectric charging[45].

These disadvantages have been addressed in recent work. Low actuation voltage switches have been developed. Shekhar et al. developed a switch with 4.8V pull-in voltage, while maintaining a good performance with ON-state insertion loss of 0.55dB and OFF-state -47.6 dB isolation[46]. Newman et al. used wafer-capping to produce a hermetic environment, they were able to build contact switches with lifetimes of up to 913 billion cycles[47]. Goldsmith et al. developed a design process that decreases dielectric charging. They were able to build capacitive switches with lifetimes of over 100 billion cycles[48].

1.3.2 MEMS switches as digital relays

The shrinking of the MOSFET transistor has almost reached its limit; traditional scaling of clock speed has ceased for over a decade and power consumption remains a critical limiting factor [49, 50]. An alternative digital logic switch with improved energy efficiency over the MOSFET is now being sought.[51]. This alternative must have lower power consumption, which can be achieved by two means. The first is reduced leakage current to reduce static power consumption. The second is reduced operating voltage (V_{DD}) to reduce dynamic power consumption[52]. There is typically a trade-off between the reduction of static and dynamic power consumption.

The Tunnelling Field Effect Transistor (TFET) and the Electromechanical Relay (EMR) are among the leading proposals widely considered[53, 9] because their energy consumption can potentially be lower than that of MOS-

FETs. Thermionic electron emission over the gate potential barrier limits the sub-threshold swing $S = d(V_G)/d(\log_{10} I_D)$ of a MOSFET to $S_{\text{MOSFET}} = (kT/e) \ln 10 = 60$ mV/decade at room temperature. TFETs can achieve lower sub-threshold swings because its leakage is dominated by quantum mechanical tunnelling through potential barriers rather than thermionic emission. Several low sub-threshold swings were achieved experimentally[54, 55, 56], with a peak of $S_{\text{TFET}} = 42$ mV/decade using Si TFETs [9]. Recently 2D materials have offered some new approaches for TFETs; such as controlling the tunneling barrier height of graphene/boron nitride heterostructures[57], or mechanical modulation of the MoS₂ tunnelling resistance[58]. Although EMRs have the potential to reduce operating voltage, the reduction of electromechanical delay time is a key challenge to low voltage EMR [59].

EMRs were considered as an alternative to MOSFETs as early as 2007. Akarvardar et al. analysed the viability and design of nano-electromechanical switch based digital circuits[60]. Chen et al.[61] further investigated the idea. In 2011 fully functioning EMRs were demonstrated by Kam et al.[4]. Fig. 1.7 shows the logic relay fabricated by Kam et al.. These EMRs had similar structure to RF switches. Their size was in the hundreds of microns range, and they needed V_{DD} of at least 5V[59]. Nonetheless the work was very promising and interest in EMRs increased since then[62, 63, 64]. In 2013, Lee et al. devised a technique for implementing combinational logic circuits using EMRs[65], while Venkatasubramanian et al. devised a technique to implement sequential logic using them[66]. Beiu et al. and Xu et al. investigated hybrid systems of EMRs and MOSFETs that combine the low static power consumption of EMRs and

the low operating voltages of MOSFETs[67, 68].

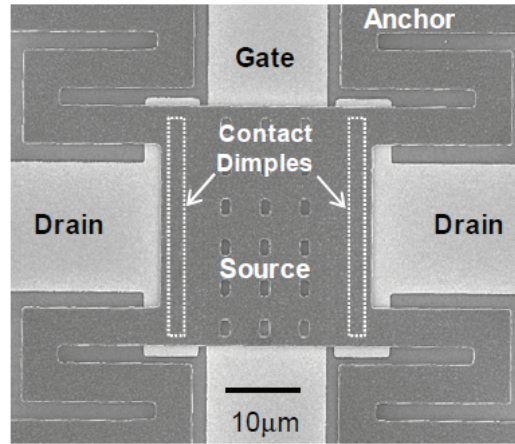


Fig. 1.7: An SEM of a mechanical relay with switching voltage of 5.35 V for logic applications[4] ©IEEE 2009.

1.4 Graphene as a NEMS material

1.4.1 Graphene mechanical properties

Compared to CMOS circuits MEMS are large and have high actuation voltage. Nano-electromechanical systems (NEMS) is the next level of scaling[69]. Thinner beams and plates are used in NEMS to reduce size while maintaining or even reducing actuation voltage. Thin films and nano-materials are used for this purpose[70]. The ultimate limit of thinness is graphene[6], a single layer of carbon atoms[30].

Due to its promise for NEMS, graphene's mechanical properties have been studied since 2007. Frank et al. used atomic force microscopy (AFM) to measure the spring constant of a suspended sheet of few layers exfoliated graphene. They measured the spring constant by force-displacement (F-D) measurements

in the linear F-D domain. From the spring constant, Young's modulus and membrane pretension were extracted. Spring constants between 1 and 5 N/m were measured for sheets less than 10 nm thick, corresponding to a Young's modulus of 500 GPa[71]. Poot and van der Zant used the same technique to measure the bending rigidity and pretension in few layers exfoliated graphene. Pretension in the range of 0.1 N/m and bending rigidity in the range of 10^{-14} nm were recorded; both properties were found to increase with thickness[72]. In 2008, Lee et al. used AFM to measure the F-D response of single layer defect-free exfoliated graphene, extending into the nonlinear regime. A Young's modulus of 1 TPa was reported. A breaking strength of 42 N/m and intrinsic strength for bulk graphite of 130 GPa were also reported[73].

Despite the very large Young's modulus of graphene, atomic layer thickness results in a low stiffness $\simeq 390$ N/m. By comparison, a 15 nm thick membrane of Si_3N_4 has an elastic stiffness of $\simeq 6.3$ kN/m. Equally important, the low mass density of 2D materials, ~ 72 ng/cm² for graphene for example[74], is optimal for minimizing actuation delay time[75].

We would like to note that due to its thinness, graphene will almost always act as a membrane and not as a plate. The difference between plates and membranes in how they respond to loading: plates are thin films that undergo bending stress when loading, while membrane are thin films that undergo in-plane stretching when loading. The bending behavior has a linear load-deflection relation, while stretching has a non-linear load-deflection behavior[76].

1.4.2 Suspended graphene devices

Several suspended graphene NEM devices have been fabricated over the last decade. The simplest and most basic device is the resonator, thus it was the first and most extensively studied. It is also used to further probe the properties of suspended graphene. In 2007, Bunch et al. fabricated the single layer graphene resonator shown in Fig. 1.8. It was both electrically and optically actuated, and optically read. For a resonator $1.1\mu\text{m}$ long and $1.93\mu\text{m}$ wide a resonant frequency (f_0) = 70.5 MHz and quality factor (Q) = 78 were reported. The resonant frequency was much higher than that expected from a tension free resonator. This implied that the resonator behaviour was dominated by built-in tension[5]. In 2009, Chen et al. measured the performance of a electrically actuated single layer graphene resonator using electrical read-out. For a resonator $1.1\mu\text{m}$ long and $3\mu\text{m}$ wide (f_0) = 65 MHz and Q = 125. Effects of mass loading and low temperature were investigated. Mass loading was found to increase the resonant frequency in a low pretension resonator, while low temperature was found to improve the quality factor[77]. In 2010, van der Zande et al. fabricated a large array of suspended graphene resonators. The graphene was grown by chemical vapour deposition (CVD). Thousands of resonators were fabricated with a yield > 80% over trenches with width to depth ratio of ten. Yield decreased with increasing this ratio[78]. Chen et al. built a self-sustaining voltage controlled oscillator (VCO) using suspended graphene resonators. The VCO had tunable range of 14% and was used in an FM radio[79].

Different other graphene NEMS were demonstrated. NEM sensors based

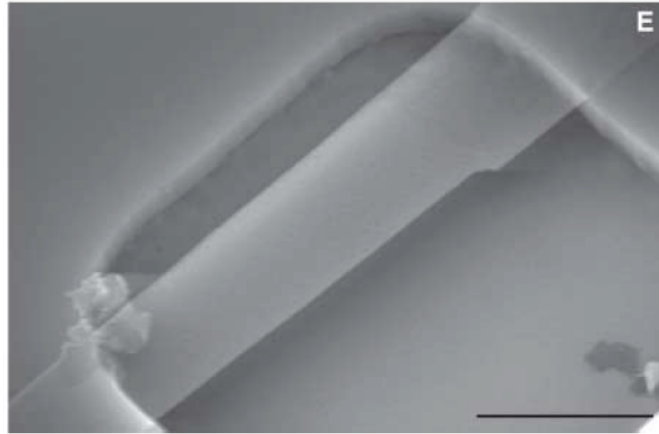


Fig. 1.8: An SEM of a mechanical graphene resonator from [5]. Reprinted with permission from AAAS. The scale bar is $1\mu\text{m}$.

on suspended graphene membranes were widely studied. In 2008, Bunch et al. demonstrated that single layer graphene is impermeable to standard gases. Fig. 1.9 shows an AFM image of the membrane with -93 kPa pressure difference across it. This discovery enables the use of graphene membranes as pressure sensors[6]. Subsequently, suspended graphene pressure sensors with both optical[80] and electrical read out were demonstrated[81, 82]. In 2012, Ledwosinska et al. fabricated an array of micro-Golay cells for infra red sensing based on the same idea[83]. Suspended graphene membranes were also used in chemical and biological sensing[84].

Graphene NEM switches were the next step. In 2009, Milaninia et al. demonstrated a few layer CVD grown suspended graphene switch. The switch had a length to height (suspension) aspect ratio of 40 and an operating voltage of 5V [85]. In 2012, Li et al. demonstrate cantilever NEM switches using few layers graphene. Their operating voltages ranged between 5V and 10V [86]. Recently, the same group demonstrated a 1V NEM switch based on single

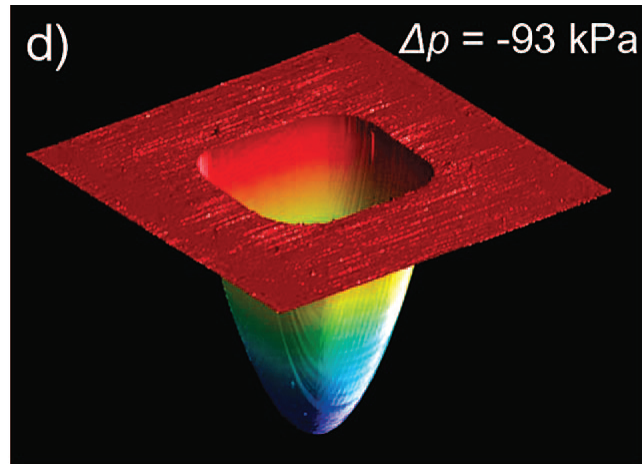


Fig. 1.9: An AFM image of the impermeable membrane from [6]. Image reprinted with permission from [6] ©2008 ACS.

crystalline graphene[7], this switch is shown in Fig. 1.10. Despite this extensive study of graphene NEMS, no suspended graphene varactors had been experimentally demonstrated.

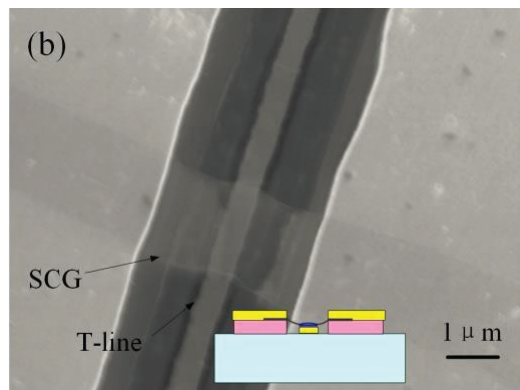


Fig. 1.10: An SEM image of the suspended graphene switch from [7] ©IEEE 2012. A schematic of the switch is located at the bottom of the figure.

1.4.3 Challenges for graphene NEMS

Two main challenges face suspended graphene NEMS: scaling and reliability. Most fabricated graphene NEMS are one-off laboratory scale demonstrations. They cannot be produced on large scale because exfoliated graphene flakes require electron-beam lithography to define contacts to randomly oriented flakes[70]. Few works have demonstrated large arrays of graphene suspensions, where yield depends greatly on the suspension height to length aspect ratio[78, 87]. Yields above 90% could only be achieved for suspensions with aspect ratios below 7[87]. Low aspect ratio devices need high actuation voltage[25], which defeats the purpose of using atomically thin sheets.

These large arrays are made with large area graphene grown by CVD on transition metals such as Cu and Ni[88]. The graphene is then transferred to the target substrate. The transfer process starts by adding a polymer handle for mechanical support. The catalytic metal is then etched away and the graphene transferred into deionized (DI) water. Afterwards the graphene is scooped from the DI water using the target substrate. Finally the polymer handle is removed using solvents and the sample is dried in a critical point dryer (CPD)[78]. Fig. 1.11 shows a flow chart of a similar transfer process as well as optical images well and badly transferred graphene. There are several issues with the process that affects the yield. The manual transfer runs the risk of misaligning, rolling, or crumpling the graphene. The transfer in water leaves water residue that can collapse the graphene if the polymer handle is not sufficiently strong.

Graphene NEMS have relatively short lifetimes. Switches suffer from dif-

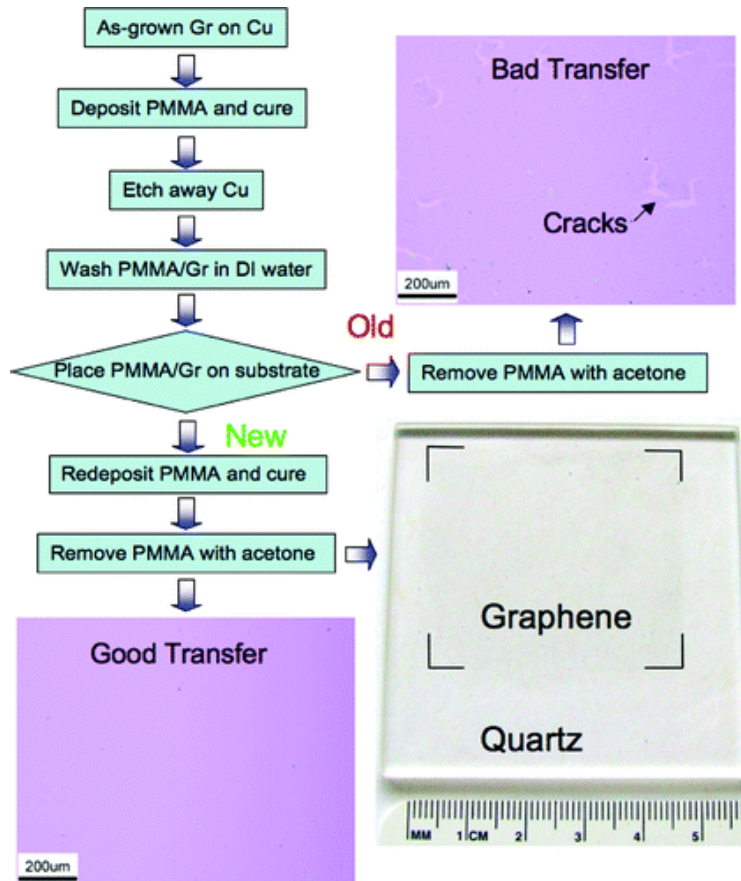


Fig. 1.11: The transfer process used by [8] along with example of good and bad transfers. Image reprinted with permission from [8] ©2009 ACS.

ferent failure modes such as breaking and stiction[85, 70], which limits their lifetime to a few thousands of cycles at most[7].

From these challenges, we can infer why suspended graphene varactors were not previously demonstrated. A varactor large arrays of suspensions with high yield, as a single collapse can short the device.

1.5 Thesis contributions

1. First proposal and theoretical analysis of suspended graphene varactors One of the challenges facing RF MEMS is the scaling of both size and actuation voltage, which are hindered by the thickness of the used material. We have investigated the use of graphene as an ultimately thin suspended membrane for nano-electromechanical varactors. We have developed a model based on large membrane deflection to describe the varactor, which we have used to predict a potential actuation voltage as low as 1V with tuning range of 76% exceeding that of the standard parallel plate varactor. The suspended graphene varactor offers a potential increase in tunable capacitance density because it eliminates the need for additional suspension mechanisms.

2. First proposal and theoretical analysis of graphene tunnelling relays The electromechanical relay is a front runner to succeed the MOSFET in digital applications, nonetheless it faces the same down scaling challenges of RF MEMS. We have explored the theoretical limit of electromechanical relays performance: the tunnelling relay, where the electrostatic actuation combined with the exponential dependency of tunnelling current on gap width offers up to 100 times potential reduction in digital circuit power consumption com-

pared to state-of-the-art CMOS. Tunnelling relays are predicted to have sub-threshold swings as low as 10 mV/decade breaking the MOSFET thermionic limit of 60 mV/decade at room temperature.

3. First demonstration of a suspended graphene varactor We have demonstrated the suspended graphene varactor by fabricating large arrays comprising thousands of suspended graphene strips. We have achieved tunable capacitance density over $10pF/mm^2$, higher than what is achieved by traditional MEMS. Our fabrication process has a yield $\sim 95\%$ over trenches with aspect ratio 16, which exceeds what was previously reported in literature. A capacitance tuning of 55% was achieved, which exceeds the 50% limit of standard parallel plate varactors. Linear and non-linear responses of the varactor were investigated and are in good agreement with the theoretical model developed in this work.

The following publications were generated by the research conducted for this thesis:

1. M. Abdelghany, E. Ledwosinska, and T. Szkopek, *Theory of the suspended graphene varactor*, Applied Physics Letters, Vol. 101, 153102, October 2012.
 - M. AbdelGhany developed the idea with Thomas Szkopek, derived the governing equation, developed the theoretical models, carried on the simulation and analysis, and co-wrote the manuscript.
 - E. Ledwosinska helped derive the governing equations.
 - T. Szkopek developed the idea with M. Abdelghany, supervised all

the work, helped with the theoretical analysis, and co-wrote the manuscript.

2. M. Abdelghany and T. Szkopek, *Extreme sub-threshold swing in tunnelling relays*, Applied Physics Letters, Vol. 104, 013509, October 2014.

- M. AbdelGhany developed the device design, derived the governing equation, developed theoretical models, carried on the simulation and analysis, and co-wrote the manuscript.
- T. Szkopek developed the idea, supervised all the work, helped with the theoretical analysis, and co-wrote the manuscript.

3. M. Abdelghany, F. Mahvash, M. Mukhopadhyay, A. Favron, R. Martel, M. Siaj, and T. Szkopek, *Suspended graphene variable capacitor*, under review.

- M. AbdelGhany developed the idea and designed the experiments with Thomas Szkopek, designed and fabricated the devices, performed the experiments, derived the governing equation, developed the theoretical models, carried on the simulation and data analysis, and co-wrote the manuscript.
- F. Mahvash grew the graphene and performed the spot Raman measurements.
- M. Mukhopadhyay helped derive the equations governing the non-linear behaviour of the varactor.

- A. Favron performed the Raman mapping ($RIMA^{TM}$) measurements.
- R. Martel is the supervisor of A. Favron.
- M. Siaz is the supervisor of F. Mahvash.
- T. Szkopek developed the idea and designed the experiments with M. Abdelghany, supervised all the work, helped with the theoretical analysis, data analysis, and co-wrote the manuscript.

1.6 Thesis organization

This thesis is divided into five chapters. This chapter included the introduction and motivation. It is followed by chapter two, which includes the theoretical part of our work. It starts with the theoretical analysis of the suspended graphene varactor, then it describes the model and predicted performance of the device. Afterwards, it investigates the intrinsic non-linearity in the suspended graphene varactor. Finally it describes the model and predicted performance of the tunnelling relay.

Chapter three presents the fabrication process of the suspended graphene varactor. It starts by illustrating the challenges we faced in fabricating the devices, then it demonstrates the successful fabrication process. It explains how we overcame the challenges. Finally, the fabricated devices are presented. Chapter four demonstrates the experimental results of the suspended graphene varactor. It illustrates the achieved performance and compares it to the predicted performance in chapter 2.

Chapter five summarizes the work done and compares the performance of the suspended graphene varactor with traditional MEMS varactors. It moves on to illustrate the needed improvements to the suspended graphene varactor, and our suggested future work.

Chapter 2

Theoretical analysis of suspended graphene varactors and relays

In this chapter, we studied the electrostatic actuation of suspended graphene. We used the virtual displacement method described in [89] to find an expression of the large deflection of a suspended membrane under electrostatic actuation. Our model differs from available models because it takes into consideration the changing and non-uniform nature of the electrostatic force. We then proposed two novel graphene NEMS: the suspended graphene varactor and the graphene tunneling relay. In the varactor, capacitance is tuned by electrostatic actuation of membrane deflection. We predict a capacitor tuning range of $\sim 76\%$, with a membrane pull-in voltage V_{pi} as low as $\sim 1V$. In the tunneling relay, the electrostatic actuation of a graphene membrane is combined with the ex-

ponential dependence of tunneling current through a vacuum gap. We predict sub-threshold swings as steep as 10 mV/decade, which break the thermionic limit of 60mV/decade at room temperature.

2.1 Electrostatic actuation of suspended graphene

2.1.1 Geometry of the suspended membrane

There are different forces affecting a membrane suspended over a trench. They are divided into two sets: The actuation forces pulling the membrane away from its un-actuated state and the restoring forces pulling it back. We are concerned with electrostatic actuation, in which a voltage applied between the suspended membrane and an underlying electrode causes the deflection. The restoring forces are the strain force and the membrane built-in pretension. The pretension is believed to be due to the adhesion between the membrane and the edges and walls of the trench[6]. When the membrane is closer than approximately 50 nm to the bottom of the trench the van der Waal - Casimir forces will pull the membrane downwards[75]. Fig. 2.1 illustrates these forces and their direction of action.

Single layer suspended graphene membranes generally do not follow Hooke's law because their deflection (d) is always larger than their thickness (t), which puts them in the large deflection domain that is characterized by a non-linear relation between the deflection and the strain force ($F = \alpha d^3$) [83] instead of the linear relation ($F = kd$) that characterizes the small deflection domain. The behaviour of membranes in large deflection depends on the edge boundary conditions. There are two canonical types of edges for suspended membranes:

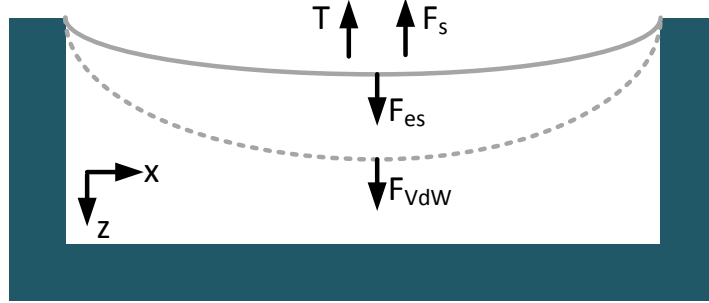


Fig. 2.1: A figure illustrating the forces acting on a suspended membrane. F_s is the strain force, F_{es} is the electrostatic force, T is the pre-tension, and F_{vdW} is the van der Waal-Casimir force.

fixed edges and hinged edges, Fig. 2.2 illustrates the difference between them. At fixed edges the derivative of deflection versus length ($\frac{\partial d}{\partial x}$) is equal to zero, while at the hinged edges this derivative is not equal to zero. The deflection of membranes with fixed edges is approximated with a quartic expression (e.g. $d(x) = (L^2/4 - x^2)(a_{00} + a_{20}x^2)$), while a half cosine approximation is used for those with hinged edges (e.g. $d(x) = d_0 \cos \frac{\pi x}{L}$), where d_0 , a_{00} , and a_{20} are equations parameters[89]. It is not clear whether the edges of suspended graphene are fixed or hinged, however the work of Bunch et al. suggests that they are hinged[6], and as will be seen later in this thesis, our measurements also suggest that hinged boundary conditions apply. Therefore we apply the half-cosine approximation of hinged edges for the work through out this thesis.

In this work we are concerned with infinitely wide suspensions where the deflection is a function only of x . This is suitable for studying wide strips suspended over short trenches, which is the geometry most suitable for a varactor as shown in Fig. 2.3A). Fig. 2.3B) depicts the top view of the membranes

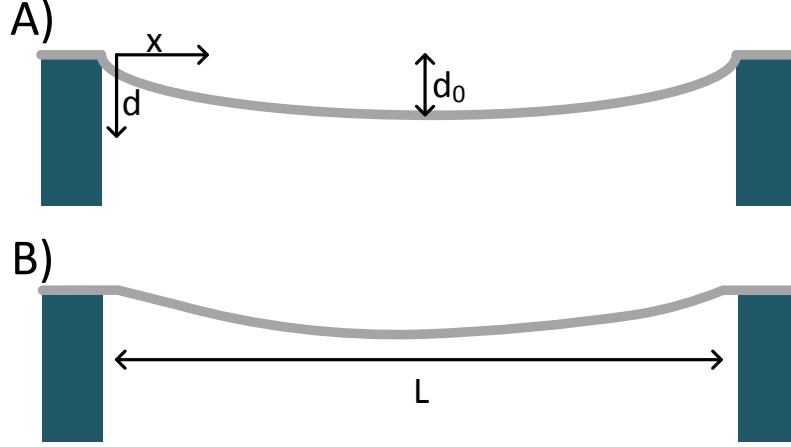


Fig. 2.2: Two suspended membranes over trenches of width L and height h . A) A suspended membrane with hinged edges $\frac{\partial d}{\partial x}(x=0) \neq 0$ and $\frac{\partial d}{\partial x}(x=L) \neq 0$. B) A suspended membrane with fixed edges $\frac{\partial d}{\partial x}(x=0) = 0$ and $\frac{\partial d}{\partial x}(x=L) = 0$.

under study illustrating the trench width and length.

2.1.2 Equation of motion

The application of the actuation voltage between the suspended membrane and the underlying electrode as shown in 2.3C) creates a non-uniform electrostatic force per unit area on the membrane as it deflects. The governing equation of motion was developed by considering first the stretching in the membrane as the only mechanical restoring force, then adding the effect of the membrane pretension, and finally the effect of van der Waals forces. This piece-wise method is similar to the methods in [90] and [89]. By applying the virtual displacement principle and using the half cosine approximation the peak deflection d_0 is implicitly determined from the balance of strain and

30 Theoretical analysis of suspended graphene varactors and relays

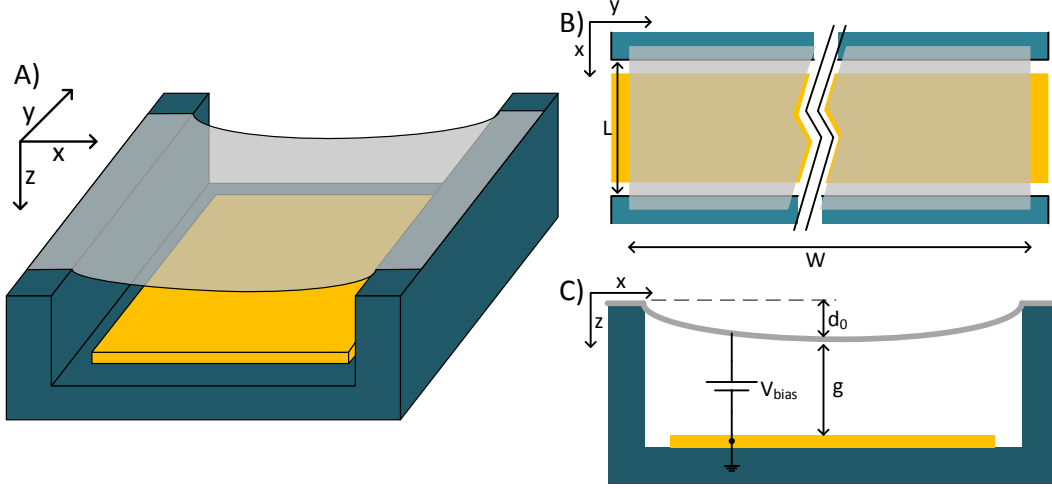


Fig. 2.3: A) Schematic showing the geometry of the suspended graphene structure under study. B) Top view of the structure showing the relationship between the width and the length of the trenches. C) Cross section of the structure illustrating how voltage is applied between the membrane and the underlying electrode.

electrostatic force

$$\frac{Et\pi^5 d_0^3}{8L^4(1-\nu^2)} = \frac{\epsilon V_{bias}^2}{h^2 - d^2} \left(\frac{2d \arctan\left(\sqrt{\frac{h+d_0}{h-d_0}}\right)}{\sqrt{h^2 - d_0^2}} + 1 \right), \quad (2.1)$$

where E is Young's modulus, and ν is Poisson's ratio. The relationship described by Eq. 2.1 is non-trivial, thus we approximated the non-uniform electrostatic pressure on the membrane with a uniform pressure equal to the mean pressure over the membrane

$$\frac{Et\pi^5 d_0^3}{8L^4(1-\nu^2)} = \frac{\epsilon V_{bias}^2}{\left(h - \sqrt{\frac{2}{\pi}} d_0\right)^2}. \quad (2.2)$$

Fig. 2.4 shows the normalized deflection (with respect to trench height)

versus normalized actuation voltage (with respect maximum operating voltage, which will be described in details later) for the mean pressure approximation (Eq. 2.2) and the non-uniform pressure given by Eq. 2.1. The uniform approximation deviates by at most 10% from the non-uniform formula up to 95% of the pull-in voltage.

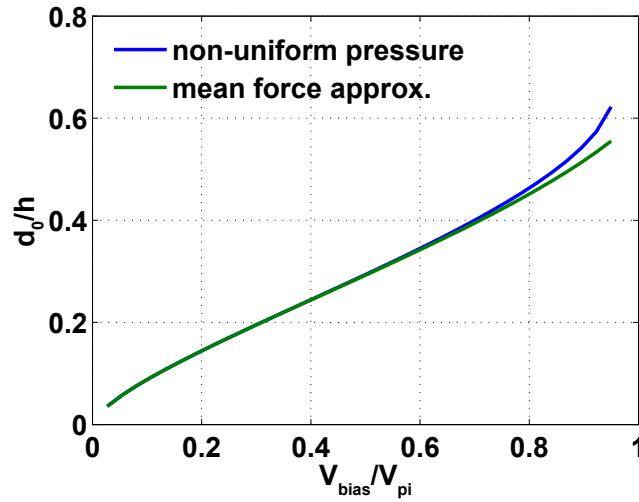


Fig. 2.4: Normalized deflection versus bias voltage plot. This is a normalized plot, hence it describes any structure regardless of its dimensions and properties of the materials used.

The restoring force per unit area due to pretension (T) can be given by Eq. 2.3, where S_0 is the pretension per unit length and C_1 is a constant that is equal to 2 for infinitely wide suspensions and grows rapidly to 3.393 for square suspensions[90]. Fig. 2.5 demonstrates how the ratio between the strain force and the pretension grows with deflection. As long as, the pretension is dominant the total force is linear. It also shows that for the same pretension value the higher the aspect ratio (L/h) the longer T stays the dominant restoring

32 Theoretical analysis of suspended graphene varactors and relays

force.

$$T = 4C_1 S_0 \frac{d_0}{L^2}. \quad (2.3)$$

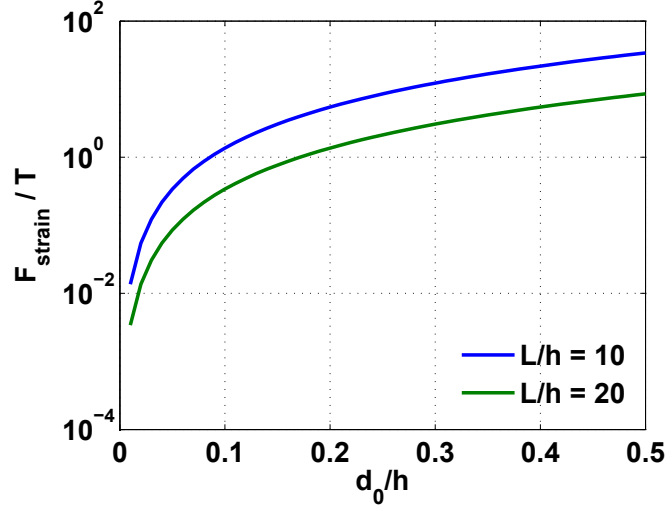


Fig. 2.5: Comparison of the strain and pretension restoring forces in two cases. The first is a trench of length of $1\mu\text{m}$ and height of 100nm , the second is a trench of length of $2\mu\text{m}$ and height of 100nm . The pretension is assumed to be $S_0 = 0.06\text{N/m}$. This value was determined experimentally by [6].

The van der Waals-Casimir pressure between doped graphene sheets ($n \sim 10^{12}\text{cm}^{-2}$) has been theoretically estimated to be $P_{vdW} \sim \frac{\beta}{(h_0-d)}$ over 1-100nm gap distances, where $h_0 - d$ is the gap between the two membranes and $\beta = 65\text{meV} - \text{nm}$ [91]. For gaps larger than 100 nm we can neglect the Casimir effect as the pull-in will happen due to the electrostatic force before these forces are significant.

At equilibrium the system can be fully described by Eq. 2.4.

$$\frac{Et\pi^5 d_0^3}{8L^4(1-\nu^2)} + 8C_1 S_0 \frac{d_0}{L^2} - \frac{\beta}{(h-d_0)^4} = \frac{\epsilon V_{bias}^2}{\left(h - \sqrt{\frac{2}{\pi}} d_0\right)^2}. \quad (2.4)$$

Pull-in occurs in the domain where the deflection is very large and the strain force is the dominant restoring force, hence it occurs when the increase in the electrostatic force is larger than the increase in the strain restoring force $\frac{\partial F_{es}}{\partial d_0} > \frac{\partial F_{strain}}{\partial d_0}$ with an increase in deflection. Determining the deflection at which the pull in occurs from Eq. 2.1 is difficult, however numerical simulations shows that the this equation gives unreliable solution for deflections in the range of $d_0 \sim 0.6h$. Approximation was used to give an approximate pull-in deflection. This approximation was $P_{es} = \frac{\epsilon V_{bias}^2}{(h-d)^2}$, from which we can predict that the pull-in occurs at $d_0 = 3h/5$ instead of $d_0 = h/3$ in Hookean structures. The pull-in voltage is then given by the Eq. 2.5.

$$V_{pi} = \sqrt{\frac{2.25Et\epsilon^3}{1-\nu^2} \frac{\sqrt{h}}{(\frac{\epsilon L}{h})^2}} \quad (2.5)$$

Fig. 2.6 depicts the pull-in voltages for different suspensions.

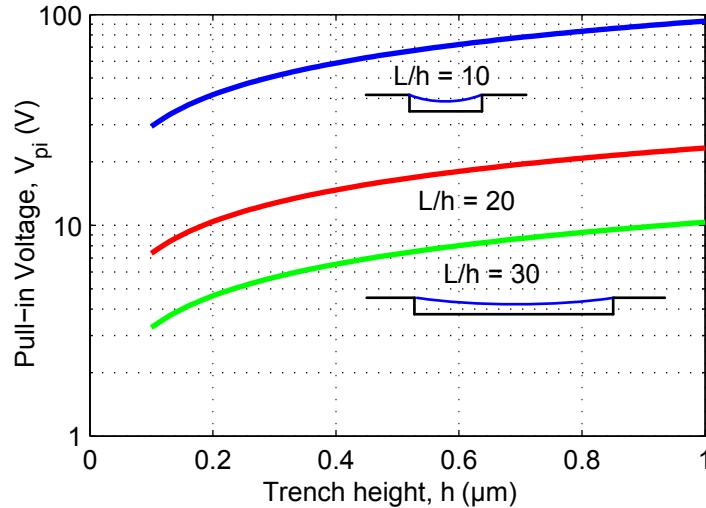


Fig. 2.6: The pull-in voltage V_{pi} of a suspended membrane versus trench height h with the trench aspect ratio L/h indicated as a parameter.

34 Theoretical analysis of suspended graphene varactors and relays

The analytical model, summarized in equations 2.2, 2.3, and 2.4, was built by adding terms developed for specific domains of suspended membrane behavior, e.g. pretension dominated behavior or stretching dominated behavior. Similar models are usually used for graphene[92, 5, 6] as well as other thin film structures[93]. These models can have limited accuracy, especially in the domain where no specific behavior is dominant[76]. Nonetheless we think that this model is sufficiently accurate to represent the structures under study in the domains of interest. Furthermore, this simplified physical model despite its limited accuracy, captures the essential physical trends of the represented structures, and facilitates understanding them.

Although numerical models describing similar problems exist[94], these models were developed for specific geometries, and boundary conditions and are not suitable for simulation of structures with extreme gap to membrane thickness ratio h/t , which is the case in suspended graphene. The finite element method (FEM) is another way to numerically simulate MEMS / NEMS problems, nonetheless, due to the extreme ratio of graphene's sectional dimension to its thickness L/t , the three dimensional gridding in a finite element model is very difficult[95]. One proposed solution is to simulate at greater thicknesses and define a trend to extrapolate the solution for actual graphene thickness[96]. However, it is not clear that this method will offer any improvement in accuracy compared to our model as the extrapolation is not based on a physical principle. Jiang et al. [95] developed another method for finite element analysis of suspended graphene structures using 2D plate models. We implemented a 2D FEM plate model, but encountered failures in numerical convergence for

the conditions relevant to our varactor structures: non-uniform load, complex boundary conditions and low elastic stiffness (and thus high deflection). Moreover, Jiang et al. found that the analytical models developed using the virtual displacement method are in excellent agreement with the FEM simulations. Therefore, we put greater effort into developing simple, approximate, analytical models rather than solving the challenging problem of robust numerical simulation of extreme aspect ratio MEMS. It is beyond the scope of this thesis to develop a model, analytical or numerical, that is suitable for the extreme aspect ratio of graphene, the non-uniform electrostatic load, and the uncertain edge conditions.

2.2 Design and Analysis of the Suspended Graphene Varactor

2.2.1 Device structure and capacitance evaluation

The study of electrostatic actuation of suspended graphene suggests that a suspended graphene varactor (SGV) is very promising. Low actuation voltage coupled with the ability to deflect more than $h/3$ are the main advantages. Fig. 2.7A) offers the proposed varactor structure. The capacitance between the suspended membrane and the fixed electrode changes as the gap is modulated. In this varactor model we made some approximations: we consider the case of highly doped graphene sheets and at least tens of nano-meters of air gaps, therefore the geometric capacitance is much smaller than quantum capacitance, thus dominant over. The quantum capacitance dominates for charge neutral

36 Theoretical analysis of suspended graphene varactors and relays

graphene sheets with ultra-thin dielectrics[97]. We also consider the case of low membrane pretension, because the experimental measurements in [5] and [6] suggest that the restoring force due to membrane stretching will be much greater than the restoring force due to pretension for the geometries we study.

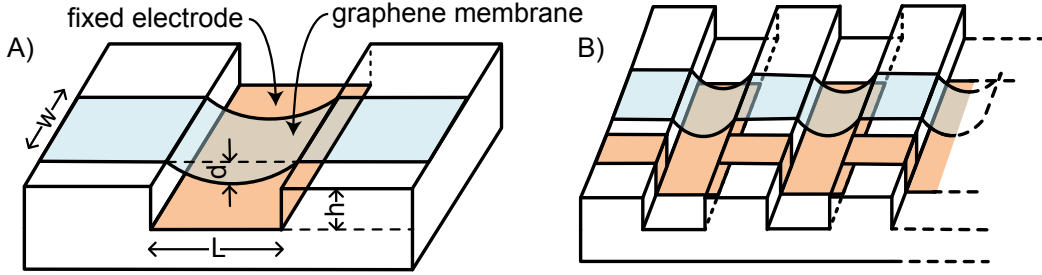


Fig. 2.7: A) A schematic of the proposed suspended varactor. B) An array of graphene capacitors can be used to increase the total capacitance for a given capacitance per unit width.

We are studying the case of $W \gg L$, thus the capacitance per unit width $C' = C/W$ is constant and can be given by the equation:

$$C' = \frac{4C'(0)}{\pi\sqrt{1-d_0^2/h^2}} \arctan\left(\sqrt{\frac{h+d_0}{h-d_0}}\right), \quad (2.6)$$

where $C'(0)$ is the capacitance per unit width at zero bias voltage, and $C'(0) = \epsilon L/h$. Here we are neglecting the fringe capacitance because $W \gg h$ and $L \gg h$. The total capacitance can be increased by using an array structure as depicted in Fig. 2.7B).

The capacitance per unit width as a function of voltage can be calculated from Eq. 2.2 and Eq. 2.6. The maximum capacitance is given by substituting in Eq. 2.6 the deflection at pull-in $d_0 = 3h/5$ giving a maximum capacitance $C'(V_{pi}) \simeq 1.76C'(0)$. Thus a maximum tuning of 76% can be achieved, which

exceeds the maximum tuning of the standard parallel-plate capacitor. Fig. 2.8 demonstrates the expected change in capacitance with voltage for a SVG. The graph shows that the change in capacitance is expected to have an approximate linear behaviour for up to 40% tuning.

Substituting $C'(0) = \epsilon L/h$ in Eq. 2.5 we arrive at Eq. 2.7 that describes the pull-in voltage in terms of capacitance per unit width $C'(0)$.

$$V_{pi} = \sqrt{\frac{2.25Et\epsilon^3}{1-\nu^2} \frac{\sqrt{h}}{(C'(0))^2}} \quad (2.7)$$

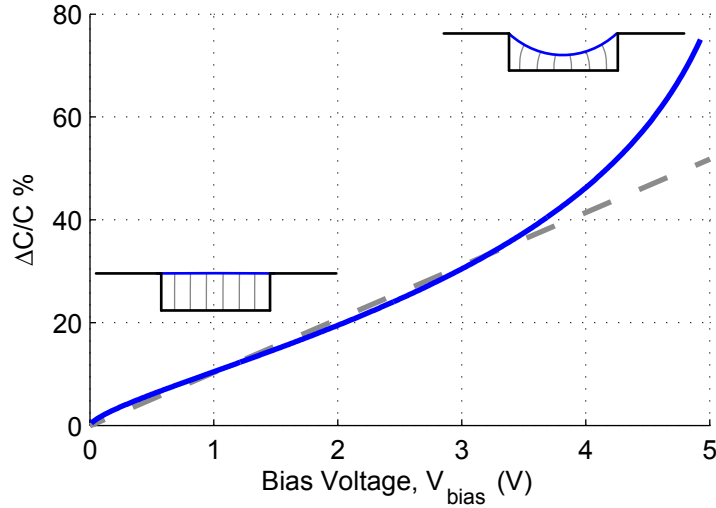


Fig. 2.8: The relative change in capacitance $[C(V_{bias}) - C(0)]/C(0)\%$ versus DC bias voltage V_{bias} for a capacitor of length $L = 2.5 \mu\text{m}$ and a trench height $h = 0.1 \mu\text{m}$. An approximate linear response is observed over a 40% tuning range, with a total tuning range of 76% at pull-in.

2.2.2 Electrical quality factor and design metrics

An important performance metric of any RF device is its electrical quality factor $Q = Im(Z)/Re(Z)$. In SGV it will be limited by the conductive losses in the graphene because the air/vacuum gap diminishes the leakage current. The distributed circuit model depicted in Fig. 2.9 was developed to help approximate the quality factor:

$$Q = \frac{2}{\omega R_s LC'(0)} \tag{2.8}$$

where R_s is the sheet resistance of the graphene. The sheet resistance of graphene can range from several hundreds Ω/\square to several $k\Omega/\square$ [30]. The sheet resistance can be further improved to $150 \Omega/\square$ by strong chemical doping with reagents such as nitric acid[98]. Fig. 2.10 demonstrates the expected quality factors versus frequency for different sheet resistance.

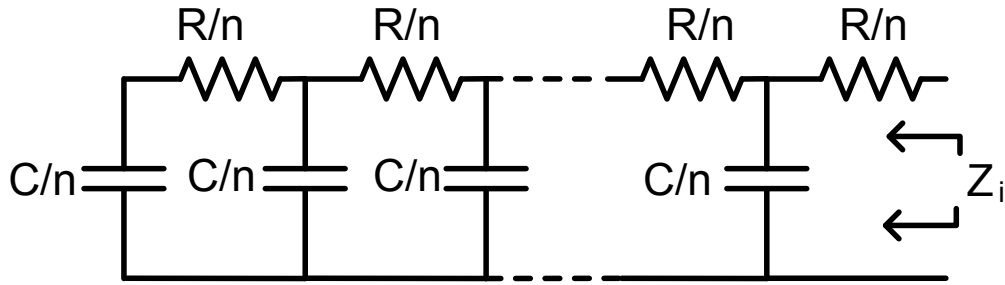


Fig. 2.9: An electric circuit model accounting for graphene resistive losses, with R being the total graphene membrane resistance, C being the total graphene-fixed plate capacitance, and n the number of discrete elements used to approximate the distributed system, with a continuum model reached as $n \rightarrow \infty$.

In order to design a SGV we need to determine its geometry: L , h , and

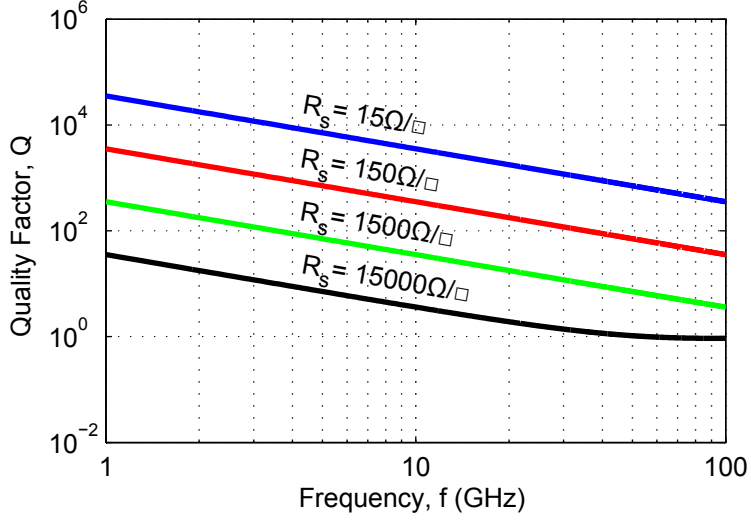


Fig. 2.10: Electric quality factor Q versus operating frequency for a graphene varactor of length $10\mu\text{m}$ and height $1\mu\text{m}$. The quality factor drops to unity at high frequency and high sheet resistance, where the varactor acts as a lossy transmission line.

W from the required specifications: initial capacitance $C(0)$, quality factor Q , operating frequency ω , and pull-in voltage V_{pi} . We developed a design procedure for this purpose: we first use Eq. 2.9 to determine $C'(0)$ from the specifications and the available sheet resistance. This equation was derived by multiplying Eq. 2.7 and Eq. 2.8.

$$\frac{1}{\omega Q V_{pi}^2} = \frac{(1 - \nu^2)}{4.5 E t \epsilon^4} \times R_s \times C'(0)^6 \quad (2.9)$$

The trench height h is determined from Eq. 2.7 using $C'(0)$. Trench length (L) is then determined as $L = C'(0)h/\epsilon$. Finally, the width W can be determined as $W = C(0)/C'(0)$. We introduced a new design metric $1/\omega Q V_{pi}^2$; combining the desired operating frequency, electrical quality factor, and pull in voltage. Fig. 2.11 shows the relationship between the new design metric

and capacitance per unit width $C'(0)$.

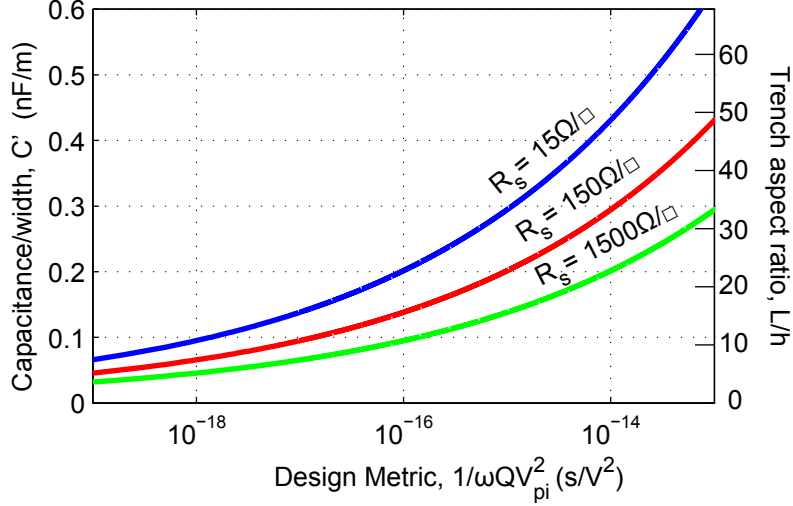


Fig. 2.11: The trench aspect ratio L/h is determined by the design metric $1/\omega Q V_{\pi}^2$ and the available graphene sheet resistance R_s .

As a specific example, If a varactor of the following specifications: $C(0) = 1\text{pF}$, $\omega = 2\pi \times 1\text{GHz}$, $Q = 200$, and $V_{pi} = 5\text{V}$ is to be designed using single layer graphene with $R_s = 1000\Omega/\square$ and $E = 1\text{TPa}$, we need $C(0) = 259\text{pF/m}$. The trench height will then be $h = 292\text{nm}$, and the trench length will be $L = 8.56\mu\text{m}$. The device width will be 3.42mm . Table 2.1 offers a comparison of the expected graphene varactor performance versus some state-of-the-art solid state and MEM varactors. The pull-in voltage, tuning ratio, and quality factor are competitive with existing variable capacitor architectures.

2.2.3 Intrinsic non-linearity

Two of the advantages RF MEMS have over their solid state counterparts are ambivalence to voltage polarity and linearity - absence of higher order

Table 2.1: Comparison of variable capacitor properties.

Varactor Type	Pull-in Voltage	Tuning Range	Q @ 1 GHz
Suspended MEMS[1]	12V	50%	100
Vertically Aligned Nano Fibre[99]	10-30V	50%	25
Junction Varactor[100]	5V	18%	118
Comb Finger varactor[3]	12V	900%	14
Suspended Graphene	1-30V	76%	200

harmonics. These two properties seems contradictory because ambivalence to voltage polarity means the movable electrode deflects at twice the frequency of an applied AC voltage. Nonetheless, MEMS do not respond to signals beyond their resonant frequency, therefore RF frequencies that are much higher than the low mechanical resonant frequency does not affect them. In the same time these MEMS are ambivalent to the polarity of low frequency bias voltages, which make it immune to forward bias leakage. Moreover, this non-linearity can be used to experimentally probe varactor characteristics through the use of high AC voltage.

Ambivalence to voltage polarity

Fig. 2.12 shows the relative change in capacitance with voltage for a SGV from the $-V_{pi}$ to $+V_{pi}$. It shows how the capacitance increases with voltage amplitude regardless of the voltage polarity. The total current is given by:

$$I = \frac{\partial(CV)}{\partial t} = C \frac{\partial V}{\partial t} + V \frac{\partial C}{\partial t} \tag{2.10}$$

Eq. 2.10 shows that the current has at least a third harmonic component as both the voltage and capacitance change in time with frequencies f_0 and $2f_0$

42 Theoretical analysis of suspended graphene varactors and relays

respectively. Finding a closed form expression for the non-linear current proved to be very difficult due to the intricate governing equations. Thus numerical analysis was used to determine the current components and their dependency on AC applied voltage.

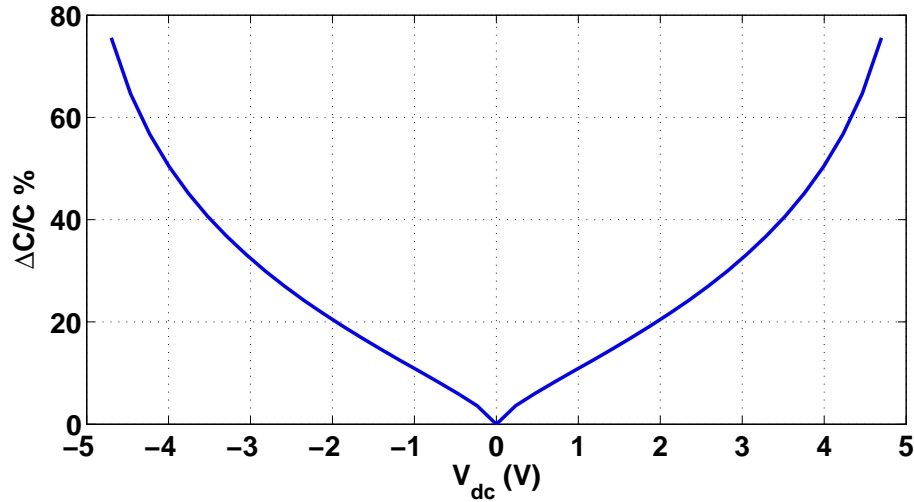


Fig. 2.12: The relative change of capacitance with voltage from $-V_{pi}$ to V_{pi} for a capacitor of length $L = 2.5 \mu\text{m}$ and a trench height $h = 0.1 \mu\text{m}$. The effect of pretension is ignored.

Fig. 2.13B) illustrates the total current of the varactor, while Fig. 2.13C) illustrates the current originating from the time dependent capacitance. The added current shows odd symmetry, which produces odd harmonics in addition to the fundamental component, as expected. The harmonic components of the current were calculated using Fourier series $B_k = 2/T \int I(\tau) \sin(2\pi k\tau/T)$, where k is the harmonic number and $T = 1/f_0$. Only quadrature components are produced as expected from Fig. 2.13. Fig. 2.14 depicts the magnitude of the calculated harmonics.

Fig. 2.15 demonstrates the change in the magnitude of the harmonics with

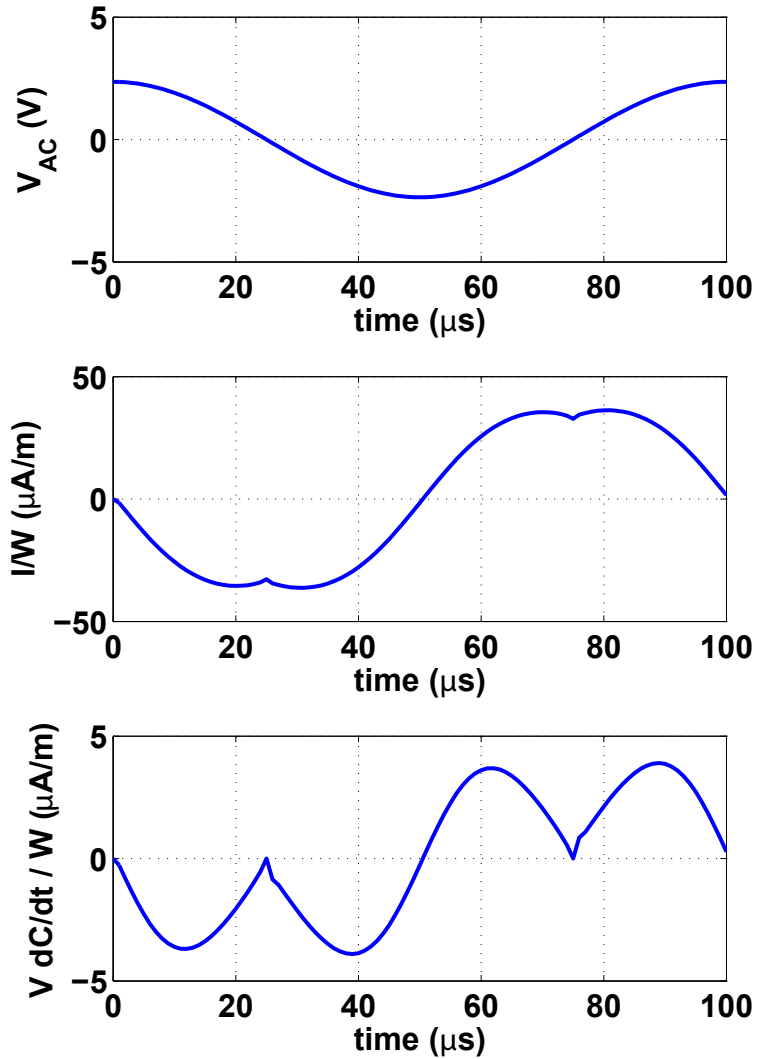


Fig. 2.13: A) AC applied voltage to a SGV, $V_{ac} = 0.5V_{pi} \times \cos(2\pi \times 10\text{kHz})$. B) Total current per unit width for the capacitor described in Fig. 2.12. C) The change in current due to capacitance change VdC/dt .

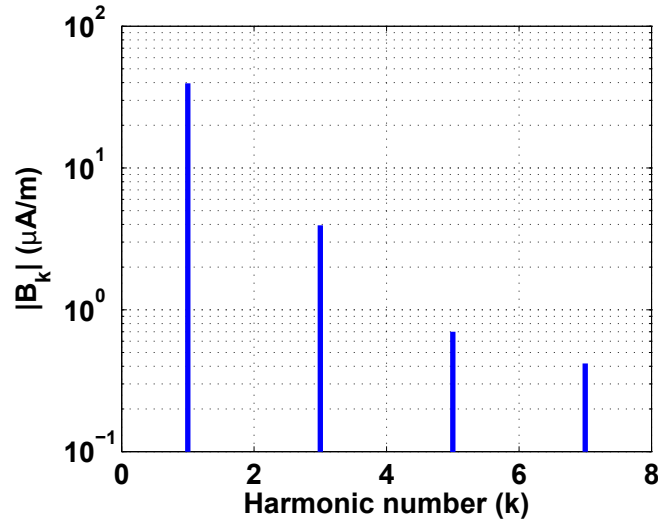


Fig. 2.14: The magnitude of quadrature Fourier components B_k of the total current per unit width from Fig. 2.13. The even harmonics do not appear on the graph because their magnitudes are much smaller than $10^{-2}\mu\text{A}/\text{m}$.

applied AC voltage. The existence of harmonics beyond the third implies that the non-linearity is not just due to the ambivalence. This added non-linearity is due to the non-linearity of the $C - V$ modulation. The dip in the fifth harmonic (around $V_{ac} = 4$ V) is due to the $C - V$ behavior of the varactor. The ratio between the first and 3rd harmonics $B_1/B_3 > 100$ for $V_{ac} \ll V_{pi}$ and it drops to B_1/B_3 3.6 at $V_{ac} V_{pi}$.

2.3 Design and analysis of the tunnelling relay

As discussed in chapter 1, there is a need for a CMOS successor. One of the main issues that must be considered in finding this successor is its power consumption; thus any successor of the CMOS must have two attributes: high ON-OFF current ratio to enable low static power consumption, and low opera-

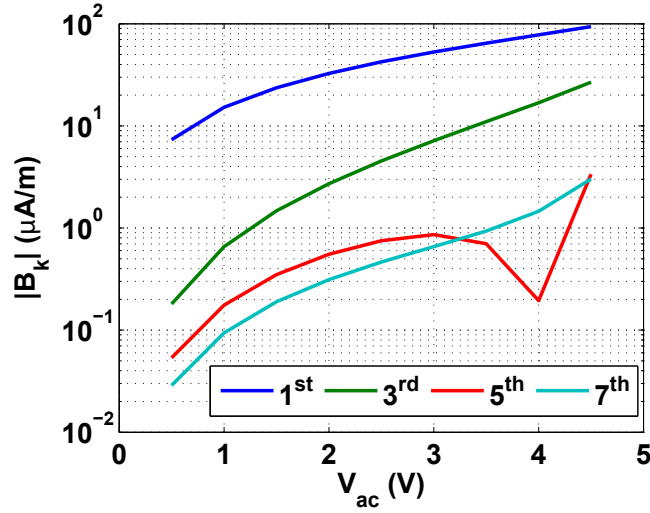


Fig. 2.15: The harmonic components B_k of varactor current versus AC amplitude V_{ac} for the suspended graphene varactor described in 2.12, where $V_{pi} = 4.7$ V, $L/W = 25$, and $V_{dc} = 0$.

tion voltage V_{DD} to enable low dynamic power. EMRs are a front runner to fill this void due to their extreme ON-OFF current ratio. In this section we propose the suspended graphene tunneling relay as a nanoscale EMR with lower operation voltage. We analyze its electrical characteristics and suitability for applications in digital circuits.

2.3.1 Structure and operation of graphene relays

Fig. 2.16A) depicts the structure of the proposed graphene relay, illustrating its three terminals. The first terminal is the suspended graphene membrane which is connected to a constant voltage. The second terminal is an underlying gate electrode that is used to actuate the suspended membrane. The contact is made through an elevated electrode, which is insulated from the gate by an ultra thin layer of wide band gap dielectric.

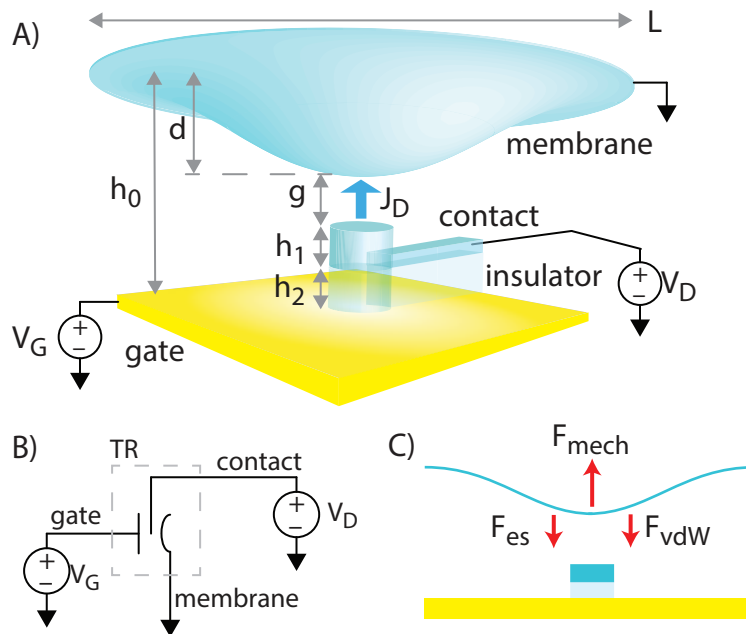


Fig. 2.16: (a) Schematic of a tunnelling relay (TR), including a suspended graphene membrane, gate electrode for electromechanical actuation of membrane motion, and contact electrode atop a gate insulator layer. Critical TR dimensions including the tunnelling gap g are indicated in the diagram. (b) Circuit symbol for a TR. (c) Force diagram for the suspended graphene membrane, including the electrostatic force F_{es} , van der Waals force F_{vdW} and mechanical strain force F_{mech} .

The air/vacuum gap between the electrodes in the proposed graphene relay is below 50nm, we therefore take into account the van der Waals - Casimir force. The narrow gap also allows significant quantum tunnelling current between the electrodes, particularly when membrane deflection is actuated by an applied potential. This tunnelling current is modulated by the electrostatic actuation, hence the graphene relay combines the operation of EMRs and TFETs making it a tunnelling relay (TR). In analogy to FETs, the suspended membrane acts as the source, while the elevated electrode acts as a drain, the source-drain current density J_D is modulated by the gate voltage. The tunnelling current increases as the membrane deflects closing the gap between the source and drain. When physical contact is achieved the current density is determined by the contact resistance between the two electrodes. We propose a drain electrode made of few layer graphene, and we approximate the contact resistance by the resistance across the basal planes of graphite, which has a resistivity of $\sim 1\Omega\mu\text{m}$ at room temperature[101]. Fig. 2.16B) shows the proposed circuit symbol for the TR.

The contact area needs to be chosen to avoid irreversible adhesion between the suspended membrane and the drain electrode and minimize or avoid altogether the hysteresis associated with pull-in. To achieve that the strain energy stored (E_{mech}) in the membrane must be larger than the adhesion energy (E_{vdW}) between the drain electrode and the suspended membrane, which allows the immediate release of the membrane once the electrostatic force vanishes. The adhesion energy between graphene sheets is estimated to be $\sim 60\text{meV}/\text{atom}$ [102]. This adhesion energy is the minimum irreversible en-

ergy consumption in each switching cycle.

2.3.2 Equation of motion and tunnelling current

There are three forces acting on the suspended membrane as depicted in Fig. 2.16C): the electrostatic force (F_{es}), the van der Waals-Casimir force (F_{vdW}), and the mechanical restoring force (F_{mech}); the strain restoring force is the only mechanical restoring force taken in consideration. At equilibrium, these forces are balanced

$$F_{mech} = F_{es}(Gate) + F_{es}(Drain) + F_{vdW}(Gate) + F_{vdW}(Drain) \quad (2.11)$$

where $F_{es}(Gate)$ is the electrostatic force between the gate and the membrane, and $F_{es}(Drain)$ is the electrostatic force between the drain and the membrane. The van der Waals-Casimir forces attracting the membrane are named in the same manner: $F_{vdW}(Gate)$ towards the gate and $F_{vdW}(Drain)$ towards the drain. $F_{es}(Drain)$ can be neglected as the drain area is $100 \sim 1000$ times smaller than the gate area. Nevertheless, we cannot neglect $F_{vdW}(Drain)$ as it is inversely proportional to the gap raised to the fourth power. The gap between the membrane and the drain contact can be determined implicitly from Eq. 2.11.

The current density J_D is then determined from the gap g between mem-

brane and drain using a Landauer-Buttiker formalism:

$$\begin{aligned}
 J_D &= \frac{e}{h} \times \int [\rho_S(E)f_S(E) - \rho_C(E)f_C(E)] \times T(E)dE \\
 &\approx \frac{e^2}{h} \times n \times T(\Phi) \times V_{DS},
 \end{aligned} \tag{2.12}$$

where ρ_S and ρ_C are the 2D electron density of states of the suspended graphene source and fixed graphene drain respectively, f_S and f_C are the source and drain Fermi functions, and the vacuum tunnelling probability that controls the current is $T(\Phi) = \exp(-2\sqrt{2m\Phi}/\hbar g)$ where $\Phi = 4.6\text{eV}$ is the graphene work function [103]. V_{DS} is the drain-source voltage. Fig. 2.17 illustrates the tunneling current versus drain-source voltage at different gate voltages.

The actuation voltage is defined as the gate voltage required to achieve physical contact between the source and drain. Fig. 2.18 illustrates how this voltage scale with the diameter of the drain electrode (D_C) under the constrain of $E_{vdW} = 0.5E_{es}$ to ensure membrane release and avoid hysteresis.

2.3.3 Sub-threshold slope, dynamic energy, and delay time

While gate voltage indirectly modulates the tunnelling current in TFETs, it directly modulates the barrier length in the TR resulting in direct exponential current modulation. Fig. 2.19 shows numerical simulation of the change in J_{DS} with applied gate voltage. It demonstrate an extreme sub-threshold swing of 10mV/decade, which exceeds the 60mV/decade thermionic limit of MOSFETs.

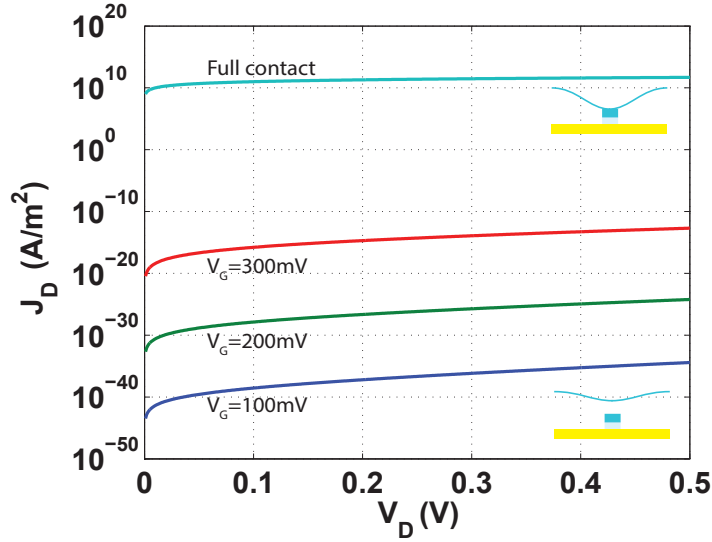


Fig. 2.17: Tunnelling current J_D versus applied contact voltage V_D , with V_G as a parameter and $V_S = 0$. The device dimensions are $L = 800$ nm, $h_0 = 16$ nm, and $h_1 + h_2 = 8$ nm. These dimensions are used in all TR simulations in this section.

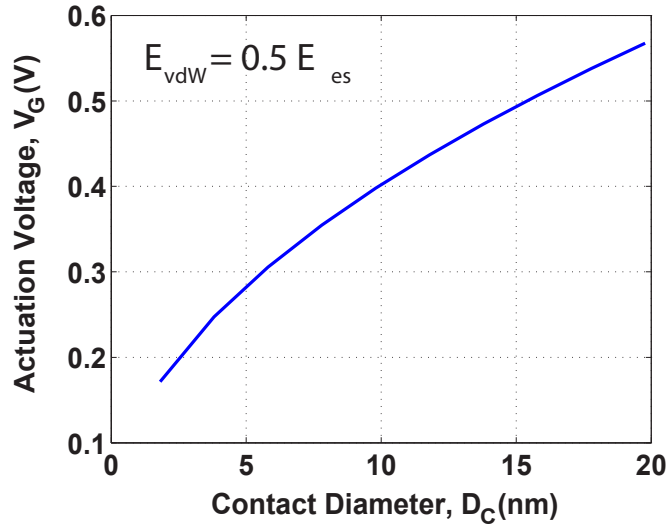


Fig. 2.18: Scaling of actuation voltage V_G versus contact electrode diameter D_C under the constraint $E_{vdW} = 0.5 E_{es}$.

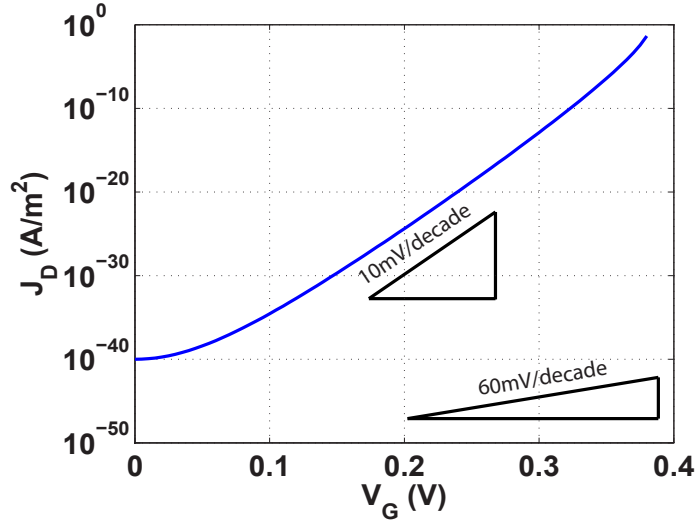


Fig. 2.19: Tunnelling current J_D versus gate voltage V_G at fixed contact voltage $V_D = 0.5\text{V}$. A mean sub-threshold swing of $S \sim 10\text{mV/decade}$ is predicted.

In the regime where $F_{es} \gg F_{vdW}$, the membrane deflection $d \propto V_G^{2/3}$. We can use this relation to derive a closed form expression for the sub-threshold swing as

$$S = \ln 10 \times \frac{1}{-2\kappa} \times \frac{\partial V_G}{\partial g} \approx \ln 10 \times \frac{3}{4} \times \frac{V_G}{\kappa \times d}. \quad (2.13)$$

where κd is the evanescent decay of the electron wave-function into the tunneling gap. Low sub-threshold swing is predicted for TRs owing to their low actuation voltage and their high tunnelling barrier.

Other important performance indicators are delay time (τ), ON-OFF current ratio (I_{ON}/I_{OFF}), and dynamic energy consumption $E_D = C_L V_{DD}^2$, where C_L is the load line capacitance. These indicators while individually important

52 Theoretical analysis of suspended graphene varactors and relays

they combine to determine the over all power consumption:

$$P = C_L V_{DD}^2 \left(\alpha \times f + \frac{I_{OFF}}{I_{ON}} \times \frac{1}{\tau} \right), \quad (2.14)$$

where α is the logic activity factor and f is the clock frequency. Fig. 2.20A) shows the predicted dynamic energy per cycle versus switching voltage. With operating voltage potentially between 0.1V and 0.5V, the TR promises to reduce the dynamic energy per cycle down to 1% of the value required for state-of-the-art 0.93V CMOS.

The predicted mechanical delay time of TRs illustrated in Fig. 2.20B) is also very promising, because delay times below 0.2ns can be achieved theoretically. This low delay time enables clock frequencies over 1GHz. The delay time τ was estimated by numerical integration of Newton's second law, $F_{es} + F_{vdW} - F_{mech} = m d^2g/dt^2$ over the deflection distance. We neglected the damping, justified by the high quality factors of suspended graphene resonators[5, 78]. Extreme ON-OFF current ratios are also predicted, since the off current is quantum tunnelling current while the on current is a current through the off-plane ohmic resistance of graphite. The theoretical model predictions shown in Fig. 2.17 suggests that I_{ON}/I_{OFF} can reach 10^{40} , which is an advantage of EMRs in general.

2.3.4 Inverter model

A TR can be used as either an n-channel transistor or a p-channel transistor: its polarity is determined by the suspended membrane bias voltage. If the membrane is connected to a high, the TR voltage it turns on when low

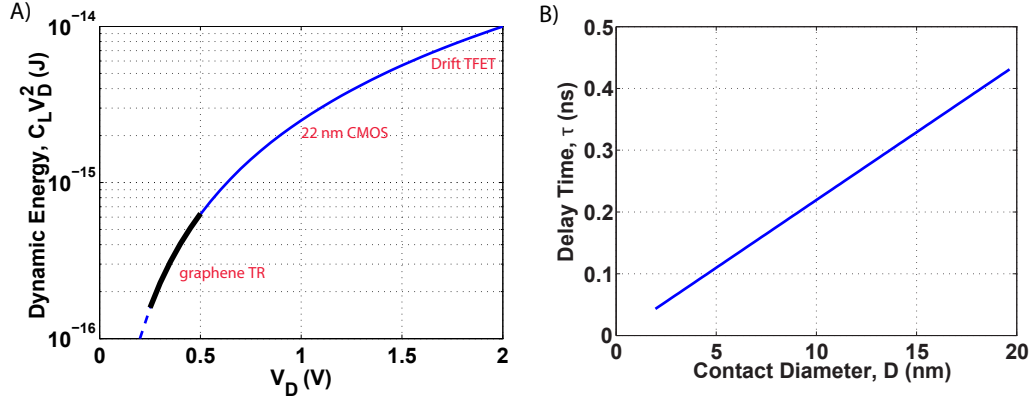


Fig. 2.20: A) The dynamic energy consumed with a representative load capacitance $C_L = 2.5$ fF versus operating voltage V_D . The proposed graphene TR, the experimentally demonstrated drift TFET[9], and the 22 nm CMOS low stand-by power node from 2011 report of International Technology Roadmap of Semiconductors [10]. B) Electromechanical delay time τ versus contact diameter D_C under the constraint $E_{vdW} = 0.5 E_{es}$. A sub-ns delay is predicted.

gate voltage is applied in the same way a p-channel transistor works. One the other hand, if the membrane is connected to a low voltage the TR turns on when a high gate voltage is applied in the same way an n-channel transistor works. Therefore, logic circuits can be built from TRs by connecting the correct bias to the suspended membranes. Fig. 2.21A) shows the schematic and circuit diagram of an inverter built from two connected TRs. The predicted input-output characteristics of the inverter are shown in Fig. 2.21B). The inverter demonstrates very promising operation with wide noise margins, steep transition, as well as a lack of hysteresis. The predicted steep transition is due to the TRs high intrinsic gain $\mathcal{A} = g_m r_0$ where $g_m = \partial J_D / \partial V_G$ is the transconductance and $r_0 = \partial V_D / \partial J_D$ is the output resistance. In the limit of

54 Theoretical analysis of suspended graphene varactors and relays

$F_{es} \gg F_{vdW}$ the intrinsic gain of a TR can be given by

$$\mathcal{A} = \frac{\partial J_D}{\partial V_G} \times \frac{\partial V_D}{\partial J_D} \simeq \frac{8}{3} \times \kappa d \times \frac{V_D}{V_G}. \quad (2.15)$$

As with the extreme sub-threshold swing, the intrinsic gain \mathcal{A} is determined by the evanescent wave-function decay κd into the gap. The intrinsic gain of the devices considered here is predicted to be $\mathcal{A} \sim 100$, which is suitable for most applications. All combinational and static memory circuits can be built using TRs. Fig. 2.21C) depicts a universal NAND gate built from four tunnelling relays.

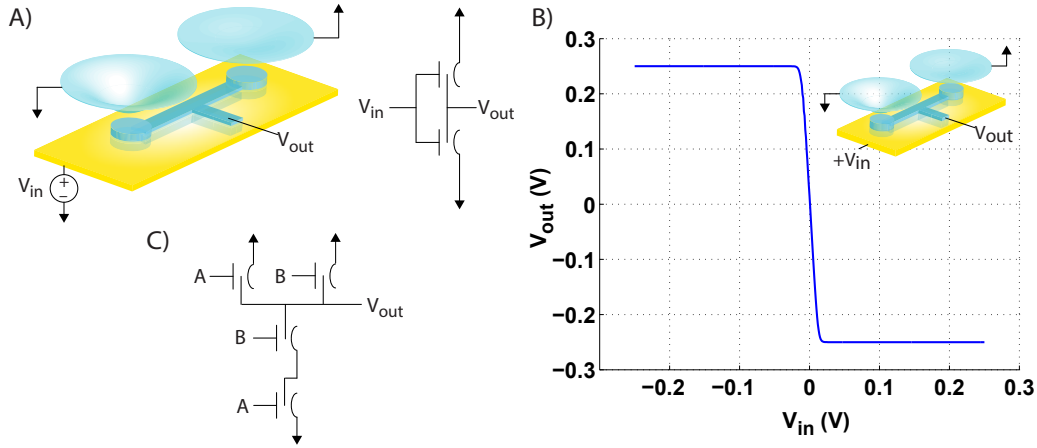


Fig. 2.21: A) Schematic and circuit diagram for a TR inverter, with input and output voltages V_{in} and V_{out} respectively. B) The transfer characteristic of an inverter built from two tunnelling relays with the geometry of Fig. 2.17. C) Circuit diagram for a universal NAND logic gate composed of TR switches, with inputs A and B .

2.4 Summary

In this chapter we proposed a model for electrostatic actuation of suspended graphene membranes, which assumes a hinged suspension edges. This model takes into consideration the non-uniform and changing nature of electrostatic actuation. From this model we predict that pull-in will happen at $d = 0.6h$ instead of $d = h/3$ for Hookean suspensions. We then proposed a suspended graphene varactor (SGV). Based of the model developed the suspended graphene varactor offers a tuning range of 76% exceeding the 50% limit for Hookean parallel plate varactors. Varactors with operating voltage ≤ 1 V are predicted due to the low elastic stiffness of graphene. We then investigated the AC response of the SGV to signals below its resonant frequency. We expect odd harmonics to be created. Finally, we investigated the use of graphene switches as EMRs. We proposed the suspended graphene tunneling relay. It promises actuation voltage as low as 0.25 V due to the low elastic stiffness of graphene, which would enable the reduction of dynamic energy consumption to only 1 – 7% of the dynamic energy of contemporary 0.93V CMOS [10]. We also predicted that extreme sub-threshold swing and high intrinsic gain can be achieved due to tunneling conduction through vacuum.

Chapter 3

Suspended graphene varactor fabrication

This chapter discusses the fabrication process of SGV, illustrating the challenges that we faced and how we addressed them. The main challenge was to fabricate large arrays of graphene suspensions with aspect ratios $L/h > 10$ at a high yield $> 90\%$. We were able to overcome this challenge by developing a transfer process that uses a hardened PMMA handle to protect the graphene during transfer and drying. Then we removed the PMMA handle using a gentle process that avoids heating. We were able to achieve a high suspension yield $\geq 95\%$ and an areal capacitance density of 12 pF/mm^2 for varactors comprising thousands of suspensions.

3.1 Target device and initial trials

Large arrays of suspensions are needed to achieve pF capacitance in SGVs. Fig. 3.1 shows the ideal structure for a SGV. The ideal varactor performance can be achieved through: patterning the underlying electrode eliminates parasitic capacitance, using large area graphene and small ratio of trench length to trench separation ensures highest variable capacitance per unit area, and contacting all suspensions with metal reduces ohmic losses. Despite the ap-

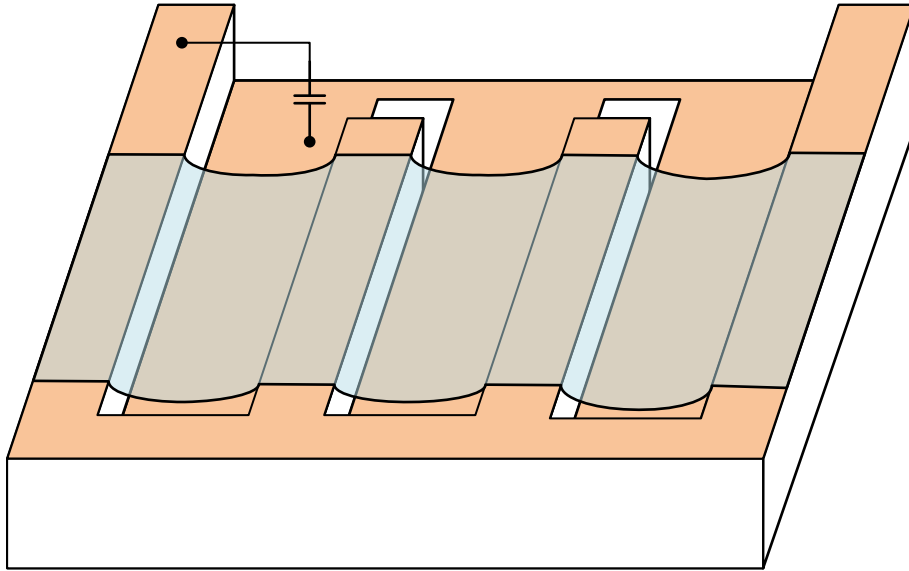


Fig. 3.1: Schematic of the ideal structure for a suspended graphene varactor.

parent simplicity of the structure, there are two fabrication issues: the manual transfer of graphene makes it difficult to suspend the graphene over only the trenches and using large area graphene traps liquids from the transfer inside the trenches. To avoid these issues the “proof of concept” device depicted

in Fig. 3.2 was developed. A silicon wafer with 300nm of thermal oxide grown on top will be used; the graphene will be suspended over trenches in the oxide, while the silicon will act as the fixed electrode. The graphene is prepatterned into strips to facilitate the drying process. Fig. 3.3 demonstrate

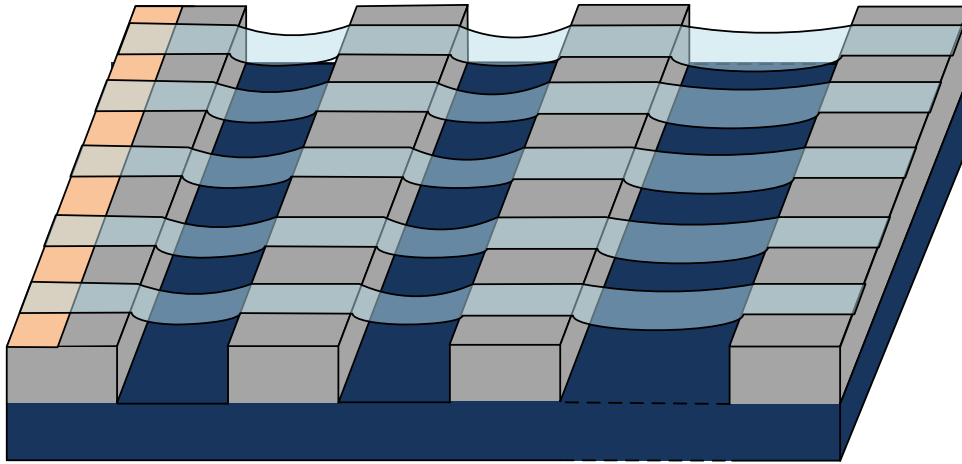


Fig. 3.2: Schematic of "proof of concept" structure for a suspended graphene varactor.

the process flow proposed to fabricate these devices, which consists of three main stages: substrate preparation, graphene growth and pre-patterning, and graphene transfer. The substrate is prepared by depositing metal contacts then etching the trenches. The graphene is grown using chemical vapour deposition (CVD) on copper, and then patterned into strips using oxygen plasma[78]. Afterwards, the copper is etched away and the graphene is transferred onto the substrate using a polymer handle. Finally the polymer handle is removed using acetone and the device is dried in a critical point dryer (CPD) to keep the graphene from collapsing. The devices were designed to have aspect ratios

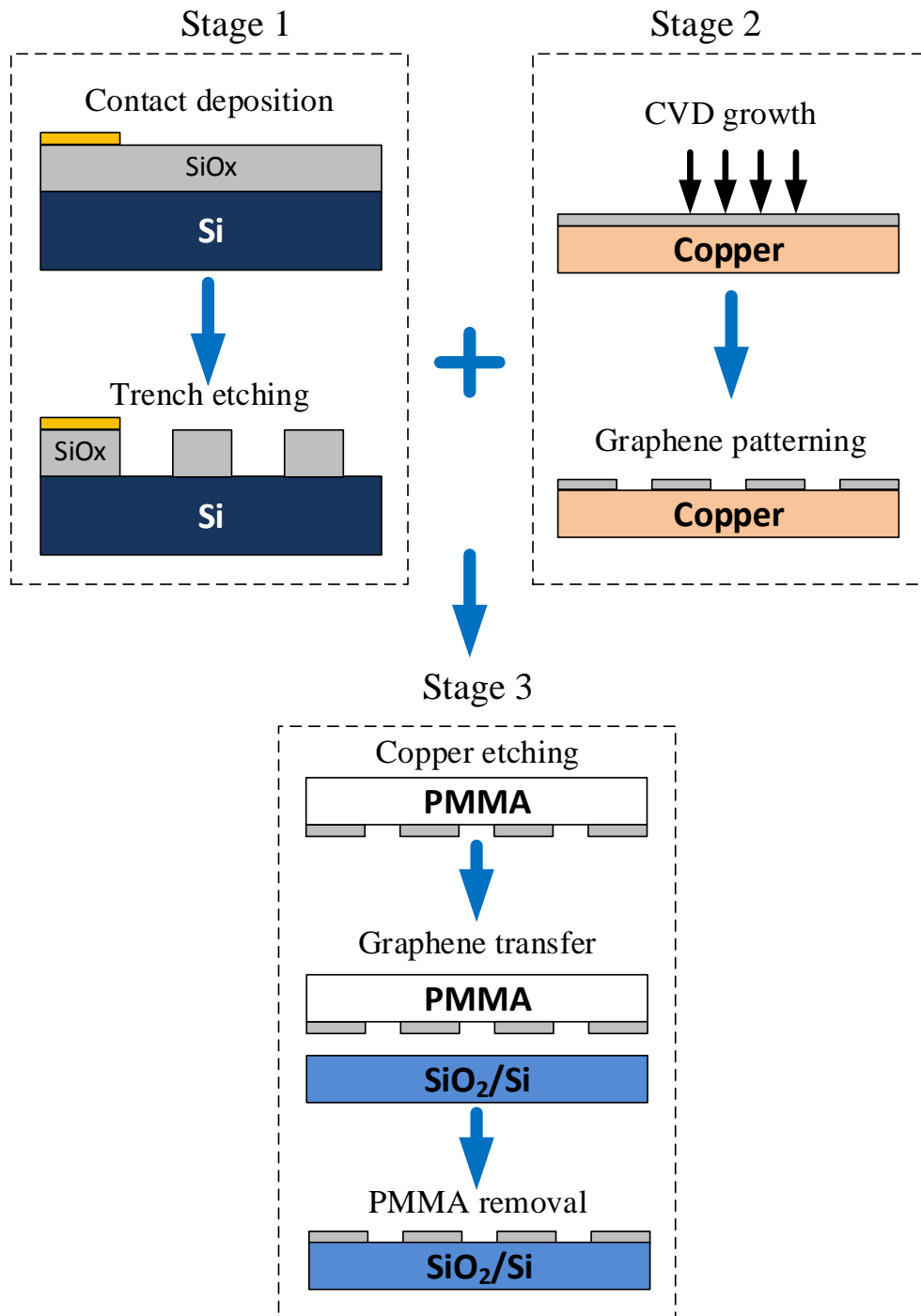


Fig. 3.3: A diagram of the proposed process flow illustrating the three stages of fabrication.

(L/h) below 10 in order to achieve good yield as reported in literature[78]. The yield reported in literature is $\sim 80\%$, which is low for a varactor. The yield here is defined as the ratio of the number of successfully fabricated suspensions to the number of suspensions intended in the varactor design (the product of the number of trenches and transferred graphene strips).

3.2 Challenges

The several challenges faced while fabricating the SGV can be divided into two categories: macroscopic challenges and microscopic challenges. The macroscopic challenges are mainly due to the manual transfer of graphene, while the microscopic challenges can be attributed to the transfer, the graphene and oxide qualities, and the device geometry.

3.2.1 Macroscopic challenges

The transfer is done manually by fishing the PMMA supported graphene from a DI water dish using the target substrate. This process may cause problems such as crumbling, rolling, and shifting of the graphene strips. Moreover, even if these problems were all avoided, it is very difficult to align the graphene strips orthogonal to the trenches. Fig. 3.4 shows an early trial that suffered from all these problems. The alignment issue was addressed by using alignment marks to show the direction of the graphene, nonetheless several trials and meticulous work are typically needed to achieve an angle close to 90° between trenches and strips, repeated trials may break the PMMA handle and destroy the graphene strips, therefore a thicker and stronger PMMA

handle was used. Another macroscopic challenge was the electrical isolation

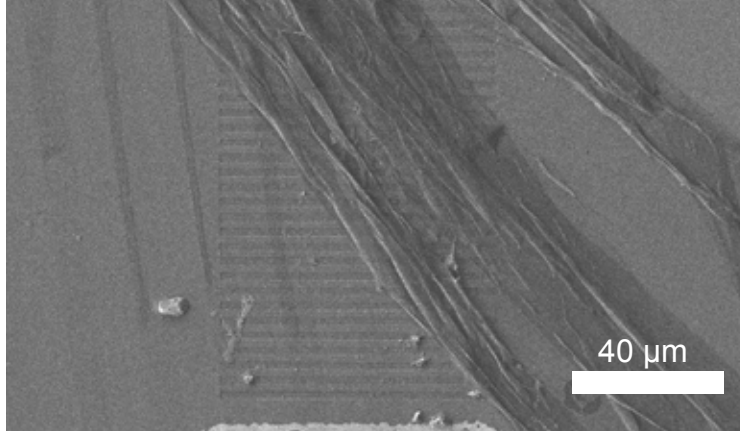


Fig. 3.4: An SEM image demonstrating the different problems associated with manual transfer.

of devices. The devices along the strips are connected to each other. Furthermore, the graphene may short the devices to the silicon wafer during manual transfer. This issue was addressed by cutting the graphene around each device using a profilometer stylus to ensure accuracy.

3.2.2 Microscopic challenges

The available fabrication processes imposed constraints on the device geometry. The smallest trench length (L) was $2\mu\text{m}$ due to the limitation of the photolithography process. The maximum trench depth (h) was the thickness of the oxide, which is 300nm . Another constraint was the workable aspect ratio, where literature surveys suggested that yields $> 80\%$ cannot be achieved for aspect ratios > 10 . These constraints limited the trench aspect ratio between ~ 6.7 to ~ 10 . Even with these aspect ratios, the graphene may collapse, break, or both. CVD growth creates graphene layers on both sides of the

catalyst copper sheet, the graphene on the undesired copper side leaves rolled up graphene residue that poses another problem as shown in Fig. 3.5. The collapsed suspensions and residue short the varactor, with a single collapse rendering the entire device inoperable. To solve this problem, the trenches were not etched all the way to the silicon, instead $< 50\text{nm}$ of oxide is left in the trench to help isolate the collapsed suspensions and the residue from the silicon.

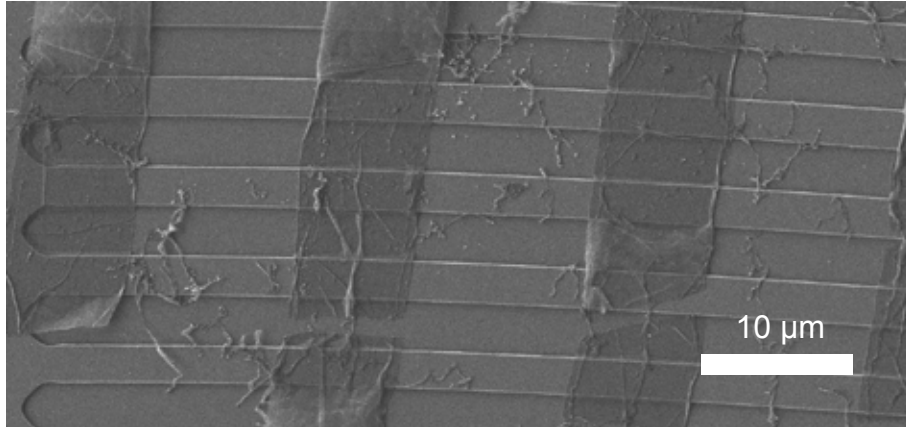


Fig. 3.5: An SEM image demonstrating the different problems associated with graphene suspensions.

The oxide isolation layer prevented the shorting of the graphene to the silicon, however it was not thick enough to with stand more than 2V without considerable conduction. Moreover the decrease in trench depth meant lower aspect ratio and lower yield. Therefore the overall performance was not improved. Further testing demonstrated that at least 100nm was needed to avoid conduction at high voltages (over 20V). A single aspect ratio $L/h = 2\text{um} / 200\text{nm}$ was thus identified as optimal for the proof-of-concept varactor demonstration.

3.3 Fabrication process

In this section the final optimized process is demonstrated, illustrating how the aforementioned challenges were addressed. The process consists of the three stages discussed before: substrate preparation, graphene growth and pre-patterning and transfer. Each stage is discussed in detail. Standard photolithography techniques are used for all patterning, etching, and deposition steps.

3.3.1 Substrate preparation

The devices are fabricated on low resistivity ($\rho \simeq 0.005\Omega\cdot\text{cm}$) silicon wafers with thermal oxide grown on both sides. The first step of fabrication is to remove the back oxide to enable the access to the silicon used as fixed electrode. The front side of the wafer is covered with $1.4\mu\text{m}$ of photoresist (S1813) and protective tape before immersion in Hydrofluoric acid (HF) to etch the back oxide. The wafer left in 10 : 1 diluted HF for 20 minutes. After removing the protective tape and the resist using acetone for 10 minutes, the wafer is moved to an isopropyl alcohol (IPA) for 5 minutes and DI water for another 5 minutes to remove the acetone residue. After the wafer is dried, it is ready for further processing.

The next step is to deposit metal contacts using a lift-off process and electron beam (e-beam) evaporation. After spinning $3\mu\text{m}$ of lift-off resist (LOR 5B) and $1.5\mu\text{m}$ of positive resist (S1813) the wafer is baked at 115°C for 60 seconds and exposed for 5 seconds to ultra violet rays at $90\text{mJ}/\text{cm}^2$ using the mask for metal deposition. The resists are developed in MF-319 developer for

45 seconds and rinsed in DI water for 5 minutes. After the wafer is dried, 10nm of Titanium (Ti) and 100nm of Gold (Au) are deposited using e-beam evaporation; the Ti layer is used for adhesion. The excess metal is removed with resist (lift-off) by immersing the wafer in “Remover 1165” at 70°C for 20 minutes with sonication. After that wafer is removed to a fresh beaker of Remover 1165 for another 10 minutes, then put in IPA and DI water for 5 minutes each to remove any Remover residue. Oxygen plasma is used to remove any organic residue on the wafer. Fig. 3.6 shows an overlap of the masks used for both contact deposition and trench etching.

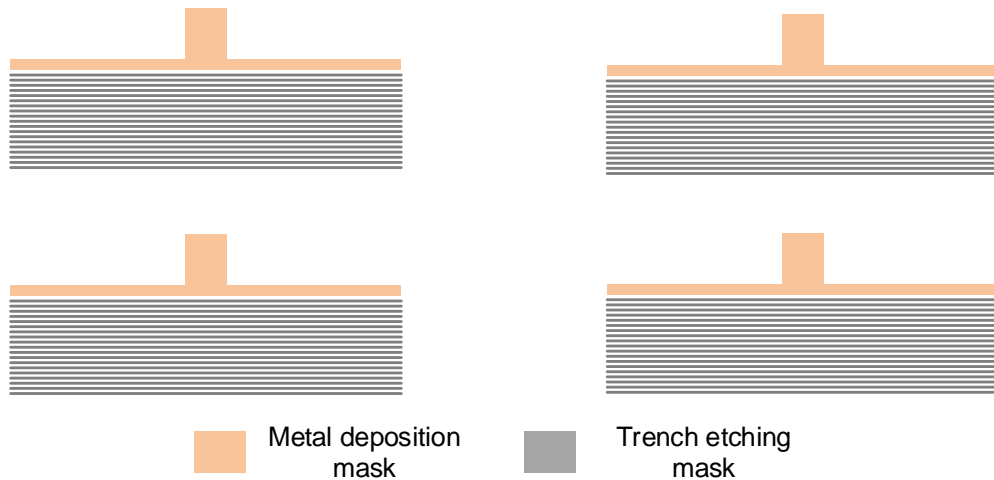


Fig. 3.6: Part of the two overlapping masks used for contact deposition and trench etching showing four adjacent devices. The mask represents the top view of the varactor.

The final step is to etch the trenches. The trenches are patterned using the same photolithography process as described above and etched using reactive ion etching (RIE). The etch chamber was cleaned before etching to ensure a reproducible controlled etch rate. The etch rates for narrow trenches differs

from the etch rate of wide trenches, which must be taken in consideration to reach the desired depth. The etching was done in an “Applied Materials P5000” RIE, and the recipe used is detailed in table 3.1. This recipe gives an etch rate of 340 nm/min for wide areas, 320 nm/min for trenches with length $5 \text{ nm} \lesssim L \lesssim 15 \text{ nm}$, and 300 nm/min for $L < 5 \text{ nm}$. These rates were calibrated through a series of test runs. The resist is then removed in the aforementioned manner, and oxygen plasma is used to ensure the cleanliness of the wafer. Fig. 3.7 shows an SEM image of the prepared substrate.

Table 3.1: Details of the Silicon oxide etch recipe.

Power	Pressure	gas flow	magnetic field
720 W	100 mT	CHF ₃ 45 scc	70 G
		Ar 70 scc	
		CF ₄ 7 scc	

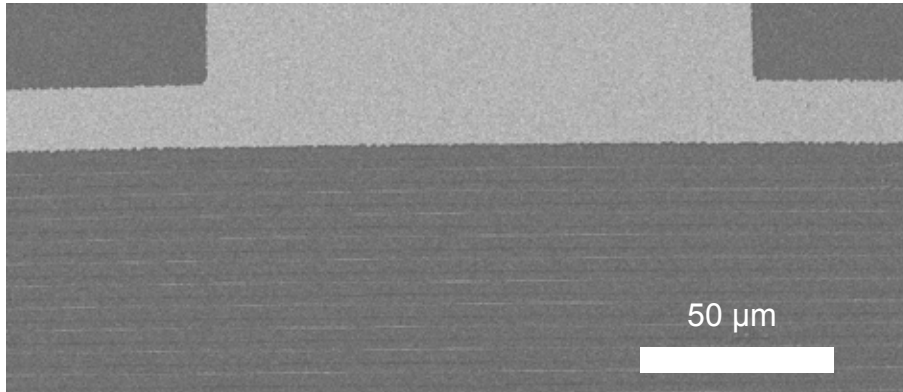


Fig. 3.7: Partial SEM of a fabricated substrate showing the trenches and metal contact.

The exact width and depth of the trenches were verified using an Asylum MFP3D atomic force microscope (AFM) in contact mode. The trenches were $2.45 \mu\text{m}$ wide and 155nm deep on average. Fig. 3.8 shows a contact mode

AFM line scan across two trenches.

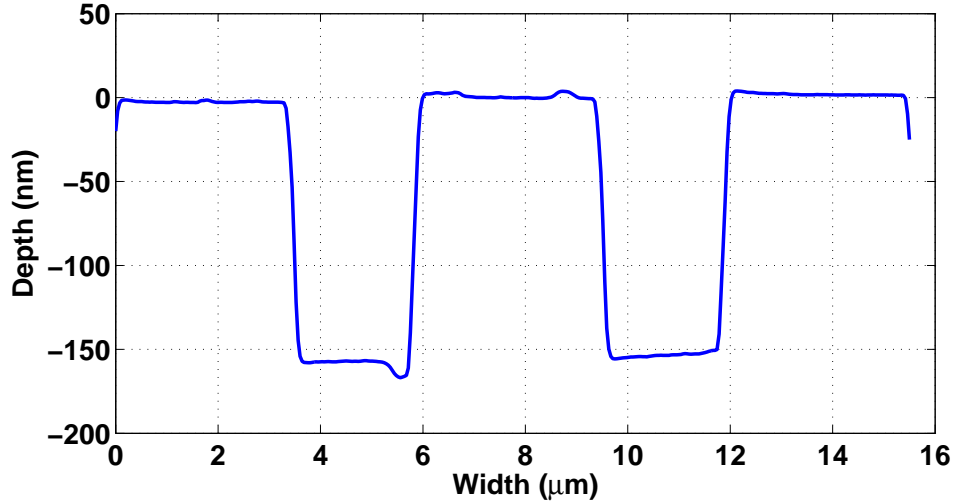


Fig. 3.8: A contact mode AFM line scan across two trenches.

3.3.2 Graphene growth and pre-patterning

We use large area graphene grown by a Farzaneh Mahvash and Mohamed Siaj using CVD[104]. We receive $1\text{cm} \times 1\text{cm}$ pieces of copper with single layer graphene grown on both sides. Graphene on one side is patterned with oxygen plasma using the same photolithography process as that used for the trenches. A representative part of the patterning mask is depicted in Fig. 3.9. The narrow strips are the desired patterns, while the wide strips act as alignment marks visible to the eye during the transfer process to show the orientation of the strips. After patterning, the photo-resist is removed by immersing the copper in acetone for 5 minutes. The copper is then put in IPA and DI water for 5 minutes each to remove any acetone residue. The copper is gently dried with a low pressure nitrogen gun.

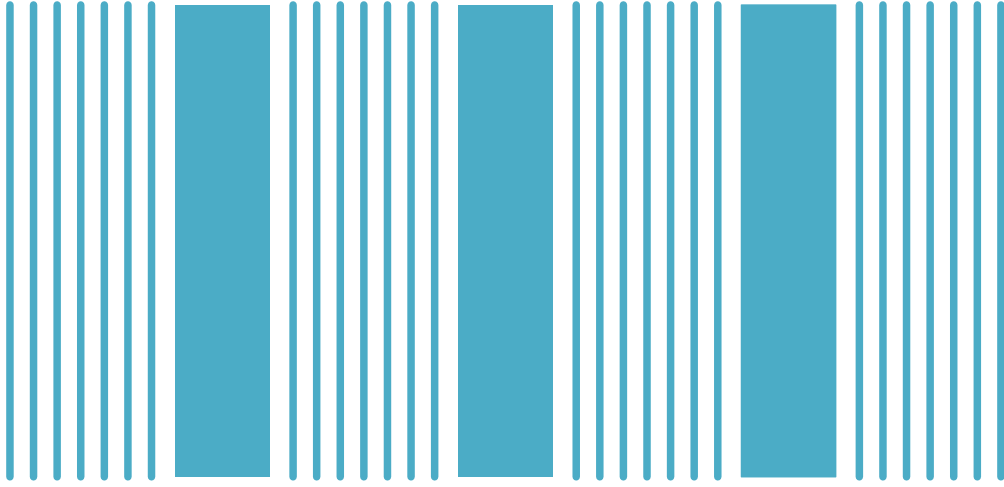


Fig. 3.9: Part of the mask used for patterning graphene. Continuous pieces of graphene are used as alignment marks.

After patterning, a 300nm PMMA 950 A4 handle is spun on the patterned side, and baked for three minutes at 90°C. The copper is then etched in a 0.1 M solution of ammonium per-sulphate ($(\text{NH}_4)_2\text{S}_2\text{O}_8$), the PMMA side is put facing up. The copper is etched 45 minutes \sim 60 minutes and once removed from the etch solution, the back side is sprayed with DI water to remove the back-side graphene. The copper is then replaced in the $(\text{NH}_4)_2\text{S}_2\text{O}_8$ beaker and left until it is fully etched, which usually requires \sim 18 hours.

3.3.3 Graphene transfer

After the copper is etched the PMMA supported graphene is scooped out of the etchant using glass slides as depicted in Fig. 3.10 and placed in DI water for 5 minutes. The graphene is then scooped and moved to a fresh beaker of DI water to remove all etchant residue. After 5 more minutes the graphene is

scooped out of the DI water using the target substrate; great care is needed to ensure the strips are orthogonal to the trenches. After transfer the sample is left to dry.

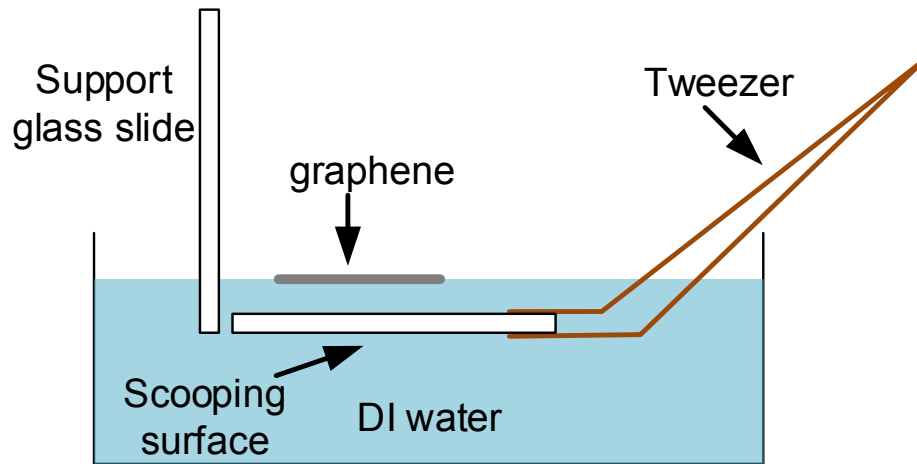


Fig. 3.10: A diagram showing how the PMMA supported graphene is scooped out of a liquid.

The PMMA is removed by putting the sample in acetone for 4 hours, and then moved to a fresh beaker of acetone for 15 more minutes. Afterwards, the sample is carefully and quickly moved to an IPA beaker and left for 5 minutes. This process is repeated twice to ensure all acetone residue is removed in order to put the sample in a critical point dryer (CPD). The sample is then carefully and quickly moved to a CPD chamber filled with sufficient IPA to keep the sample entirely immersed. One quarter of the chamber was used, and the purge time was 20 minutes.

After drying the sample, the devices are individually isolated by cutting the graphene around each of them using a profilometer stylus. Three working devices were fabricated using this process in the first run. The process was re-

peated to check the reproducibility of the devices, and two more devices were successfully fabricated. Fig. 3.11 shows SEM images of the fabricated suspended graphene varactor. Tunable capacitance per unit area was calculated from the SEM images, and tunable capacitance density up to $> 12\text{pF}/\text{mm}^2$ was achieved. The fabricated devices occupied an area of $1\text{mm} \times 120\mu\text{m}$ each, and comprises around 1200 suspensions per device with tunable capacitances between 0.87 pF and 1.4 pF depending on the strips geometry. This tunable capacitance density exceeds what can be achieved by traditional MEM varactors.

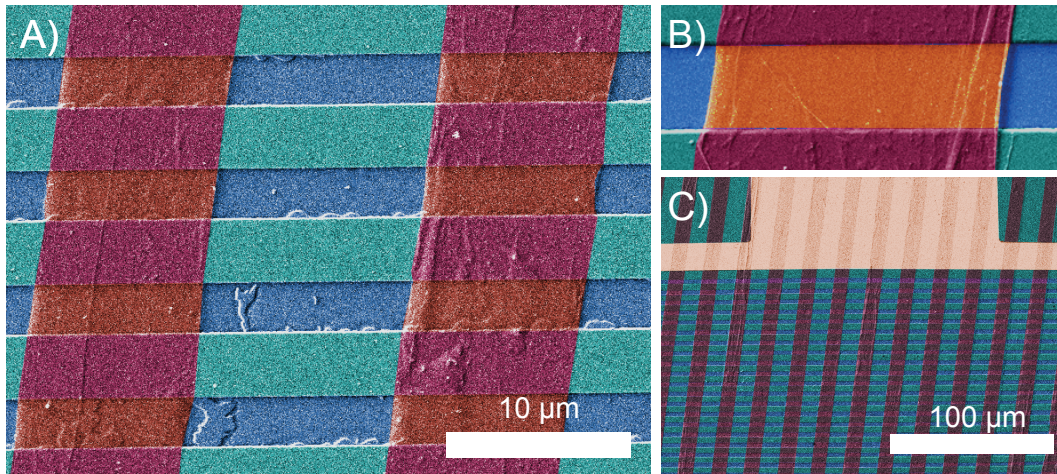


Fig. 3.11: False colour SEM images of the fabricated devices. A) Image of few suspensions. B) Magnified image of a single suspension. C) Low magnification image of one third of a varactor showing hundreds of suspensions.

The tunable capacitance and the graphene suspension yields of the 5 working devices are reported in Table 3.2, the yields were calculated from SEM images. The average yield for all fabricated devices is $\sim 95\%$ for trench aspect ratio ~ 16 , which exceeds the yields reported in literature.

Table 3.2: Tunable capacitance and yield for the fabricated devices.

Device no.	Tunable capacitance	Yield
1	1.4 pF	95%
2	1 pF	95%
3	1.05 pF	90%
4	0.87 pF	99%
5	1.03 pF	97%

3.3.4 Suspended graphene verification

Contact mode AFM imaging was used to verify the suspension of graphene; Fig. 3.12B) shows two cross section: the first is of two trench and the other is of a suspended membrane. The cross sections were taken $5\mu\text{m}$ apart as illustrated in Fig. 3.12A). The images were taken using an Asylum MFP3D AFM. The probe used was Bruker DNP-B with spring constant $k = 0.12\text{N}/\text{m}$. The AFM image show that the graphene start to deflect at the edge, which corresponds to the hinged boundary condition used in the modelling work.

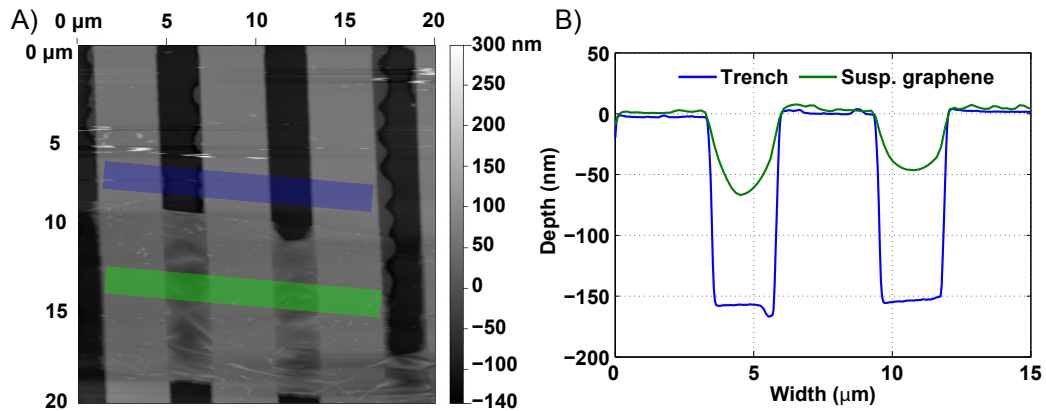


Fig. 3.12: A) A contact mode AFM image of the probed area showing the cross sections sampled across the trench and suspended graphene. B) Cross sections of trenches and suspended graphene.

The quality and number of layers of graphene can be probed using Raman

spectroscopy[105]. The number of layers can be determined from shapes of the G and 2D peaks[106], while the amount of defects is determined from the height of the D-peak[107]. We used a Renishaw InVia to do Raman spectroscopy. The pump wave length and power for these measurements were 514.5 nm and 12.25 mW respectively, and the exposure time was 25 seconds. The spectrum in Fig. 3.13A) shows a G-peak at 1595cm^{-1} , 2D-peak at 2694cm^{-1} , and a D-peak at 1353cm^{-1} . It demonstrates a D-peak to G-peak ratio ~ 0.075 , which shows that the process of patterning and transfer does not reduce graphene quality dramatically. The sharpness of the G-peak along with the high 2D to G ratio suggests that this is single layer graphene[105].

RIMATM instrument was used for hyperspectral Raman imaging to verify the continuity in the graphene over the device. The pump wave length and power used for imaging were 532 nm and 3 W respectively. Fig. 3.13B) shows a map of the 2D peak intensity over a $65\mu\text{m} \times 65\mu$. The image confirms that the graphene strips are continuous along the device. While Fig. 3.13C) shows a map of the 2D peak wave number shift for the same area.

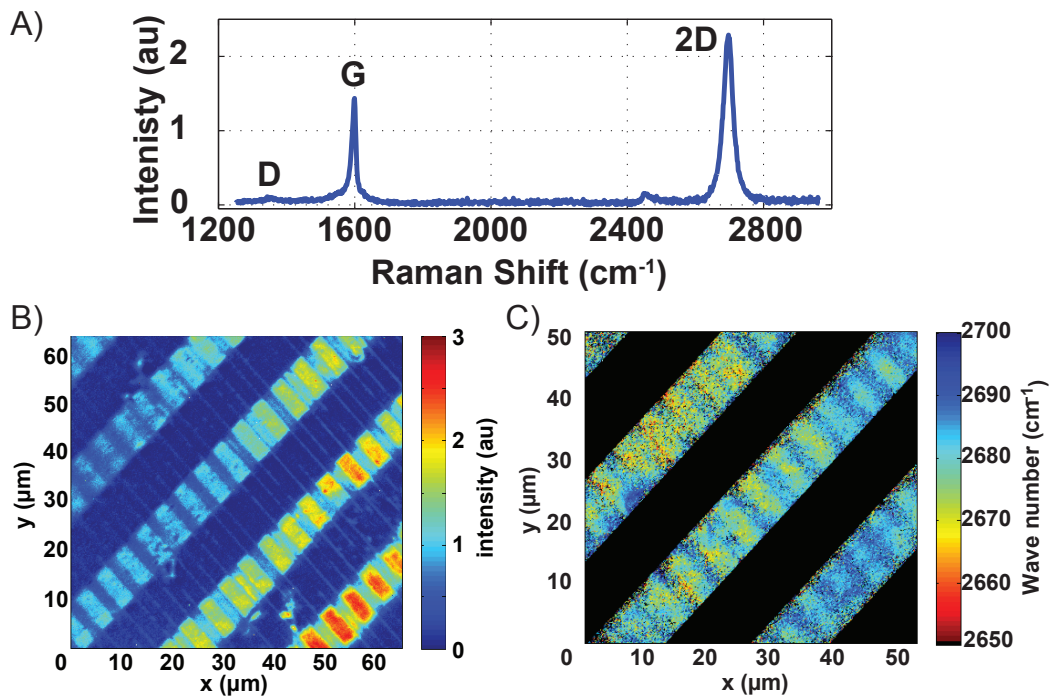


Fig. 3.13: A) Raman spectrum of the graphene after all processing and transfer. The pump wave length was 514.5 nm. B) Partial map of the 2D peak intensity of a suspended graphene varactor made using hyperspectral Raman imaging technique with a pump wave length of 532 nm. C) Partial map of the wave number shift of the 2D peak of the same area, where the black areas denote no peak.

Chapter 4

Varactor experimental characterization

This chapter demonstrates the performance of suspended graphene varactors. The capacitance versus voltage $C - V$ characteristics of the fabricated varactors were measured. A capacitance tuning of 55% was achieved with a 10 V actuating voltage, which exceeds the 50 % Hookean limit of conventional MEMS parallel plate capacitors. The theoretical model described in chapter 2 was used to fit the measured $C - V$ characteristics and extract effective Young's modulus and pre-tension values for the graphene suspensions. These properties were verified independently using Atomic Force Microscopy (AFM).

4.1 Linear Electrical Characterization

4.1.1 Test setup

The testing was conducted in vacuum to avoid dielectric breakdown of air between suspended graphene and silicon. The samples were enclosed in a probe station at a pressure $< 10^{-4}$ mbar and at room temperature. Fig. 4.1A) illustrates the setup used for testing. The graphene was contacted by landing a probe tip on the metal contacts, while the silicon was contacted through the chuck of the probe station as shown in Fig. 4.1B). When the varactor was not tested the two terminals were electrically connected to avoid charge build-up.

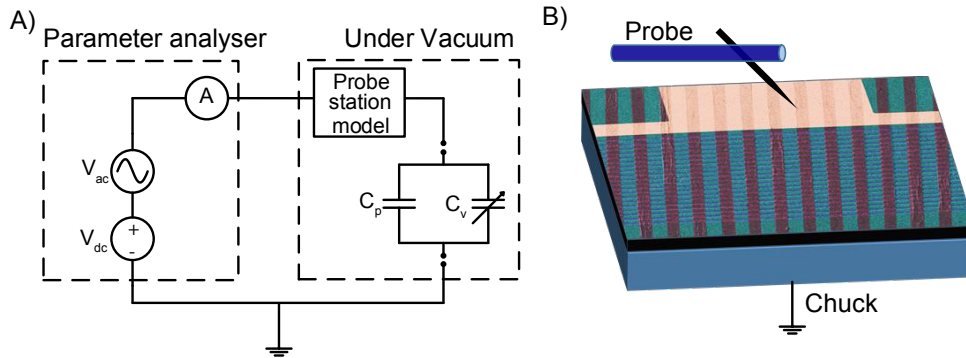


Fig. 4.1: A) The circuit schematic of the used for capacitance measurement. B) A simple diagram illustrating how the device is connected in the probe station. A metal probe is fixed to metal contact in the device, while the ground is connected to the silicon wafer. A false colour SEM image shows how the metal contact is connected to the suspended graphene.

A Janis Research ST-500 probe station was used. The probes, cables, and chuck of the probe station have finite parasitic impedances. To ensure accurate measurements, these parasitic impedances must be accounted for. Therefore we extracted the parasitic impedances of the probe station by measuring the impedance between the two terminals of the probe station (probe and chuck)

Z_{in} under three conditions: the probe and the chuck are not connected (open circuit), the probe and the chuck are connected (short circuit), and with a known load connected between the two terminals. Fig. 4.2A) shows the extracted circuit model for the probe station, while Fig. 4.2B) displays the measured and modeled short circuit impedance between the two terminals. The extracted model was used to correct for the probe station parasitics during device measurements.

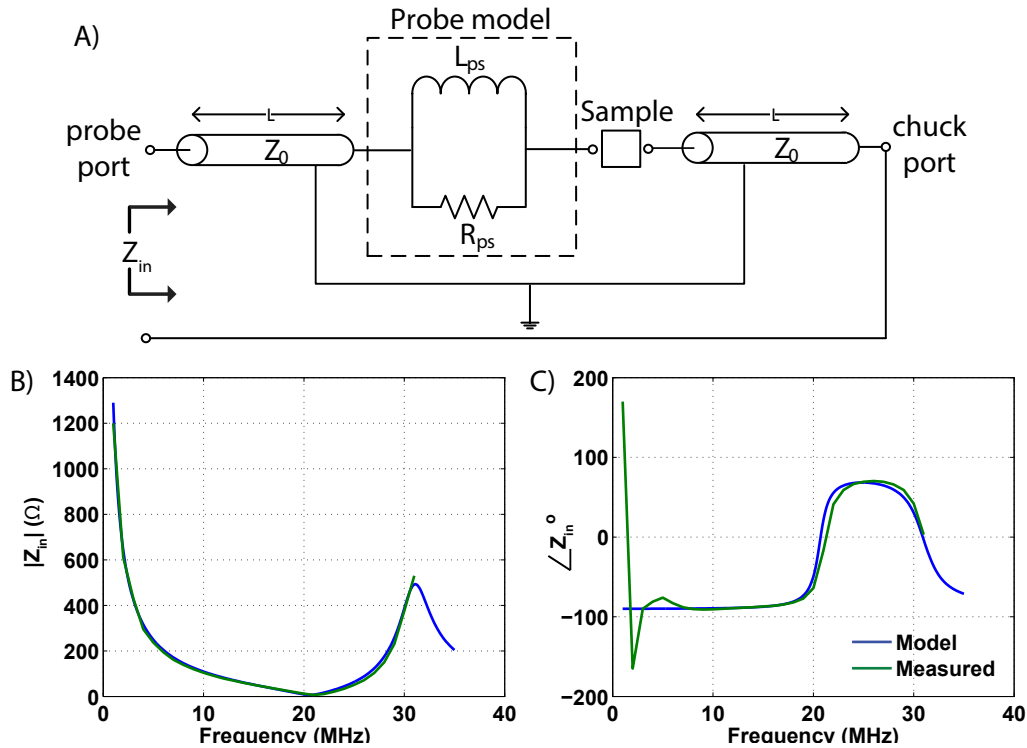


Fig. 4.2: A) The circuit schematic of extracted probe station model. The best fit model parameters are $L_{ps} = 0.75\mu\text{H}$, $R_{ps} = 1.55\text{k}\Omega$, $L = 61\text{cm}$, and $Z_0 = 50\Omega$. B) and C) The measured short circuit impedance Z_{in} between the probe station terminals. The short circuit was achieved by landing the probe directly on the chuck.

4.1.2 Capacitance measurement

The main test of a varactor performance is to measure its capacitance versus voltage ($C - V$) characteristics, through applying a DC bias voltage while measuring the capacitance with an AC signal. The bias voltage was increased from 0 V to 10 V. The five working devices were tested, and the theoretical model described by Eq. 2.4 and Eq. 2.6 was used to fit the measured $C - V$ characteristics. We maintained the assumptions that the suspensions have hinged edges and that the width of the suspension (W) is much larger than the length of the trench (L). All suspensions were actuated together and we could only measure the total capacitance, therefore the properties of individual suspensions could not be measured. Nonetheless, we extracted effective values for Young's modulus and pretension per unit width by assuming that all suspensions were identical. Table 4.1 contains the extracted values for each of the 5 measured devices. Although we neglected the effect of pretension in our initial proposal of the suspended graphene varactor, the experiment proved that pretension has a noticeable effect especially at low deflection values. These values were extracted by fitting the results to our model, and varying the fit parameters to approximate the uncertainty in the fit.

Table 4.1: Effective values for Young's modulus and pretension per unit width for the working devices.

Device no.	Young's modulus	Pretension per unit width
1	183 ± 15 GPa	45 ± 10 mN/m
2	180 ± 15 GPa	41 ± 10 mN/m
3	170 ± 15 GPa	50 ± 10 mN/m
4	180 ± 30 GPa	120 ± 25 mN/m
5	180 ± 30 GPa	150 ± 20 mN/m

Fig. 4.3 shows the relative change $[C(V_{bias}) - C(0)]/C(0)$ in tunable capacitance with bias voltage for device no. 2. A capacitance tuning of 55% was achieved, which exceeds the 50 % tuning range of a Hookean parallel plate varactor. The other 4 devices exhibited similar behavior. These $C - V$ measurements were done using the capacitance measurement module (CMU) of an “Agilent B 1500A” semiconductor device analyzer. The AC voltage V_{ac} used in these measurements had an amplitude of 30 mV and a frequency of 100 kHz. The amplitude was chosen to be sufficiently small not to cause any change in the membrane deflection, but in the same time the current created would be large enough for high signal to noise ratio measurements. The frequency was chosen to be orders on magnitude lower than the cut-off frequency of the probe station. Tunable and parasitic capacitances of the devices were calculated from the SEM images.

The Young’s modulus values extracted from the C-V measurements is lower than the 1 TPa reported for pristine single-crystal exfoliated graphene[92]. Nonetheless, it is in agreement with the values reported by [108] and [109] in 2011 for CVD grown graphene. These references report an elastic modulus 6 times lower than that of single-crystal exfoliated graphene. This degradation in graphene elastic modulus was attributed to the poly-crystalline nature of CVD graphene. However, in 2013 [110] reported mechanical properties of CVD graphene that are very close to those of single-crystal graphene. They attributed the degradation reported by [108] and [109] not to the poly-crystalline nature of the CVD graphene or the existence of grain boundaries, but to the weakening of these boundaries during the transfer process, especially due to

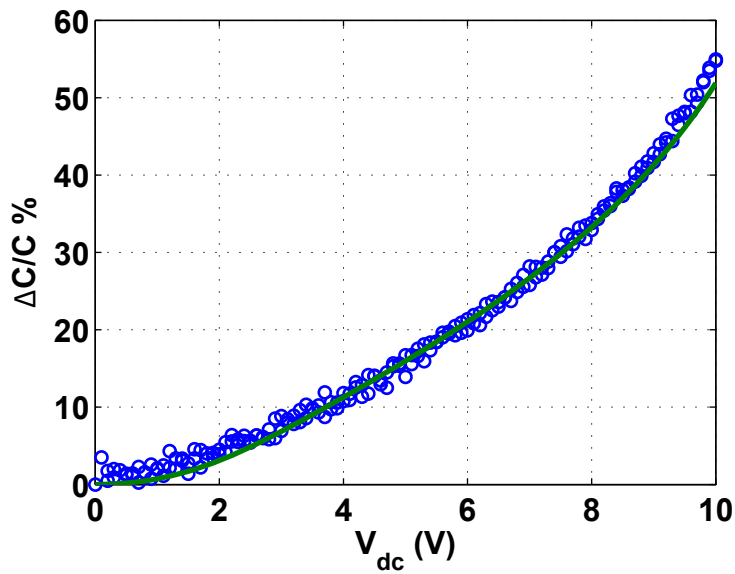


Fig. 4.3: The relative change in capacitance $[C(V_{bias}) - C(0)]/C(0)$ versus DC bias voltage. Both measurement and the theoretical model are depicted here. The capacitance change is calculated relative to the tunable suspended capacitance. The graph shows forward and backward measurement sweeps with no hysteresis. The model includes a pre-tension $S = 0.04 \pm 0.01\text{N/m}$ and a Young's modulus $E = 180 \pm 15\text{GPa}$.

the use of ferric chloride (FeCl_3) for copper etching and the baking of the polymer handle in air.

From these previously reported experiments we conclude that the degraded elastic modulus of our suspended graphene is due to the combination of using CVD graphene and the transfer process. Interestingly, Lower elastic modulus leads to lower actuation voltage, which is considered an advantage in a NEM varactor.

We note that the extraction of Young's modulus and pretension depends on an accurate determination of membrane and trench geometry. To check the systematic error arising from uncertainty in geometry, we give a simple error analysis. At equilibrium, where the applied bias voltage and membrane deflection are constant, we can infer that $S_0 \propto L^2/h^2$, in the domain where the pretension behavior dominates, from this relation the relative error in extracted pretension value $\Delta S_0/S_0$ can be estimated from the relative error in trench width $\Delta L/L$ and trench depth $\Delta h/h$ as $\Delta S_0/S_0 \approx \pm 2\Delta L/L \mp 2\Delta h/h$. While in the domain where the stretching behavior dominates, we can infer that $E \propto L^4/h^2$. Therefore the relative error in extracted Young's modulus value $\Delta E/E$ can be estimated as $\Delta E/E \approx \pm 4\Delta L/L \mp 2\Delta h/h$. Since the trench dimensions of the device represented in figure 4.3 were $L = 2.45\mu\text{m} \pm 68\text{nm}$ and $h = 155\text{nm} \pm 6\text{nm}$, we estimate the error in the extracted value of Young's modulus to be around 19 % and, the error in the extracted value of the pretension to be around 13%.

4.1.3 Direct current measurement

The design depicted in Fig. 4.4 enables the measurement of sheet resistance (R_{\square}) and field effect mobility (μ). Fig. 4.5A) demonstrates the DC $I_{ds} - V_{ds}$ curve of the fabricated SGV, from which we can calculate the total resistance between the two terminal $R_{ds} = V_{ds}/I_{ds} \sim 2\text{k}\Omega$ and the graphene sheet resistance $R_{\square} = R_{ds} \times \frac{W}{L} \sim 7\text{k}\Omega/\square$, which is considered high for graphene. The varactor had a time constant $\tau \sim 5\text{ns}$ and an electrical quality factor $Q \sim 300$ at 100 kHz, thus at 1 GHz we predict that $Q \sim 0.03$ rendering the use of the fabricated varactor at radio frequencies impossible. Nonetheless, if chemically doped graphene with $R_{\square} \sim 125\Omega/\square$ [111] is used to fabricate the same design, the quality factor will be improved to $Q \sim 2$. Fig. 4.5B) demonstrates the change in the current across the graphene I_{ds} versus back gate voltage V_g . We conclude that the graphene is p-doped, which is likely due to the photo-resist used in fabrication[112] or air doping by the water-oxygen redox couple active at the oxide surface[113]. We can calculate the field effect mobility $\mu = 820\text{cm}^2/\text{Vs}$.

4.2 Non-linear measurements

As discussed in chapter 2, the SGV is inherently non-linear due to its ambivalence to voltage polarity. We tested this ambivalence by sweeping the bias voltage between -10 V and 10 V, the result is shown in Fig. 4.6, which verified our prediction.

The test setup had to be adjusted as illustrated in Fig. 4.7A) to measure the non-linear current components. The higher harmonics were individually mea-

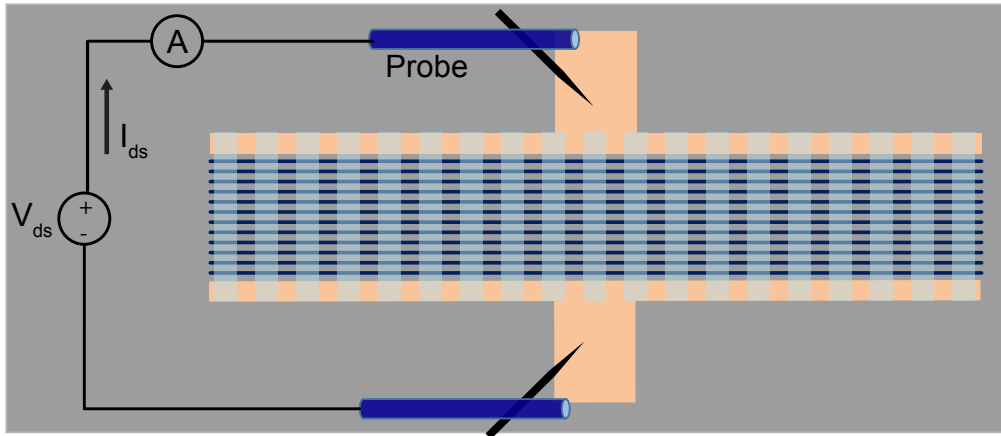


Fig. 4.4: Schematic of the three terminal device used for DC measurements. The gate voltage was applied through the probe station chuck.

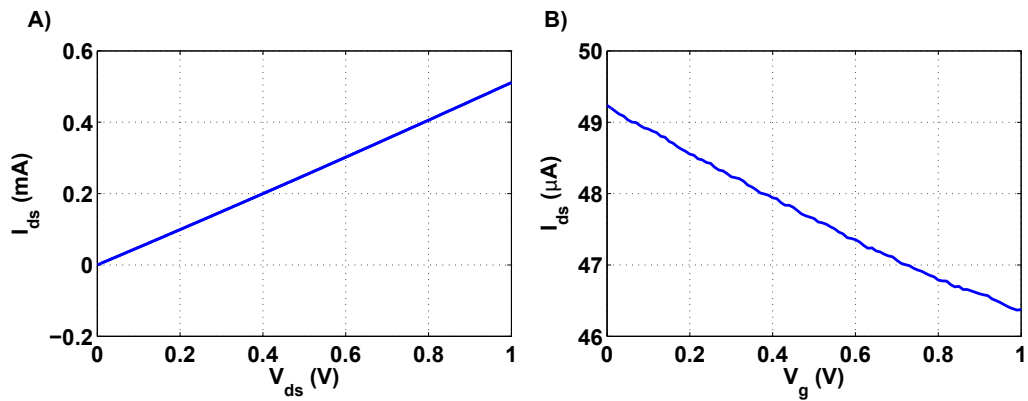


Fig. 4.5: A) Current across the graphene I_{ds} versus voltage across the graphene V_{ds} at bias voltage $V_g = 0$. The curve shows ohmic behavior. B) Current across the graphene strips I_{ds} versus gate voltage V_g at $V_{ds} = 0.1$ V.

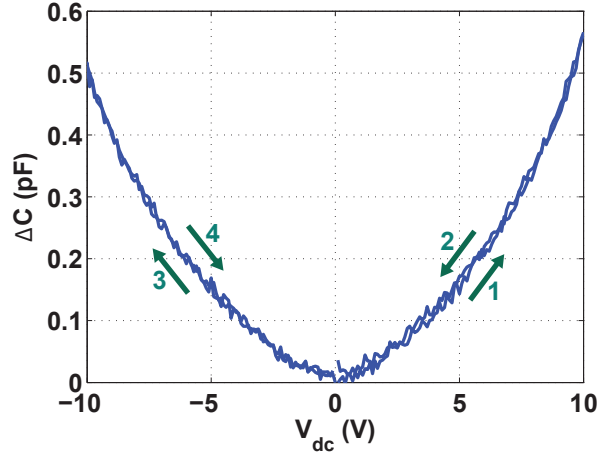


Fig. 4.6: Measured change in capacitance $[C(V_{bias}) - C(0)]$ versus bias voltage V_{bias} from -10 V to 10V. The figure shows capacitance ambivalence to the voltage polarity. The numbered arrows show the order in which the sweeps were done. The capacitance was measured using an excitation AC voltage of amplitude 30 mV and frequency 100 kHz.

sured using Zurich instruments HF2 lock-in amplifier with the HF2TA trans-impedance amplifier. We used the trans-impedance amplifier which converts current to voltage with a controllable gain because the lock-in amplifier measured voltage, but we need to measure the current. We used trans-impedance gain of 100 kV/A, at this gain setting the amplifier has a cut-off frequency ~ 3 MHz. Therefore, the trans-impedance amplifier hinders measurement for any driving frequency ≥ 1 MHz, although the expected resonant frequency of the suspended membranes is ~ 73 MHz. Fig. 4.7B) shows the increase in generated 3_{rd} harmonic current ($I_{3\omega}$) versus AC voltage. The measured currents agrees with the theoretical prediction.

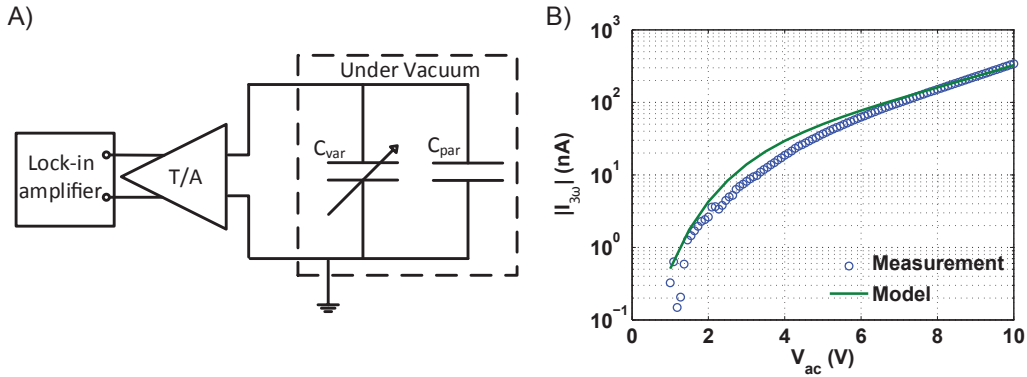


Fig. 4.7: A) Setup used for non-linear measurements. B) Measured and theoretically modelled third harmonic component of the varactor current due to a 20 kHz AC excitation. The amplitude of the AC signal was swept from 1 V to 10 V. The model includes $S = 0.04\text{N/m}$ and $E = 180\text{GPa}$.

4.2.1 Device lifetime

The varactors were modulated by a 10 V AC voltage for several thousand cycles. The life time of a typical device before significant loss of tunable capacitance (30%) is ~ 10000 cycles. The lifetime was calculated by measuring the time before a significant loss of tunable capacitance occurred due to the application of an AC voltage (V_{ac}) with amplitude 10 V and a known frequency (e.g. 1 kHz). Fig. 4.8A) shows the same area in a typical varactor before and after testing. The SEM images show a loss of 30% of the suspended membranes, which corresponds to an approximate 30% loss in tunable capacitance as demonstrated in Fig. 4.8B). We attribute this loss to the collapse of graphene suspensions.

A device with very wide graphene strips was fabricated and tested, in this device the deterioration starts as soon as it is tested and continue with each sweep as illustrated in Fig. 4.9A). We hypothesize that cracks and defects in

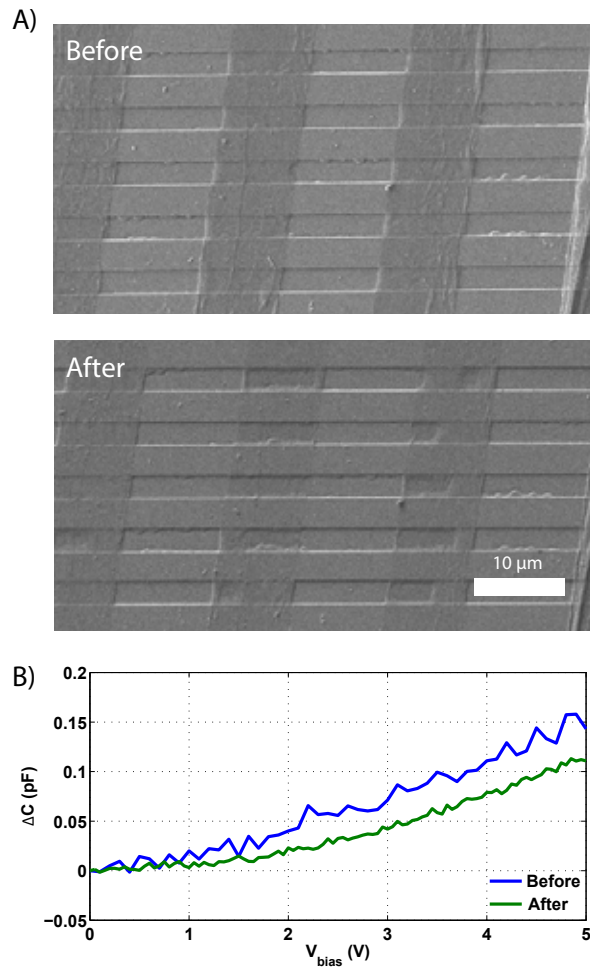


Fig. 4.8: A) SEM images before and after applying and AC voltage V_{ac} with amplitude 10 V and frequency 1 kHz for several seconds. It shows graphene suspension collapse. B) The capacitance change versus voltage for this device before and after applying the voltage.

the graphene, along with imperfections in the trenches, leads to collapse at voltages less than the nominal pull-in voltage of the ideal suspended graphene structure. Once collapsed, the graphene membranes suffer further collapse that is accelerated by the increased van der Waals - Casimir forces that result from the smaller gap between graphene and trench floor. The accelerated spread of collapse is suppressed in structures with thin graphene strips relative to structures with wide graphene strips, as expected from the disruption of pull-in with the presence of an increased number of gaps. Fig. 4.9B) shows a wide graphene suspensions with collapses spreading through it.

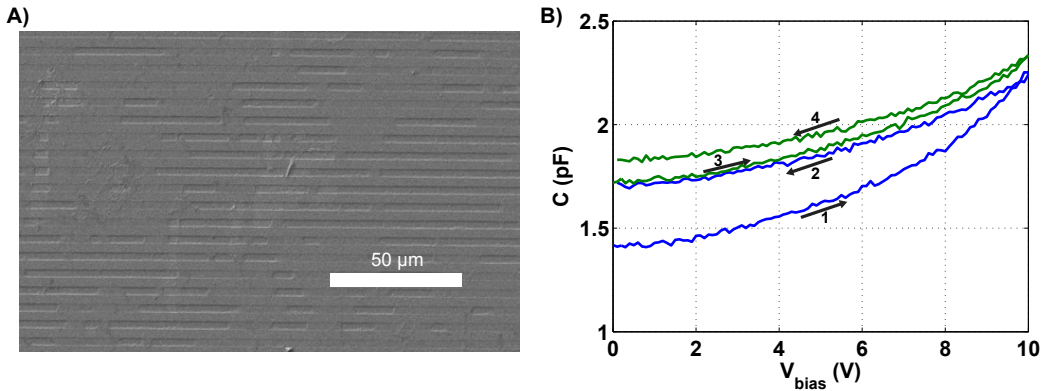


Fig. 4.9: A) SEM image of the collapses in a suspended wide strip. B) The suspended capacitance versus voltage for this device as it decayed.

4.3 AFM characterization of suspended graphene mechanical properties

The values of the Young's modulus E and pretension S_0 extracted from model fits to experimentally measured C-V curves were verified through the force-displacement ($F - D$) experimental protocol described in Whittaker

et al.[114] and Lee et al.[73], in which an AFM tip of known spring constant is used to probe a suspended membrane. The tested region is first imaged using contact AFM mode to determine the position of the suspensions. Then the geometric centre of the membranes is selected for probing. Fig. 4.10 shows two AFM images of the probed areas, where the white marks denote the indentation position.

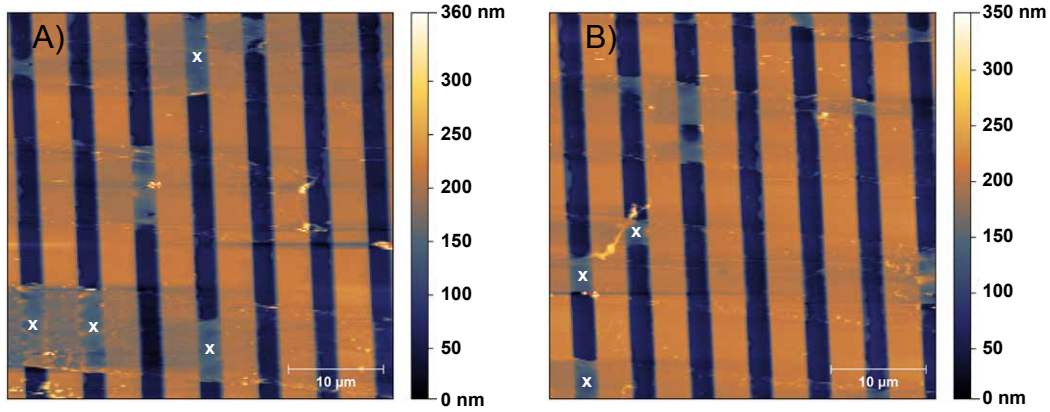


Fig. 4.10: Contact mode AFM images of two of the probed areas, where the white marks denote the positions of indentation.

The images and force displacement curves were acquired using an Asylum MFP3D AFM. Bruker MLCT-F tips were used for the measurements, the tips had cantilever spring constants between 0.9 N/m and 0.95 N/m. Before starting the measurement, the tips must be calibrated to determine two main parameters: the optical lever sensitivity (InvOLS) and spring constant (k). InvOLS is the output from the photodiode that results from a given deflection of the cantilever[115], it is calibrated by pressing the tip against a very hard surface (e.g. glass), this way the deflection of the cantilever ΔZ_{tip} corresponds directly to the change in piezo position ΔZ_{piezo} [116]. The spring constant is

calibrated by removing the tip as far as possible from the surface of the sample and measuring its thermal fluctuation[117]. The instrument interface software has step by step calibration procedure to facilitate the calibration.

To obtain accurate results the microscope was scanning for 20 minutes to reduce the x-y drift. Afterwards the positions of the indentations were chosen manually and each suspension was tested twice with a maximum force of 10 nN. The tip deflection ΔZ_{tip} versus the piezo position ΔZ_{piezo} is recorded as in Fig. 4.11A), after which the graphene membrane deflection shown in Fig. 4.11B) is extracted as $\Delta Z_{graphene} = \Delta Z_{piezo} - \Delta Z_{tip}$. Fig. 4.11C) depicts exerted force versus the graphene deflection. Fig. 4.11A) shows that when the tip first reaches the surface it is suddenly attracted downward to the surface, which gives negative deflection. As the piezo presses the tip, the cantilever starts deflecting upwards. It is very important to find the point at which the AFM tip deflection is zero to avoid the effect of the initial adhesion and obtain accurate results[?].

Thirty three membranes were tested twice to determine whether the indentation caused any damage or slippage in the suspension. If the results from the two tests agreed, this was interpreted to indicate that no damage occurred and the data was included for analysis. On the other hand, if the data from the two measurements did not agree to within the accuracy of the experiment, this meant some damage or slippage occurred and this point was excluded from the analysis. Fig. 4.12 shows the data from two different points, one accepted and one rejected. Afterwards, half of the included membranes were tested with an indentation force up to 150 nN to probe their non-linear behaviour.

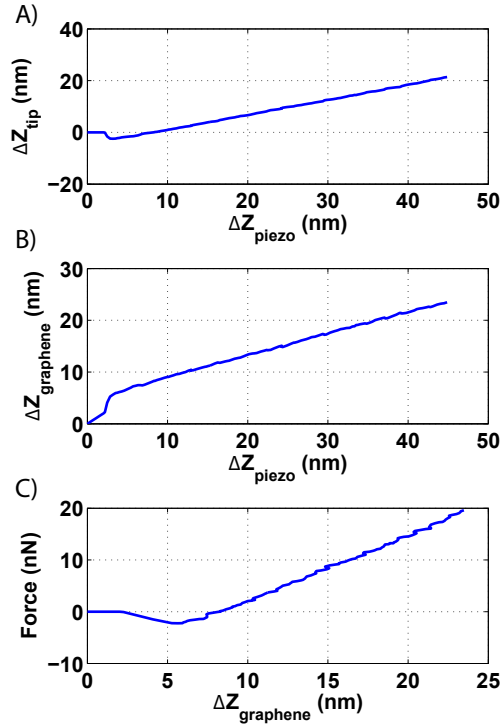


Fig. 4.11: Raw data from the force versus displacement experiment. A) The tip deflection ΔZ_{tip} versus the piezo position ΔZ_{piezo} . The graph shows an initial dip in deflection that corresponds to the sudden attraction between the tip and the surface as the tip reaches the surface. As the piezo presses on, the tip starts deflecting upward. B) The extracted graphene deflection $\Delta Z_{graphene} = \Delta Z_{piezo} - \Delta Z_{tip}$ versus ΔZ_{piezo} . C) The force applied by the piezo $F = k_{tip}\Delta Z_{tip} = k_{graphene}\Delta Z_{graphene}$ versus graphene deflection $\Delta Z_{graphene}$. The spring constant of the cantilever $k_{tip} = 0.92\text{N/m}$.

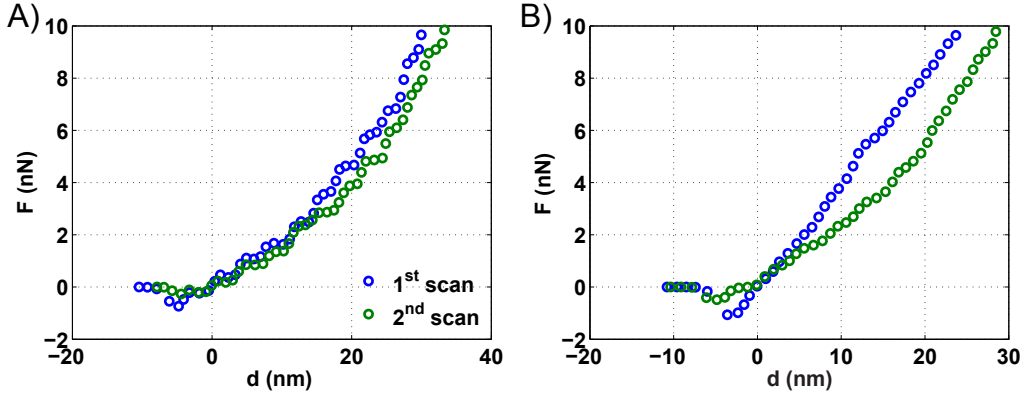


Fig. 4.12: A) $F - D$ curves for two indentations on the same suspension. The agreement of the data suggests that suspension was not damaged by the first indentation. B) $F - D$ curves for two indentations on a different suspension. The disagreement between the data suggests that suspension was damaged by the first indentation.

The behaviour of suspended graphene sheets under a perpendicular load is divided into two regimes: the small deflection regime that has a linear force deflection relation with a restoring force dominated by the pretension and the large deflection regime that has a non-linear force deflection relation with a restoring force dominated by the stretching of the membrane. There is no exact closed form relation describing the complete behaviour of a rectangular membrane deflection under point load, exact solutions can only be found for certain cases of circular membranes due to their axisymmetry[118, 76]. Therefore we divided the membranes into two groups: narrow membranes ($W \leq L$) that can be approximated as beams under small deflections[71] and wide membranes ($W > 2L$), for which we developed an approximation to describe their large deflection behaviour. Fig. 4.13A) shows typical linear behaviour of the membranes in the small deflection regime, where the force deflection relation can be approximated to $F \simeq \pi^2/2S_0W/L$, while Fig. 4.13B) shows the ex-

tracted pretension for 12 narrow devices versus W/L . The extracted S_0 values have a mean of 62mN/m and standard deviation of 24 mN/m, which is close to the value extracted from the $C - V$ measurement ($S_0 = 50\text{mN/m}$) for the same device.

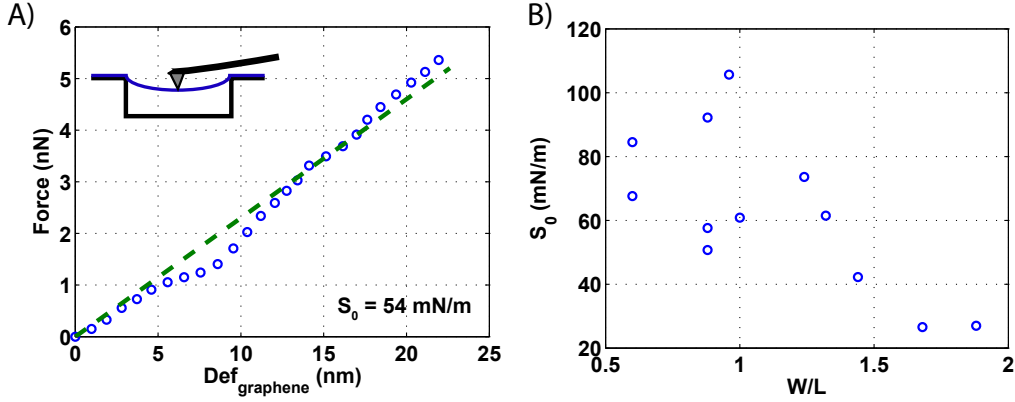


Fig. 4.13: A) Applied force versus displacement for a narrow membrane with a linear fit. The inferred S_0 value is 54 mN/m. B) The extracted S_0 values of 12 suspensions versus their W/L .

For the wide membranes, the virtual displacement principle described in [89] was used to develop a force deflection relation in the large deflection (stretching) regime. Using the wide membranes allowed us to ignore the deflection of the free edges, this way all edges were assumed to be simply supported and immovable. Fig. 4.14A) illustrates the geometry of the membranes under consideration. The deflection profile was assumed to be a half cosine, where the approximate displacements are given as:

$$\omega = d \cos \frac{\pi x}{2a} \cos \frac{\pi y}{2b}, u = c_1 \sin \frac{\pi x}{a} \cos \frac{\pi y}{2b}, v = c_2 \sin \frac{\pi y}{b} \cos \frac{\pi x}{2a}, \quad (4.1)$$

where ω , u , v are the displacements in z , x , and y directions respectively, d

is the deflection at the centre of membrane, and c_1 and c_2 are the maximum displacements in x and y directions respectively. The virtual displacement method described in reference [89] was used to find an approximate force deflection relation in the non-linear membrane domain (large deflection). The final force deflection relation is given by:

$$F = 4Etd^3 \frac{0.44a^{12} + 16.3a^{10}b^2 + 151a^8b^4 + 3.6a^6b^6 + 151a^4b^8 + 16.3a^2b^{10} + 0.44b^{12}}{a^3b^3(a^4 + 20.5a^2b^2 + b^4)^2}. \quad (4.2)$$

where t is the thickness of the membrane. This relation was calculated for a Poisson's ratio of 0.141. For a square, the force deflection relation is:

$$F = 2.7 \frac{Etd^3}{a^2}. \quad (4.3)$$

When this relation is adjusted for a uniform load (q) and a Poisson's ratio of 0.25 the relation becomes $q = 1.9Etd^3/a^4$, which agrees with reference [89]. Fig. 4.14A) illustrates the typical behaviour of the suspended membrane in the non-linear regime, and compares the measured deflection with the developed model. Fig. 4.14B) shows the extracted E values of 14 suspensions versus their W/L , the values has a mean of 140 GPa and a standard deviation 60 GPa, which is similar to the value extracted from the $C - V$ measurement ($E = 170 \pm 5$ GPa) for the same device.

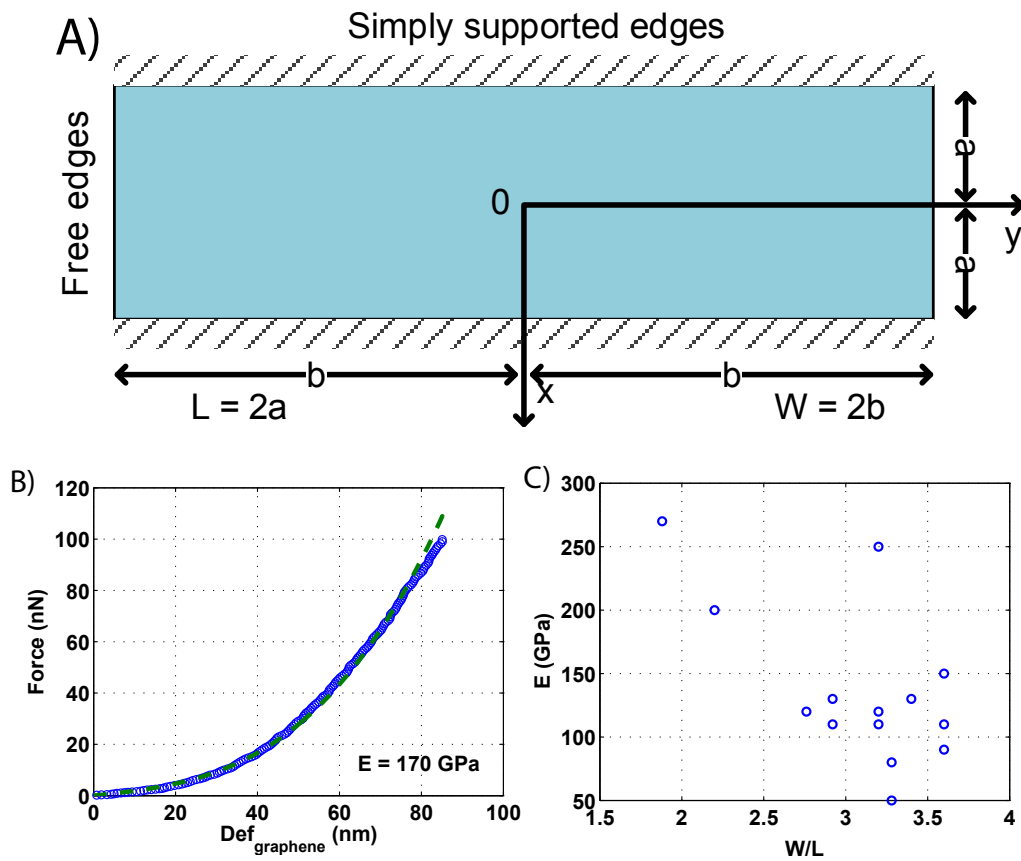


Fig. 4.14: A) The geometry of membranes under consideration. B) Applied force versus displacement for a large membrane with a linear fit. The inferred E value is 170 GPa. C) The extracted E values of 14 suspensions versus their W/L .

4.4 Summary

In this chapter, we demonstrated the $C - V$ characteristics of suspended graphene varactors, reaching a 55% tuning with a 10 V actuation voltage. We then used the theoretical model developed earlier to extract the values of the mechanical properties of graphene from the $C - V$ curves. Afterwards, we measured the field effect mobility and sheet resistance of the suspended graphene, from which we calculated the varactor time constant and electrical quality factor. Due to the high sheet resistance of graphene, the fabricated devices can not be used at radio frequencies. We also demonstrated the ambivalence of the varactor, and probed its non-linear response to AC signals. Finally, we performed $F - D$ AFM measurements to independently measure the mechanical properties of the suspended graphene, and found that the values of Young's modulus and membrane-pretension measured using this method agree with the values extracted from the $C - V$ fitting.

Chapter 5

Conclusion and future work

5.1 Summary

Radio frequency micro-electromechanical systems are becoming more important and profitable as they replace their semiconductor counterparts. The main challenges facing these devices are all due to their large size and micron range thickness. For the last decade suspended graphene devices have been investigated as the solution to these challenges, because atomic thinness of graphene makes it the ultimate limit of electromechanical structures.

We have investigated the theoretical limit of suspended graphene varactors (SGV), and found that they are very promising for low voltage RF applications as pull-in voltages below 5 V can be achieved. We have reported the analysis, simulation, and design equations of the SGV. We have also considered the use of the graphene switch in digital applications and investigated the limit where it works as a tunnelling relay. We have reported the analysis, simulation, and design of these tunnelling relays, and we have predicted that digital circuits

with operating voltages as low as 0.25 V can be built, which offers a potential reduction of both static and dynamic power consumptions to as little as 1% of the power consumption of state-of-the-art CMOS circuits.

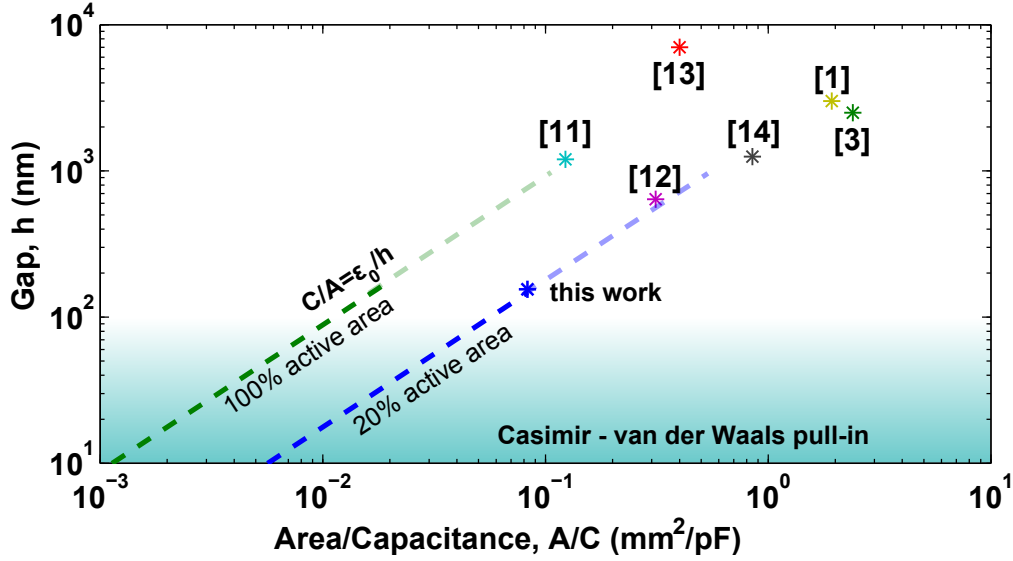


Fig. 5.1: A) A comparison between this work and different types of state of the art MEMS varactors. The figure shows the air/vacuum gap versus the area per pF. The devices shown are state of the art silicon based MEMS varactors: parallel plate with fractal structure[11], curved plate varactor[12], vertical parallel plate[13], parallel plate with levers[14], original parallel plate design[1], and comb finger varactor[3]. Further indicated in the graph are the ideal limits achievable in accordance with $C/A = \epsilon/h$. The varactor height is limited by spontaneous pull-in from Casimir-van der Waals forces.

We have also reported the fabrication of large array SGV with a yield of 95%, which exceeds the yields of large arrays of suspended graphene resonators previously reported in literature. The tunable capacitance per unit area of the fabricated devices is as much as 12pF/mm², which exceeds that achieved by traditional MEM varactors. Fig. 5.1 compares the size of the fabricated SGV with several state-of-the-art MEM varactors. This comparison shows that the

SGV fulfills our prediction of its potential small size. Moreover, this size can be further reduced by careful design and improved fabrication process. A tuning of 55% in suspended capacitance has been reported, which exceeds the 50% maximum tuning of a traditional parallel plate varactor. This tuning was achieved with a bias voltage of only 10 V. We have also measured the non-linear response of the SGV and found that it can be used as a frequency mixer for voltages close to its pull-in voltage.

5.2 Future work

We fabricated the proof-of-concept device shown in Fig. 5.2A), which has three principle shortcomings: RF compatibility, parasitic capacitance and actuation voltage. These aspects can be improved as follows:

- The RF compatibility can be achieved by two combining low sheet resistance graphene with a design in which all graphene suspensions are connected directly to the metal contacts as illustrated in 5.2B). This design minimize the over all resistance parasitic resistance of the varactor by using graphene only as movable membrane and using gold as interconnects. For a varactor with suspension length $L = 5\mu\text{m}$ and effective trench height $h = 200\text{nm}$ made from monolayer graphene with sheet resistance $R_{\square} = 240\Omega/\square$ [119], the electrical quality factor $Q \simeq 3000$ of varactor will be at 1 GHz.
- Fig. 5.2B) also illustrates a proposed patterning for the fixed electrode that confines the fixed electrode to the region under the suspended

graphene. This scheme will eliminate the parasitic capacitance due to the overlap between the fixed electrode and the interconnects above the trench separations. Nonetheless, parasitic capacitance will still exist due to capacitance between the edges of the fixed electrode and the interconnects, but they can be negligible. In this case the ratio of the parasitic capacitance C_p to the tunable capacitance C_v can be approximated as:

$$\frac{C_p}{C_v} \approx \frac{t_e}{L}. \quad (5.1)$$

where L is the length of the trench and t_e is the electrode thickness. For a varactor with trench length $L = 5\mu$ and electrode thickness $t_e = 100nm$, the parasitic capacitance will be less than 2 % of the tunable capacitance.

- The actuation voltage can be reduced by increasing the device aspect ratio. Aspect ratios as high as 40 were achieved for double clamped graphene suspensions[85] and as high at 100 for circular suspensions[87], nonetheless these processes had low yield. A way to improve the yield is to develop a process that does not require a critical point drying, which involves violent liquid exchange and dramatic pressure changes.

The ultimate goal for the SGV is to be integrated with CMOS circuits using only one or two post processing steps, which is feasible as the graphene is compatible with CMOS process and has been integrated with CMOS circuits since 2009[23, 24]. Nonetheless, this integration requires great effort to adjust the suspension process to CMOS dies.

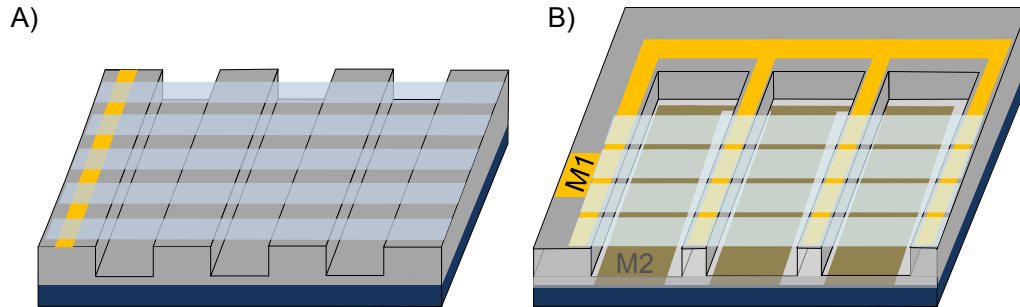


Fig. 5.2: A) Schematic of the fabricated device, while B) shows the a schematic of the improved varactor design.

The use of the proposed tunneling relays (TR) will offer a significant reduction in power consumption. Nonetheless, TRs require high aspect ratio (L/h) suspensions as well as small trench height $h < 50\text{nm}$. The small trench height requirement poses another challenge to increasing the fabrication yield, because the Casimir-van der Waals forces will be an additional force pulling the graphene membrane down. This additional challenge may be overcome by building the bottom and the walls of the trenches from materials that have low van der Waals forces between them and graphene.

References

- [1] B. Zhang and D. Fang. Modeling and modification of the parallel plate variable MEMS capacitors considering deformation issue. *Mechanism and Machine Theory*, 44(4):647–655, APR 2009.
- [2] J. Maciel, S. Majumder, J. Lampen, and C. Guthy. Rugged and reliable ohmic MEMS switches. In *IEEE MTT-S International Microwave Symposium Digest (MTT), 2012*, pages 1–3, June 2012.
- [3] D-H. Baek, Y. Eun, D-S. Kwon, M-O. Kim, T. Chung, and J. Kim. Widely Tunable Variable Capacitor With Switching and Latching Mechanisms. *IEEE Electron Device Letters*, 36(2):186–188, Feb 2015.
- [4] H. Kam, V. Pott, R. Nathanael, J. Jeon, E. Alon, and T-J. K. Liu. Design and reliability of a micro-relay technology for zero-standby-power digital logic applications. In *IEEE International Electron Devices Meeting (IEDM), 2009*, pages 1–4, Dec 2009.
- [5] J. S. Bunch, A. M. van der Zande, S. S. Verbridge, I. W. Frank, D. M. Tanenbaum, J. M. Parpia, H. G. Craighead, and P. L. McEuen. Electromechanical Resonators from Graphene Sheets. *Science*, 315(5811):490–493, 2007.
- [6] J. S. Bunch, S. S. Verbridge, J. S. Alden, A. M. van der Zande, J. M. Parpia, H. G. Craighead, and P. L. McEuen. Impermeable Atomic Membranes from Graphene Sheets. *Nano Letters*, 8(8):2458–2462, 2008.
- [7] P. Li and T. Cui. RF nano switch based on single crystalline graphene. In *18th International Conference on Solid-State Sensors, Actuators and Microsystems (Transducers), 2015*, pages 307–310, June 2015.
- [8] X. Li, Y. Zhu, W. Cai, M. Borysiak, B. Han, D. Chen, R. D. Piner, L. Colombo, and R. S. Ruoff. Transfer of Large-Area Graphene Films for High-Performance Transparent Conductive Electrodes. *Nano Letters*, 9(12):4359–4363, 2009.

- [9] F. Mayer, C. Le Royer, J. F. Damlencourt, K. Romanjek, F. Andrieu, C. Tabone, B. Previtali, and S. Deleonibus. Impact of SOI, Si_{1-x}Ge_xOI and GeOI substrates on CMOS compatible Tunnel FET performance. In *IEEE International Electron Devices Meeting, 2008. IEDM 2008*, pages 1–5, Dec 2008.
- [10] Overall Technology Roadmap Characteristics (ORTC). Technical report, International Technology Roadmap for Semiconductors, 2011.
- [11] A. M. Elshurafa, K. N. Salama, and P. H. Ho. Modeling and fabrication of an RF MEMS variable capacitor with a fractal geometry. In *IEEE International Symposium on Circuits and Systems (ISCAS), 2013*, pages 2711–2714, May 2013.
- [12] M. Bakri-Kassem, S. Fouladi, and R. R. Mansour. Novel High-Q MEMS Curled-Plate Variable Capacitors Fabricated in 0.35-um CMOS Technology. *IEEE Transactions on Microwave Theory and Techniques*, 56(2): 530–541, Feb 2008.
- [13] S. Achenbach, D. T. Haluzan, D. M. Klymyshyn, M. Borner, and J. Mohr. Large tuning ratio high aspect ratio variable capacitors using leveraged bending. *Microsystem Technologies*, 20(10-11):1807–1813, 2014.
- [14] C-H. Han, D-H. Choi, and J-B. Yoon. Parallel-Plate MEMS Variable Capacitor With Superior Linearity and Large Tuning Ratio Using a Levering Structure. *Journal of Microelectromechanical Systems*, 20(6): 1345–1354, Dec 2011.
- [15] R. R. Schaller. Moore’s law: past, present and future. *IEEE Spectrum*, 34(6):52–59, Jun 1997.
- [16] C. Liu. *Foundations of MEMS*. Pearson Education, Inc., 2006.
- [17] K. E. Bean. Anisotropic etching of silicon. *IEEE Transactions on Electron Devices*, 25(10):1185–1193, Oct 1978.
- [18] C. S. Smith. Piezoresistance Effect in Germanium and Silicon. *Physical Review*, 94:42–49, Apr 1954.
- [19] F. T. Geyling and J. J. Forst. Semiconductor Strain Transducers. *Bell System Technical Journal*, 39(3):705–731, 1960.

- [20] E. Mounier. Future of MEMS: a Market & Technologies Perspective. Technical report, Yole Developpement, 2014.
- [21] L. Wood. Global RF MEMS Market 2014-2018. Technical report, Reasearch and Markets, 2015.
- [22] V Vaganov. *Advanced Materials and Technologies for Micro/Nano-Devices, Sensors and Actuators*, chapter Challenges of Complete CMOS/MEMS Systems Integration, pages 17–30. Springer Netherlands, Dordrecht, 2010.
- [23] X. Chen, K-J. Lee, D. Akinwande, G. F. Close, S. Yasuda, B. Paul, S. Fujita, J. Kong, and H-S. P. Wong. High-speed graphene interconnects monolithically integrated with CMOS ring oscillators operating at 1.3GHz. In *IEEE International Electron Devices Meeting (IEDM), 2009*, pages 1–4, Dec 2009.
- [24] L. Huang, H. Xu, Z. Zhang, C. Chen, J. Jiang, X. Ma, B. Chen, Z. Li, H. Zhong, and L-M. Peng. Graphene/Si CMOS Hybrid Hall Integrated Circuits. *Scientific Reports*, 4:5548, 2014.
- [25] M. AbdelGhany, E. Ledwosinska, and T. Szkopek. Theory of the suspended graphene varactor. *Applied Physics Letters*, 101(15):153102, 2012.
- [26] A. Dec and K. Suyama. Micromachined varactor with wide tuning range. *Electronics Letters*, 33(11):922–924, May 1997.
- [27] G. M. Rebeiz. *RF MEMS, Applications, Theory, and Techniques*. John Wiley & Sons, Inc., 2003.
- [28] S. Lucyszyn. Review of radio frequency microelectromechanical systems technology. *IEE Proceedings - Science, Measurement and Technology*, 151(2):93–103, March 2004.
- [29] A. Emira, M. AbdelGhany, M. Elsayed, A. M. Elshurafa, S. Sedky, and K. N. Salama. All-pMOS 50-V Charge Pumps Using Low-Voltage Capacitors. *IEEE Transactions on Industrial Electronics*, 60(10):4683–4693, Oct 2013.
- [30] A. K. Geim. Graphene: Status and Prospects. *Science*, 324 (5934): 1530–1534, 2009.

- [31] H. D. Nguyen, D. Hah, P. R. Patterson, R. Chao, W. Piyawattanametha, E. K. Lau, and M. C. Wu. Angular vertical comb-driven tunable capacitor with high-tuning capabilities. *Journal of Microelectromechanical Systems*, 13(3):406–413, June 2004.
- [32] J. T. Kung and H-S. Lee. An integrated air-gap-capacitor pressure sensor and digital readout with sub-100 attofarad resolution. *Journal of Microelectromechanical Systems*, 1(3):121–129, Sep 1992.
- [33] Q. Zou, Z. Tan, Z. Wang, J. Pang, X. Qian, Q. Zhang, R. Lin, S. Yi, H. Gong, L. Liu, and Z. Li. A novel integrated silicon capacitive microphone-floating electrode “electret” microphone (FEEM). *Journal of Microelectromechanical Systems*, 7(2):224–234, Jun 1998.
- [34] L-S. Fan, Y-C. Tai, and R. S. Muller. IC-processed electrostatic micro-motors. In *Technical Digest of International Electron Devices Meeting (IEDM), 1988*, pages 666–669, Dec 1988.
- [35] C. Livermore, A. R. Forte, T. Lyszczarz, S. D. Umans, A. A. Ayon, and J. H. Lang. A high-power MEMS electric induction motor. *Journal of Microelectromechanical Systems*, 13(3):465–471, June 2004.
- [36] D. S. Greywall, P. A. Busch, F. Pardo, D. W. Carr, G. Bogart, and H. T. Soh. Crystalline silicon tilting mirrors for optical cross-connect switches. *Journal of Microelectromechanical Systems*, 12(5):708–712, Oct 2003.
- [37] P. Osterberg, H. Yie, X. Cai, J. White, and S. Senturia. Self-consistent simulation and modelling of electrostatically deformed diaphragms. In *Proceedings of IEEE Workshop on Micro Electro Mechanical Systems (MEMS), 1994*, pages 28–32, 1994.
- [38] T. K. Tsang, M. N. El-Gamal, W. S. Best, and H. J. De Los Santos. Wide tuning range RF-MEMS varactors fabricated using the PolyMUMPs foundry. *Microwave Journal*, 46(8):22–44, 2003.
- [39] H. Nieminen, V. Ermolov, K. Nybergh, S. Silanto, and T. Ryhanen. Microelectromechanical capacitors for RF applications. *Journal of Micromechanics and Microengineering*, 12(2):177, 2002.
- [40] J-B. Yoon and C. T-C. Nguyen. A high-Q tunable micromechanical capacitor with movable dielectric for RF applications. In *Technical Digest of International Electron Devices Meeting (IEDM), 2000*, pages 489–492, Dec 2000.

- [41] G. M. Rebeiz and Jeremy B. Muldavin. RF MEMS switches and switch circuits. *IEEE Microwave Magazine*, 2(4):59–71, Dec 2001.
- [42] R. E. Mihailovich, M. Kim, J. B. Hacker, E. A. Sovero, J. Studer, J. A. Higgins, and J. F. DeNatale. MEM relay for reconfigurable RF circuits. *IEEE Microwave and Wireless Components Letters*, 11(2):53–55, Feb 2001.
- [43] C. Goldsmith, J. Randall, S. Eshelman, T. H. Lin, D. Denniston, S. Chen, and B. Norvell. Characteristics of micromachined switches at microwave frequencies. In *IEEE MTT-S International Microwave Symposium Digest, 1996*, volume 2, pages 1141–1144 vol.2, June 1996.
- [44] D. Peroulis, S. P. Pacheco, K. Sarabandi, and L. P. B. Katehi. Electromechanical considerations in developing low-voltage RF MEMS switches. *IEEE Transactions on Microwave Theory and Techniques*, 51(1):259–270, Jan 2003.
- [45] W. M. van Spengen. Capacitive RF MEMS switch dielectric charging and reliability: a critical review with recommendations. *Journal of Micromechanics and Microengineering*, 22(7):074001, 2012.
- [46] S. Shekhar, K. J. Vinoy, and G. K. Ananthasuresh. Design, fabrication and characterization of capacitive RF MEMS switches with low pull-in voltage. In *Microwave and RF Conference (IMaRC), 2014 IEEE International*, pages 182–185, Dec 2014.
- [47] H. S. Newman, J. L. Ebel, D. Judy, and J. Maciel. Lifetime Measurements on a High-Reliability RF-MEMS Contact Switch. *IEEE Microwave and Wireless Components Letters*, 18(2):100–102, Feb 2008.
- [48] C. Goldsmith, D. Forehand, D. Scarbrough, Z. Peng, C. Palego, J. Hwang, and J. Clevenger. Understanding and improving longevity in RF MEMS capacitive switches, 2008.
- [49] T. N. Theis and P. M. Solomon. Its Time to Reinvent the Transistor! *Science*, 327(5973):1600–1601, 2010.
- [50] A. C. Seabaugh and Q. Zhang. Low-Voltage Tunnel Transistors for Beyond CMOS Logic. *Proceedings of the IEEE*, 98:2095–2110, DEC 2010.
- [51] S. Luryi, J. Xu, and A. Zaslavsky. *Device Proposals Beyond Silicon CMOS*, pages 127–140. Wiley-IEEE Press, 2010.

- [52] T. N. Theis and P. M. Solomon. In Quest of the "Next Switch": Prospects for Greatly Reduced Power Dissipation in a Successor to the Silicon Field-Effect Transistor. *Proceedings of the IEEE*, 98(12):2005–2014, dec. 2010.
- [53] T-J. K. Liu, D. Markovic, V. Stojanovic, and E. Alon. The relay reborn. *IEEE Spectrum*, 49(4):40–43, April 2012.
- [54] H. Zhao, Y. Chen, Y. Wang, F. Zhou, F. Xue, and J. Lee. InGaAs Tunneling Field-Effect-Transistors With Atomic-Layer-Deposited Gate Oxides. *IEEE Transactions on Electron Devices*, 58(9):2990–2995, 2011.
- [55] P. Guo, Y. Yang, Y. Cheng, G. Han, J. Pan, Ivana, Z. Zhang, H. Hu, Z. X. Shen, C. K. Chia, and Y-C. Yeo. Tunneling field-effect transistor with Ge/In_{0.53}Ga_{0.47}As heterostructure as tunneling junction. *Journal of Applied Physics*, 113(9):094502–094502–9, 2013.
- [56] M. Schmidt, L. Knoll, S. Richter, A. Schafer, J. Hartmann, Q. T. Zhao, and S. Mantl. Si/SiGe hetero-structure tunneling field effect transistors with in-situ doped SiGe source. In *13th International Conference on Ultimate Integration on Silicon (ULIS), 2012*, pages 191–194, 2012.
- [57] L. Britnell, R. V. Gorbachev, R. Jalil, B. D. Belle, F. Schedin, A. Mishchenko, T. Georgiou, M. I. Katsnelson, L. Eaves, S. V. Morozov, N. M. R. Peres, J. Leist, A. K. Geim, K. S. Novoselov, and L. A. Ponomarenko. Field-Effect Tunneling Transistor Based on Vertical Graphene Heterostructures. *Science*, 335(6071):947–950, FEB 24 2012.
- [58] D. Fu, J. Zhou, S. Tongay, K. Liu, W. Fan, T-J. K. Liu, and J. Wu. Mechanically modulated tunneling resistance in monolayer MoS₂. *Applied Physics Letters*, 103(18):183105, 2013.
- [59] H. Kam, T-J. K. Liu, V. Stojanovic, D. Markovic, and E. Alon. Design, Optimization, and Scaling of MEM Relays for Ultra-Low-Power Digital Logic. *IEEE Transactions on Electron Devices*, 58(1):236–250, jan. 2011.
- [60] K. Akarvardar, D. Elata, R. Parsa, G.C. Wan, K. Yoo, J. Provine, P. Peumans, R.T. Howe, and H.-S.P. Wong. Design Considerations for Complementary Nanoelectromechanical Logic Gates. In *IEEE International Electron Devices Meeting (IEDM), 2007*, pages 299–302, Dec 2007. doi: 10.1109/IEDM.2007.4418930.

- [61] F. Chen, H. Kam, D. Markovic, T-J. K. Liu, V. Stojanovic, and E. Alon. Integrated circuit design with NEM relays. In *Computer-Aided Design, 2008. ICCAD 2008. IEEE/ACM International Conference on*, pages 750–757, Nov 2008.
- [62] D. Grogg, Y. Pu, A. Knoll, U. Duerig, U. Drechsler, C. Hagleitner, and M. Despont. NEM switch technologies for low-power logic applications. In *IEEE Sensors, 2012*, pages 1–3, Oct 2012.
- [63] S. Hourri, G. Billiot, M. Belleville, A. Valentian, and H. Fanet. Limits of CMOS Technology and Interest of NEMS Relays for Adiabatic Logic Applications. *IEEE Transactions on Circuits and Systems I: Regular Papers*, 62(6):1546–1554, June 2015.
- [64] H. Alrudainy, A. Mokhov, and A. Yakovlev. A scalable physical model for Nano-Electro-Mechanical relays. In *Power and Timing Modeling, Optimization and Simulation (PATMOS), 2014 24th International Workshop on*, pages 1–7, Sept 2014.
- [65] D. Lee, W. S. Lee, C. Chen, F. Fallah, J. Provine, S. Chong, J. Watkins, R. T. Howe, H-S. P. Wong, and S. Mitra. Combinational Logic Design Using Six-Terminal NEM Relays. *IEEE Transactions on Computer-Aided Design of Integrated Circuits and Systems*, 32(5):653–666, May 2013.
- [66] R. Venkatasubramanian, S. K. Manohar, and P. T. Balsara. NEM Relay-Based Sequential Logic Circuits for Low-Power Design. *IEEE Transactions on Nanotechnology*, 12(3):386–398, May 2013.
- [67] V. Beiu, W. Ibrahim, M. Tache, and T-J. K. Liu. On ultra-low power hybrid NEMS-CMOS. In *Nanotechnology (IEEE-NANO), 2014 IEEE 14th International Conference on*, pages 201–206, Aug 2014.
- [68] N. Xu, J. Sun, I-R. Chen, L. Hutin, Y. Chen, J. Fujiki, C. Qian, and T-J. K. Liu. Hybrid CMOS/BEOL-NEMS technology for ultra-low-power IC applications. In *IEEE International Electron Devices Meeting (IEDM), 2014*, pages 28.8.1–28.8.4, Dec 2014.
- [69] H. G. Craighead. Nanoelectromechanical Systems. *Science*, 290 (5496): 1532–1535, 2000.
- [70] O. Y. Loh and H. D. Espinosa. Nanoelectromechanical contact switches. *Nature Nanotechnology*, 7:283295, 2012.

- [71] I. W. Frank, D. M. Tanenbaum, A. M. van der Zande, and P. L. McEuen. Mechanical properties of suspended graphene sheets. *Journal of Vacuum Science & Technology B*, 25(6):2558–2561, 2007.
- [72] M. Poot and H. S. J. van der Zant. Nanomechanical properties of few-layer graphene membranes. *Applied Physics Letters*, 92(6):063111, 2008.
- [73] C. Lee, X. Wei, J. W. Kysar, and J. Hone. Measurement of the Elastic Properties and Intrinsic Strength of Monolayer Graphene. *Science*, 321(5887):385–388, 2008.
- [74] X. Chen, K.-J. Lee, D. Akinwande, G. F. Close, S. Yasuda, B. Paul, S. Fujita, J. Kong, and H.-S. P. Wong. High-speed graphene interconnects monolithically integrated with CMOS ring oscillators operating at 1.3GHz. In *IEEE International Electron Devices Meeting (IEDM), 2009*, pages 1–4, Dec 2009.
- [75] M. AbdelGhany and T. Szkopek. Extreme sub-threshold swing in tunnelling relays. *Applied Physics Letters*, 104(1):013509, 2014.
- [76] U. Komaragiri, M. R. Begley, and J. G. Simmonds. The Mechanical Response of Freestanding Circular Elastic Films Under Point and Pressure Loads. *Journal of Applied Mechanics*, 72(2):203–212, 2005.
- [77] C. Chen, S. Rosenblatt, K. I. Bolotin, W. Kalb, P. Kim, I. Kymissis, H. L. Stormer, T. F. Heinz, and J. Hone. Performance of monolayer graphene nanomechanical resonators with electrical readout. *Nature Nanotechnology*, 4(5887):861 – 867, 2009.
- [78] A. M. van der Zande, R. A. Barton, J. S. Alden, C. S. Ruiz-Vargas, W. S. Whitney, P. H. Q. Pham, J. Park, J. M. Parpia, H. G. Craighead, and P. L. McEuen. Large-Scale Arrays of Single-Layer Graphene Resonators. *Nano Letters*, 10(12):4869–4873, 2010.
- [79] C. Chen, S. Lee, V. Deshpande, G.-H. Lee, M. Lekas, K. Shepard, and J. Hone. Graphene mechanical oscillators with tunable frequency. *Nature Nanotechnology*, 8:923–927, 2013.
- [80] J. Ma, W. Jin, H. L. Ho, and J. Y. Dai. High-sensitivity fiber-tip pressure sensor with graphene diaphragm. *Optics Letters*, 37(13):2493–2495, Jul 2012.

- [81] A. D. Smith, S. Vaziri, F. Niklaus, A. C. Fischer, M. Sterner, M. Delin, A. Ostling, and M. C. Lemme. Pressure sensors based on suspended graphene membranes. *Solid-State Electronics*, 88:89 – 94, 2013.
- [82] J. Aguilera-Servin, T. Miao, and M. Bockrath. Nanoscale pressure sensors realized from suspended graphene membrane devices. *Applied Physics Letters*, 106(8):083103, 2015.
- [83] E. Ledwosinska, T. Szkopek, A. Guermoune, and M. Siaj. Application of graphene membrane in micro-Golay cell array. In *SPIE Proceedings — Volume 8261 — THz Imaging, Spectroscopy, and Instrumentation II*, volume 8261, pages 82610A–82610A–8, 2012.
- [84] Z. Cheng, Q. Li, Z. Li, Q. Zhou, and Y. Fang. Suspended Graphene Sensors with Improved Signal and Reduced Noise. *Nano Letters*, 10 (5): 1864–1868, 2010.
- [85] K. M. Milaninia, M. A. Baldo, A. Reina, and J. Kong. All graphene electromechanical switch fabricated by chemical vapor deposition. *Applied Physics Letters*, 95(18), NOV 2 2009.
- [86] P. Li, Z. You, and T. Cui. Graphene cantilever beams for nano switches. *Applied Physics Letters*, 101(9):093111 –093111–5, aug 2012.
- [87] R. A. Barton, B. Ilic, A. M. van der Zande, W. S. Whitney, P. L. McEuen, J. M. Parpia, and H. G. Craighead. High, Size-Dependent Quality Factor in an Array of Graphene Mechanical Resonators. *Nano Letters*, 11(3): 1232–1236, 2011.
- [88] Y. Zhang, L. Zhang, and C. Zhou. Review of Chemical Vapor Deposition of Graphene and Related Applications. *Accounts of Chemical Research*, 46 (10):2329–2339, 2013.
- [89] S. P. Timoshenko and S. Woinowsky-Krieger. *Theory of Plates and Shells*. McGraw-Hill International Editions, 1959.
- [90] J. J. Vlassak and W. D. Nix. A new bulge test technique for the determination of Young’s modulus and Poisson’s ratio of thin films. *Journal of Materials Research*, 7:3242–3249, 1992.
- [91] J. Sarabadani, A. Naji, R. Asgari, and R. Podgornik. Many-body effects in the van der Waals - Casimir interaction between graphene layers. *Physical Review B*, 84:155407, Oct 2011.

- [92] C. Lee, X. Wei, J. W. Kysar, and J. Hone. Measurement of the Elastic Properties and Intrinsic Strength of Monolayer Graphene. *Science*, 321(5887):385–388, 2008.
- [93] M. W. Pruessner, T. T. King, D. P. Kelly, R. Grover, L. C. Calhoun, and R. Ghodssi. Mechanical property measurement of InP-based MEMS for optical communications. *Sensors and Actuators A: Physical*, 105(2):190 – 200, 2003.
- [94] E. M. Abdel-Rahman, H. I. Younis, and A. H. Nayfeh. Characterization of the mechanical behavior of an electrically actuated microbeam. *Journal of Micromechanics and Microengineering*, 12(6):759, 2002.
- [95] S. Jiang, S. Shi, and X. Wang. Nanomechanics and vibration analysis of graphene sheets via a 2D plate model. *Journal of Physics D: Applied Physics*, 47(4):045104, 2014.
- [96] A. D. Smith, S. Vaziri, A. Delin, M. Ostling, and M. C. Lemme. Strain engineering in suspended graphene devices for pressure sensor applications. In *13th International Conference on Ultimate Integration on Silicon (ULIS), 2012*, pages 21–24, March 2012.
- [97] S. J. Koester. High quality factor graphene varactors for wireless sensing applications. *Applied Physics Letters*, 99(16):163105, 2011.
- [98] S. Bae, H. Kim, Y. Lee, X. Xu, J-S. Park, Y. Zheng, J. Balakrishnan, T. Lei, H. R. Kim, Y. I. Song, Y-J. Kim, K. S. Kim, B. Ozyilmaz, J-H. Ahn, B. H. Hong, and S. Iijima. Roll-to-roll production of 30-inch graphene films for transparent electrodes. *Nature Nanotechnology*, 5:574578, 2010.
- [99] F. A. Ghavanini, P. Enoksson, S. Bengtsson, and P. Lundgren. Vertically aligned carbon based varactors. *Journal of Applied Physics*, 110(2):021101, 2011.
- [100] J. Garcia, M. Marrero-Martin, B. Gonzalez, I. Aldea, and A. Hernandez. Coupled varactor based on PN junction and accumulation MOS for RF applications. In *2011 Spanish Conference on Electron Devices (CDE)*, pages 1–4, Feb 2011.
- [101] H. Kempa, P. Esquinazi, and Y. Kopelevich. Field-induced metal-insulator transition in the c -axis resistivity of graphite. *Physical Review B*, 65:241101, May 2002.

- [102] R. Zacharia, H. Ulbricht, and T. Hertel. Interlayer cohesive energy of graphite from thermal desorption of polyaromatic hydrocarbons. *Physical Review B*, 69:155406, Apr 2004.
- [103] Y-J. Yu, Y. Zhao, S. Ryu, L. E. Brus, K. S. Kim, and P. Kim. Tuning the Graphene Work Function by Electric Field Effect. *Nano Letters*, 9(10):3430–3434, 2009.
- [104] A. Guermoune, T. Chari, F. Popescu, S. S. Sabri, J. Guillemette, H. S. Skulason, T. Szkopek, and M. Siaj. Chemical vapor deposition synthesis of graphene on copper with methanol, ethanol, and propanol precursors. *Carbon*, 49(13):4204 – 4210, 2011.
- [105] A. Jorio, R. Saito, M. S. Dresselhaus, and G. Dresselhaus. *Raman Spectroscopy in Graphene Related Systems*. WILEY-VCH, 2011.
- [106] A. C. Ferrari, J. C. Meyer, V. Scardaci, C. Casiraghi, M. Lazzeri, F. Mauri, S. Piscanec, D. Jiang, K. S. Novoselov, S. Roth, and A. K. Geim. Raman Spectrum of Graphene and Graphene Layers. *Physical Review Letters*, 97:187401, Oct 2006.
- [107] F. Tuinstra and J. L. Koenig. Raman Spectrum of Graphite. *The Journal of Chemical Physics*, 53(3):1126–1130, 1970.
- [108] P. Y. Huang, C. S. Ruiz-Vargas, A. M. van der Zande, W. S. Whitney, M. P. Levendorf, J. W. Kevek, S. Garg, J. S. Alden, C. J. Hustedt, Y. Zhu, J. Park, P. L. McEuen, and D. A. Muller. Grains and grain boundaries in single-layer graphene atomic patchwork quilts. *Nature*, 469:389392, 2011.
- [109] C. S. Ruiz-Vargas, H. L. Zhuang, P. Y. Huang, A. M. van der Zande, S. Garg, P. L. McEuen, D. A. Muller, R. G. Hennig, and J. Park. Softened Elastic Response and Unzipping in Chemical Vapor Deposition Graphene Membranes. *Nano Letters*, 11(6):2259–2263, 2011.
- [110] G-H. Lee, R. C. Cooper, S. J. An, S. Lee, A. van der Zande, N. Petrone, A. G. Hammerberg, C. Lee, B. Crawford, W. Oliver, J. W. Kysar, and J. Hone. High-Strength Chemical-Vapor-Deposited Graphene and Grain Boundaries. *Science*, 340(6136):1073–1076, 2013.
- [111] S. Bae, H. Kim, Y. Lee, X. Xu, J-S. Park, Y. Zheng, J. Balakrishnan, T. Lei, H. R. Kim, Y. I. Song, Y-J. Kim, K. S. Kim, B. Ozyilmaz, J-H. Ahn, B. H. Hong, and S. Iijima. Roll-to-roll production of 30-inch

- graphene films for transparent electrodes. *Nature Nanotechnology*, 5(8): 574–578, AUG 2010.
- [112] D. L. Sounas, H. S. Skulason, H. V. Nguyen, A. Guermoune, M. Siaj, T. Szkopek, and C. Caloz. Faraday rotation in magnetically biased graphene at microwave frequencies. *Applied Physics Letters*, 102(19), 2013.
- [113] P. L. Levesque, S. S. Sabri, C. M. Aguirre, J. Guillemette, M. Siaj, P. Desjardins, T. Szkopek, and R. Martel. Probing Charge Transfer at Surfaces Using Graphene Transistors. *Nano Letters*, 11(1):132–137, 2011.
- [114] J. D. Whittaker, E. D. Minot, D. M. Tanenbaum, P. L. McEuen, and R. C. Davis. Measurement of the Adhesion Force between Carbon Nanotubes and a Silicon Dioxide Substrate. *Nano Letters*, 6(5):953–957, 2006.
- [115] S. Alexander, L. Hellemans, O. Marti, J. Schneir, V. Elings, P. K. Hansma, M. Longmire, and J. Gurley. An atomic-resolution atomic-force microscope implemented using an optical lever. *Journal of Applied Physics*, 65(1):164–167, 1989.
- [116] N. P. D’Costa and J. H. Hoh. Calibration of optical lever sensitivity for atomic force microscopy. *Review of Scientific Instruments*, 66(10): 5096–5097, 1995.
- [117] J. L. Hutter and J. Bechhoefer. Calibration of atomic-force microscope tips. *Review of Scientific Instruments*, 64(7):1868–1873, 1993.
- [118] L. Zhang, J. Wang, and Y-H. Zhou. Wavelet solution for large deflection bending problems of thin rectangular plates. *Archive of Applied Mechanics*, 85(3):355–365, 2014.
- [119] V. P. Pham, K. H. Kim, M. H. Jeon, S. H. Lee, K. N. Kim, and G. Y. Yeom. Low damage pre-doping on CVD graphene/Cu using a chlorine inductively coupled plasma. *Carbon*, 95:664 – 671, 2015.